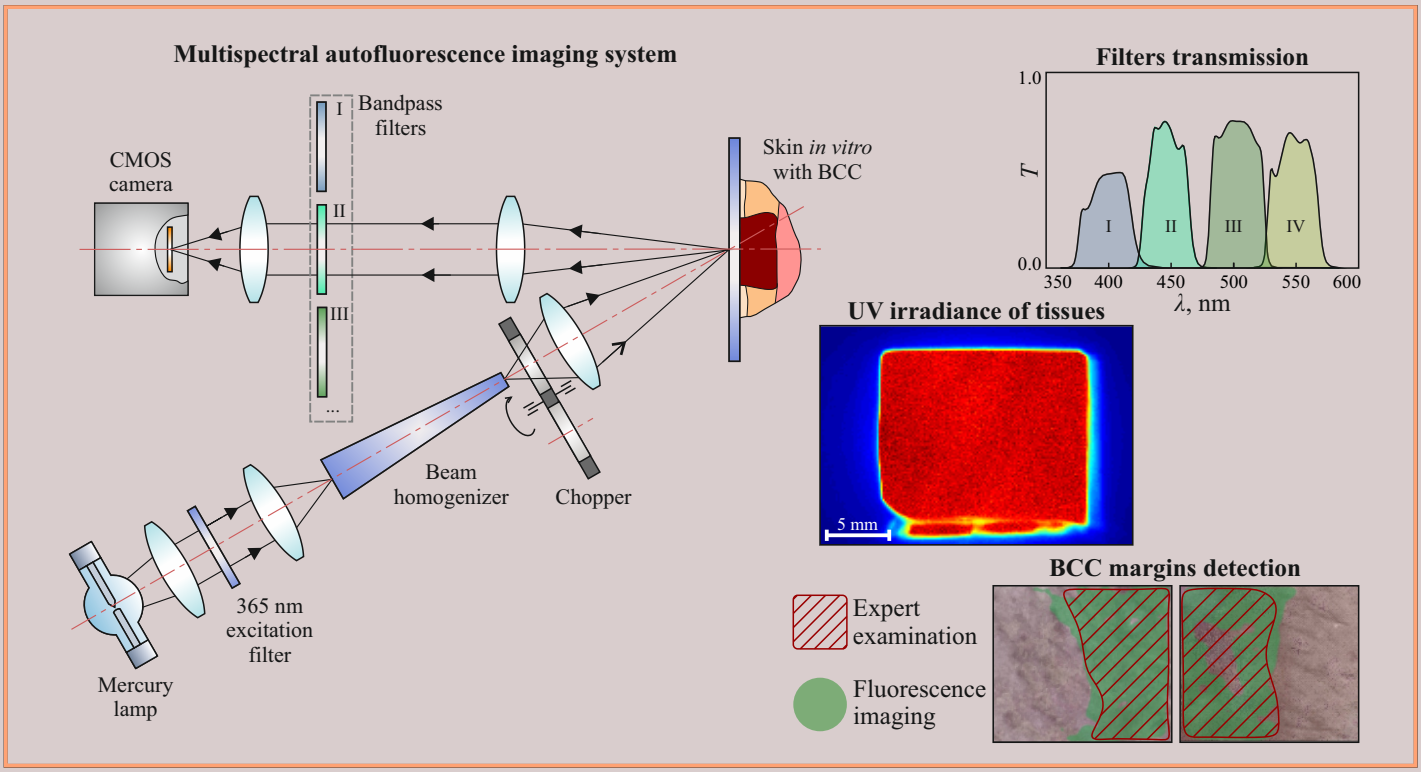
Volume 5, Issue 1, 2019

Journal of Biomedical Photonics & Engineering

Special Issue

"Years in Optoacoustics: 70-th Anniversary of Prof. Vladimir P. Zharov"



Special Issue Editors: Ekaterina I. Galanzha, Dmitry A. Gorin, and Valery V. Tuchin

© 2019 J-BPE

 doi: 10.18287/JBPE18.05.010001

Journal of Biomedical Photonics & Engineering

by Samara National Research University

Volume 5, Issue 1 (March 2019)

Editorial Board

Editor-In-Chief

Valery V. Tuchin - Saratov National Research State University, Russian Federation;
Institute of Precision Mechanics and Control RAS, Russian Federation

Deputy Editor-In-Chief

Valery P. Zakharov - Samara National Research University, Russian Federation

Editorial Board

Stefan Andersson-Engels (Tyndall National Institute, Ireland), **Alexey N. Bashkatov** (Saratov National Research State University, Russia), **Ekaterina Borisova** (Institute of Electronics, Bulgarian Academy of Sciences, Bulgaria), **Wei Chen** (University of Central Oklahoma, USA), **Arthur Chiou** (National Yang-Mind University, Taiwan), **Elina Genina** (Saratov National Research State University, Russia), **Min Gu** (Swinburne University, Australia), **Dror Fixler** (Bar-Ilan University, Ramat Gan, Israel), **Vyacheslav Kalchenko** (The Weizmann Institute of Science, Israel), **Nikolay G. Khlebtsov** (Institute of Biochemistry and Physiology of Plants and Microorganisms RAS, Russia), **Juergen Lademann** (Charite University Clinic, Germany), **Kirill V. Larin** (University of Houston, USA), **Martin Leahy** (University of Galway, Ireland), **Qingming Luo** (Huazhong University of Science and Technology, China), **Stephen J. Matcher** (University of Sheffield, Great Britain), **Aleksandra M. Mayorova** (Samara Branch of P.N. Lebedev Physical Institute of Russian Academy of Sciences, Russia), **Igor Meglinski** (University of Oulu, Finland), **Vladimir S. Pavelyev** (Image Processing Systems Institute RAS, Russia), **Francesco Pavone** (University of Florence, Italy), **Roberto Pini** (Institute of Applied Physics, Italy), **Igor A. Platonov** (Samara National Research University, Russia), **Juergen Popp** (Institute of Photonic Technology, Germany), **Alexander V. Priezzhev** (Moscow State University, Russia), **David Sampson** (The University of Western Australia, Australia), **Alexander Savitsky** (Institute of Biochemistry RAS, Russia), **Alexander P. Shkurinov** (Moscow State University, Russia), **Peter So** (Massachusetts Institute of Technologies, USA), **Janis Spigulis** (University of Latvia, Latvia), **Ilya V. Turchin** (Institute of Applied Physics RAS, Russia), **Lihong V. Wang** (California Institute of Technology, USA), **Ruikang Wang** (University of Washington, USA), **Xunbin Wei** (Shanghai Jiao Tong University, China), **Dan Zhu** (Britton Chance Center for Biomedical Photonics, Huazhong University of Science and Technology, China).

Postal address:
39B Lukacheva st., room #301
Samara 443086, Russian Federation

 © 2019 J-BPE

doi: 10.18287/JBPE18.05.010001

Special Issue

"Years in Optoacoustics: 70th Anniversary of Prof. Vladimir P. Zharov"

Special Issue Editors

Ekaterina I. Galanzha
University of Arkansas for Medical Sciences (UAMS), Little Rock, AR, USA
Saratov State University, Russia

Dmitry A. Gorin
Skolkovo Institute of Science and Technology, Moscow, Russia

Valery V. Tuchin,
Saratov State University, Russia
Institute of Precision Mechanics and Control of the RAS, Russia
Tomsk State University, Russia

Used Figure from this issue on the Cover

Nikita V. Chernomyrdin et al. Differentiation of basal cell carcinoma and healthy skin using multispectral modulation autofluorescence imaging: A pilot study, 010302, Figs. 1, 4 (combined).

© 2019 J-BPE

Contents

Introduction

Years in Optoacoustics: 70th Anniversary of Prof. Vladimir P. Zharov 010101

Articles

Miniature optical fiber sensors using surface enhanced Raman spectroscopy (SERS) for remote biochemical sensing 010301
Aditya H. Pandya, Joseph C. Kumaradas, and Alexandre Douplik

Differentiation of basal cell carcinoma and healthy skin using multispectral modulation autofluorescence imaging: A pilot study 010302
Nikita V. Chernomyrdin, Anastasiya D. Lesnichaya, Egor V. Yakovlev, Konstantin G. Kudrin, Olga P. Cherkasova, Elena N. Rimskaya, Vladimir N. Kurlov, Valeriy E. Karasik, Igor V. Reshetov, Valery V. Tuchin, and Kirill I. Zaytsev

Laser photoacoustic spectroscopy applications in breathomics 010303
Yury V. Kistenev, Alexey V. Borisov, Victor V. Nikolaev, Denis A. Vrazhnov, and Dmytry A. Kuzmin

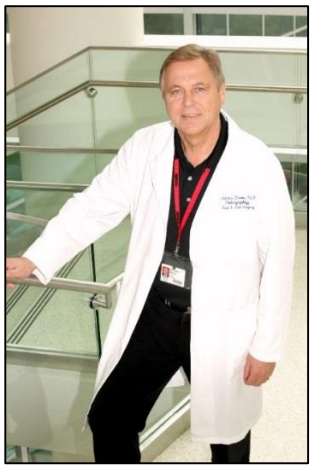
Optoacoustic gas-analysis for diagnostics of biosystems 010304
Boris G. Ageev, Olga Y. Nikiforova, Yurii N. Ponomarev, and Valeria A. Sapozhnikova

Application of Yb,Er:Glass laser radiation for active drug delivery at the treatment of onychomycosis 010305
Andrey V. Belikov, Anastasia D. Tavalinskaya, Sergey N. Smirnov, and Andrey N. Sergeev

 © 2019 J-BPE

 doi: 10.18287/JBPE18.05.010101

Years in Optoacoustics: 70th Anniversary of Prof. Vladimir P. Zharov





The guest editors introduces this Special Issue of the Journal of Biomedical Photonics & Engineering in honor of **Vladimir P. Zharov**, PhD, DSc, who is considered one of the pioneers of the modern era of biomedical engineering associated with novel integrations of laser diagnostics and therapy called laser theranostics with focus on photoacoustic and photothermal targeted theranostics using conjugated nanoparticles as the photoacoustic and phohothemal molecular contrast agents. He has the extraordinary influence on this field. **Vladimir Zharov**'s research interests are exceptionally broad and his contributions to the field fall into many distinct areas including laser spectroscopy, photoacoustics (called also optoacoustics), analytical chemistry, nanomedicine and biophotonics, and their multiple applications for theranostics (diagnosis + therapy) and prevention of cancer, infection and cardiovascular disorders (e.g., stroke) which are major killers in the world [1-27].

Prof. Zharov pioneered a high resolution photoacoustic spectroscopy with tunable lasers [1, 2] and invented photoacoustic flow cytometry [5, 6, 9-16] and pulsed nanophototherapy of infections and cancers targeted by gold nanoclusters [17-24], photoacoustic and photothermal tweezers for manipulation of nanoparticles and cells even in blood [26], photothermal super-resolution confocal and multiplex imaging [16], photothermal-gene therapy [24], noninvasive ultrasensitive blood test [15, 27] and *in vivo* multicolor flow cytometry [9-11]. In particular, **Prof. Zharov** pioneered (2002) one of the first applications of nanotechnology for cancer treatment using pulse laser-induced photothermal and accompanied nanobubble-formation phenomena around gold nanoparticles and, especially, their clusters targeted cancer cells [17-24].

He discovered ultrasharp (~1 nm) photothermal and photoacoustic spectral resonances in plasmonic nanostructures and their red and blue spectral shifting [7], which were named after him by others as "*Zharov splitting*." [25]

 doi: 10.18287/JBPE18.05.010101

He leaded the group of interdisciplinary researches to demonstrate the first clinical application of in vivo theranostics of circulating tumor cells (CTCs) in melanoma patients with the ~1000-fold sensitivity improvement and simultaneous laser killing of early CTCs that open way to prevent the development of deadly metastasis [15]. His team demonstrated also first biomedical application of spasers (nanolasers) as the brightest labels for advancer targeted single cell theranostics [8].

For his innovations, **Prof. Zharov** was many prestigious awards including the State Prize (1989), one of the Russia's highest scientific award for laser monitoring of pollution in atmosphere, and the United States' Maiman Award (1993), named after the inventor of the first laser (**Vladimir Zharov** was the first recipient of this award) for first combination of ultrasound and laser for microsurgery using optical fibers as the waveguide for both acoustic waves and laser radiation. **Vladimir Zharov** richly deserves to be called a photoacoustic flow cytometry "pioneer," and not just of a single methodology.

In the eighties, **Vladimir Zharov** received unique interdisciplinary education and skills in physics (degree from Moscow State University), optical engineering (degrees from Moscow State Technical University), photobiology and biochemistry (fellowship at the Lawrence Berkeley National Laboratory at the University of California in 1984-1985) and business management (Diploma certificate from the U.S. Educational Center in Moscow in 1993). Through serving as the Chairman of largest in Russia Biomedical Engineering Department (1989-2000) at the Moscow State Technical University named after N.E. Bauman and as a president of the private company "Yainvest" in Moscow at the end of the1980s and into the 1990s, **Vladimir Zharov** was focused on both fundamental research and commercialization. Based on his broad interdisciplinary background in biomedical engineering he organized commercial productions of novel hybrid medical technologies and apparatuses for LED-vacuum, magnetic-laser and electro-laser therapies. These systems have been successfully used in many Russian medical centers and clinics to treat several thousand patients who suffered from infected wounds, postmastectomy lymphedema, and urological disorders (e.g., chronic prostatitis).

In collaboration with the colleagues from the Institute of Spectroscopy RAS, Moscow State University, and Bauman Moscow State Technical University there were developed and studied [1-4]: optoacoustic (OA) spectroscopy (named later photoacoustic) of the excited molecule states using heated OA detector (1977); OA nonlinear and multiphoton absorption using strong-focused laser beams with high spatial resolution OA detector (1978); OA isotope analysis (1976-1982); laser-acoustic drug injection and delivery through syringe needle (1986-1987); the influence of laser-acoustic effects on cells using nanosecond and picosecond pulses (1986-1989), laser-OA scalpel (1986); destruction of gall bladder stones by using "internal" and "external" OA effects (1986); principle and the first demonstration of OA tomography of large beam profiles (1988-1989); biophotophone for diagnostic of ear's diseases with an ear as natural acoustic sensor of acoustic waves generated by light in different internal ear's zones (1987); OA-chromatographic detectors for early diagnostic of some diseases including detection of vitamin A in blood plasma (1986) and some organic substances in exhaled air associated with tuberculosis (1989); the first application the remote pulsed photothermal radiometry for study tissue properties and as a feedback in laser medicine (1986-1987). His team also developed the first integration of laser and low-

 doi: 10.18287/JBPE18.05.010101

frequency (20-50 kHz) ultrasound technology for microsurgery using the same optical fiber for delivery optical and acoustic waves that increased the cutting and drilling speed (5-10-fold) of soft and hard tissues with simultaneous self-cleaning the surgical tip.

In 1997-2000 they tested in clinical condition novel photo-ultrasonic treatment of infected wounds by integration photodynamic therapy (PDT) and ultrasonic (US) therapy with antibiotics (A) as tools for effective killing bacteria. The delivery into wound both photosensitizer (PS) and A and followed up light irradiation and US low-frequency application brought new advantages: effective mixing of A and PS in solution; enhanced diffusion A in tissue; increasing penetration of PS in bacteria; US clearing of surface from necrotic adjournment; additional US-induced bactericidal effect; increasing efficacy of light irradiation of non-transparent wound; and additional activation of immune system. The clinical trials with over 200 patients with different post-operation infectious complications of different origin demonstrated advantage of new technology [4].

At that time **Zharov**'s team also developed [4]: photo-bactericidal patch as integration of LED-based thin film chip with PA to provide PDT of local skin infected areas; photo-electrical autonomous capsule of elliptical shape with size ∅ 8×16 mm for therapy in endoscopy; implantable electrooptical module ∅ 4×0.8 mm with remote power supply using pulse magnetic field and miniature coil inside module (these micro-modules during clinical trials in Institute of Eye's Surgery in Moscow in 1996-1999 were implanted in eyes of 175 patients with different vision problems caused mostly by atrophied optic nerve; LED-based strip with remote pulse magnetic power source for treatment of chronic generalized parodontitis (20 patients were treated in Moscow State University of Medicine and Dentistry in 1998-2000).

Prof. Zharov broad interdisciplinary background and experience in biomedical engineering helped him to organize commercial productions of novel hybrid medical technologies. Specifically in 1992-1999, **Zharov**'s team commercialized several combined therapeutic technologies for treatment of chronic prostatitis [4]: 1) electro-laser apparatus integrating near-infrared therapy and electrostimulation that provided increasing of blood microcirculation, improving drug delivery, and reducing infections (it has been used in 140 Russian clinics for successful treatment of many thousand patients); 2) "photo-vacuum" therapy integrating powerful LED array and so-called "vacuum" therapy (decompression); 3) photo-magnetic therapy integrating relatively high intensity of pulse magnetic field and laser thermal therapy with infrared pulse laser diode. Phototherapy of lymphedema after mastectomy (breast cancer surgery) using powerful LED array and compression was used with the high efficacy (87%) for treatment 128 patients in Moscow State University of Medicine and Dentistry (1997-1999). **Zharov**'s team presented the first experimental evidence of mechanism of phototherapy with powerful LED array as photochemical transformation IgG antibody from a low-acid state to a high one that was used in 1998-2000 for treatment of 18 patients with atopic dermatitis [4].

Since 2000 as the Director of the Laser Research at Winthrop Paul Rockefeller Cancer Institute at the University of Arkansas for Medical Science (UAMS), he established Arkansas Nanomedicine Center (ANC), which is currently one of the best in the USA in the field of Nanotechnology, Nanomedicine, and Biophotonics and their clinical applications. He was one of the researchers who

 doi: 10.18287/JBPE18.05.010101

clearly saw the potential of integration of photoacoustics, nanotechnology, and laser optics for biomedicine. Specifically, he became interested in the biomedical applications of these technologies to answer a question: how to help people with severe diseases like cancer, heart attack, stroke and severe infections? His curiosity and wide spanning intellectual interests enriched these fields and propelled them in many ways.

The one of his main achievements in the USA is the developing in 2002-2003 innovative integrations of laser and nanotechnology, which opened new avenues in medicine called laser Nanomedicine for earliest diagnosis and treatment of cancer with focus on metastasis (leading to 90% of cancer death) prevention. He is among those scientists who have made pioneering and contributions in innovative integration of laser, nanotechnology, and medicine. Since then the fields have grown exponentially to become an integral part in many medical disciplines.

Prof. Zharov has provided leadership in many multidisciplinary NIH and NSF research and translational research projects. Quickly adapting to USA's complicated and multilayered funding system, he demonstrated the ability to obtain multiple state and federal grants serving as principal investigator/leader. Overall, **Prof. Zharov** is the principle investigator of 17 grants from the National Institute of Health (NIH), National Science Foundation (NSF), Medical programs of Department of Defense (DOD), and many other agencies, as well as international projects with Samsung, Inc., and European Programme 'EUREKA'. Under his leadership, his self-supporting (i.e., funding from grants) for laboratories have had total nearly $11 million budget.

Zharov's work in the assessment of the physical properties, toxicity, targeting, and pharmacokinetics of the advanced nanotechnology products (e.g., new bioconjugated nanoparticles) has received significant support from two Nanotechnology centers at the University of Arkansas at Fayetteville and at Little Rock and especially from Nanocore in the FDA-affiliated National Center for Toxicological Research (NCTR) in Arkansas.

Today, **Prof. Zharov** leads several clinical trials of new biomedical technologies including photoacoustic flow cytometry and MRI-guided laser interstitial therapy for the earliest theranostics of metastatic tumors (e.g., melanoma), local tumor and laser treatment of post-resection margins as well as advanced diagnosis of cardiovascular diseases and infections. His 18 years' experience at UAMS with clinical studies allowed him to establish interdisciplinary very productive team of physicist, engineers, chemists, biologists and physicians with publication's rate up to 10-20 papers per year. His communication skills allowed him to establish international collaborations with many universities in different countries (e.g., Russia, Germany, Canada, and Slovenia). He has authored ~200 peer-reviewed publications (including 10 papers in Nature journals), five books, and 55 patents.

The several state medical magazines, and European journal of international innovation have highlighted **Prof. Zharov**'s extraordinarily accomplishments, innovations and ability to conduct groundbreaking research in the novel methods of noninvasive disease diagnosis with ultra-high sensitivity. His work has been featured also in several respected sources including NIH website, and journals with the high impact factor such as Nature and Nature Nanotechnology, which highlighted

 doi: 10.18287/JBPE18.05.010101

his the first-of-its-kind clinical trials using photoacoustic flow cytometry for early cancer diagnosis and therapy.

Prof. Zharov is working in the strong collaboration with scientists across the world (e.g., Vladimir Torchilin, Samir Gambhir, Mark Stockman, Valery Tuchin, Vladislav Verkhusha, Markus Frank, Viacheslav Artyushenko, Nikolai Khlebtsov, and Dmitry Gorin) from many universities and companies including IPG Photonics, BrightSolution, Art Photonics, Skolkovo Institute of Science and Technology, Moscow State University, Tomsk State University, Saratov State University, Saratov Medical State University, Institute of Bioorganic Chemistry, Institute of Biochemistry and Physiology of Plants and Microorganisms.

In 2017, **Prof. Zharov** was awarded by the Megagrant given by the Russian Ministry of Science and Higher Education, which allowed him to establish the laboratory of Biomedical Photoacoustics at Saratov State University in 2018. The main goal of this laboratory is the development of a new concept, approaches, methods and technical solutions for an ultrasensitive analysis of almost the entire blood volume of the patients, and thus to detect rare disease-associated biomarkers, in particular, CTCs, exosomes, bacteria and clots presenting in extremely low concentrations, especially at the early disease stages, for example, down to a few CTCs per 5 liters of blood.

This Special Issue in **Vladimir Zharov**'s honor provides a multidisciplinary reflection on his career, indicating the breadth of **Vladimir Zharov**'s scientific interests and contributions.

The guest editors of this Special Issue would like to thank all authors for their efforts in preparing their contributions and thank all the reviewers for their help in reviewing these papers. Last but not least, we would like to thank the editorial staff of Journal of Biomedical Photonics & Engineering for the opportunity to organize this Special Issue.

Special Issue Editors:

Ekaterina I. Galanzha
Laboratory of Lymphatic Research, Diagnosis and Therapy (LDT),
University of Arkansas for Medical Sciences (UAMS),
Little Rock, AR, USA,
Photoacoustic Laboratory, Saratov State University,
Saratov 410012, Russia
E-mail: egalanzha@uams.edu

Dmitry A. Gorin,
Skolkovo Institute of Science and Technology,
Moscow 143026, Russia
E-mail: d.gorin@skoltech.ru

Valery V. Tuchin
Research-Educational Institute of Optics and Biophotonics,
Saratov State University,
Saratov 410012,
Institute of Precision Mechanics and Control of the RAS,
Saratov 410028,

Tomsk State University,
Tomsk 634050, Russia
E-mail: tuchinvv@mail.ru

Selected publications of Prof. Zharov

1 V. P. Zharov, V. S. Letokhov, Laser Optoacoustic Spectroscopy, Springer Series in Optical Sciences. Vol. 37, Springer-Verlag, Berlin, Heidelberg, New York (1986).
2 V. P. Zharov, "Laser optoacoustic spectroscopy in chromatography," Chap in Laser Analytical Spectrochemistry, V. S. Letokhov (ed), The Adam Hilger Series on Optics and Optoelectronics, Bristol, Boston, Mass, 229-271 (1986).
3 V. P. Zharov, "Application of power optoacoustic methods and instruments in medicine and biology," Chap. in Photoacoustics and Photothermal Phenomena, Springer Series in Optical Sciences. Vol. 58, Springer, Berlin, 533-547 (1987).
4 V. P. Zharov, A. S. Latyshev, "Laser combined medical technologies from Russia," Journal of Laser Applications 11(2), 80-90 (1999).
5 E. I. Galanzha, V. P. Zharov, "Photoacoustic flow cytometry," Methods 57(3), 280-296 (2012).
6 V. V. Tuchin, A. Tárnok, and V. P. Zharov, "In vivo flow cytometry: A horizon of opportunities," Cytometry Part A 79A(10), 737-745 (2011).
7 V. P. Zharov, "Ultrasharp nonlinear photothermal and photoacoustic resonances and holes beyond the spectral limit," Nature Photonics 5(2), 110-116 (2011).
8 E. I. Galanzha, R. Weingold, D. A. Nedosekin, M. Sarimollaoglu, J. Nolan, W. Harrington, A. S. Kuchyanov, R. G. Parkhomenko, F. Watanabe, Z. Nima, A. S. Biris, A. I. Plekhanov, M. I. Stockman, and V. P. Zharov, "Spaser as a biological probe," Nature Communications 8(1), 15528 (2017).
9 J.-W. Kim, E. I. Galanzha, E. V. Shashkov, H.-M. Moon, and V. P. Zharov, "Golden carbon nanotubes as multimodal photoacoustic and photothermal high-contrast molecular agents," Nature Nanotechnology 4(10), 688-694 (2009).
10 E. I. Galanzha, E. V. Shashkov, T. Kelly, J.-W. Kim, L. Yang, and V. P. Zharov, "In vivo magnetic enrichment and multiplex photoacoustic detection of circulating tumour cells," Nature Nanotechnology 4(12), 855-860 (2009).
11 E. I. Galanzha, E. V. Shashkov, P. M. Spring, J. Y. Suen, and V. P. Zharov, "In vivo, noninvasive, label-free detection and eradication of circulating metastatic melanoma cells using two-color photoacoustic flow cytometry with a diode laser," Cancer Research 69(20), 7926-7934 (2009).
12 A. Zerda, J.-W. Kim, E. I. Galanzha, S. S. Gambhir, and V. P. Zharov, "Advanced contrast nanoagents for photoacoustic molecular imaging, cytometry, blood test, and photothermal theranostics," Contrast Media & Molecular Imaging 6(5), 346-369 (2011).
13 D. A. Nedosekin, M. Sarimollaoglu, E. I. Galanzha, R. Sawant, V. P. Torchilin, V. V. Verkhusha, J. Ma, M. H. Frank, A. S. Biris, and V. P. Zharov, "Synergy of photoacoustic and fluorescence flow cytometry of circulating cells with negative and positive contrasts," Journal of Biophotonics 6(5), 425-434 (2013).
14 Y. A. Menyaev, K. A. Carey, D. A. Nedosekin, M. Sarimollaoglu, E. I. Galanzha, J. S. Stumhofer, and V. P. Zharov, "Preclinical photoacoustic models: application for ultrasensitive single cell malaria diagnosis in large vein and artery," Biomedical Optics Express 7(9), 3643-3658 (2016).
15 E. I. Galanzha, Y. A. Menyaev, A. C. Yadem, M. Sarimollaoglu, M. A. Juratli, D. A. Nedosekin, S. R. Foster, A. Jamshidi-Parsian, E. R. Siegel, I. Makhoul, L. F. Hutchins, J. Y. Suen, and V. P. Zharov, "In vivo liquid biopsy using Cytophone platform for photoacoustic detection of circulating tumor cells in patients with melanoma," Science Translational Medicine (2019) [in press].
16 D. A. Nedosekin, E .I. Galanzha, E. Dervishi, A. S. Biris, and V. P. Zharov, "Super-resolution nonlinear photothermal microscopy," Small 10(1), 135-142 (2014).
17 V. Zharov, V. Galitovsky, and M. Viegas, "Photothermal detection of local thermal effects during selective nanophotothermolysis," Applied Physics Letters 83(24), 4897-4899 (2003).
18 V. P. Zharov, E. N. Galitovskaya, C. Johnson, and T. Kelly, "Synergistic enhancement of selective nanophotothermolysis with gold nanoclusters: potential for cancer therapy," Lasers in Surgery and Medicine 37(3), 219-226 (2005).
19 B. Khlebtsov, V. Zharov, A. Melnikov, V. Tuchin, and N. Khlebtsov, "Optical amplification of photothermal therapy with gold nanoparticles and nanoclusters," Nanotechnology 17(20), 5167-5179 (2006).
20 V. P. Zharov, K. E. Mercer, E. N. Galitovskaya, and M. S. Smeltzer, "Photothermal nanotherapeutics and nanodiagnostics for killing of bacteria targeted with nanoparticles," Biophysical Journal 90(2), 619-627 (2006).
21 V. K. Pustovalov, A. S. Smetannikov, V. P. Zharov, "Photothermal and accompanied phenomena during selective nanophotothermolysis with gold nanoparticles and laser pulses," Laser Physics Letters 5(11), 775-792 (2008).

22 J. Shao, R. J. Griffin, E. I. Galanzha, J.-W. Kim, N. Koonce, J. Webber, T. Mustafa, A. S. Biris, D. A. Nedosekin, and V. P. Zharov, "Photothermal nanodrugs: potential of TNF-gold nanospheres for cancer theranostics," Scientific Reports 3(1), 1293 (2013).
23 R. R. Letfullin, C. Joenathan, T. F. George, and V. P. Zharov, "Laser-induced explosion of gold nanoparticles: potential role for nanophotothermolysis of cancer," Nanomedicine 1(4), 473-480 (2006).
24 M. Everts, V. Saini, J. L. Leddon, R. J. Kok, M. Stoff-Khalili, M. A. Preuss, C. L. Millican, G. Perkins, J. M. Brown, H. Bagaria, D. E. Nikles, D. T. Johnson, V. P. Zharov, and D. T. Curiel, "Covalently linked Au nanoparticles to a viral vector: potential for combined photothermal and gene cancer therapy," Nano Letters 6(4), 587-591 (2006).
25 A. Mertiri, H. Altug, M. K. Hong, P. Mehta, J. Mertz, L. D. Ziegler, and S. Erramilli, "Nonlinear midinfrared photothermal spectroscopy using Zharov splitting and quantum cascade lasers," ACS Photonics 1(8), 696-702 (2014).
26 E. I. Galanzha, M. G. Viegas, T. I. Malinsky, A. V. Melerzanov, M. A. Juratli, M. Sarimollaoglu, D. A. Nedosekin, and V. P. Zharov, "In vivo acoustic and photoacoustic focusing of circulating cells," Scientific Reports 6(1), 21531 (2016).
27 Noninvasive Cytophone device detects melanoma in earliest stages, could prevent fatal disease spread.

Miniature optical fiber sensors using surface enhanced Raman spectroscopy (SERS) for remote biochemical sensing

Aditya H. Pandya[1], Joseph C. Kumaradas[1], and Alexandre Douplik[1,2,3*]

[1] Department of Physics, Ryerson University, Toronto, ON, M5B 2K3, Canada

[2] Institute for Biomedical Engineering, Science and Technology (iBEST), St. Michael's hospital, Toronto, ON, M5B 1W8, Canada

[3] Keenan Research Centre for Biomedical Science of St. Michael's Hospital, Toronto, ON, M5B 1T8, Canada

*** e-mail:** douplik@ryerson.ca

Abstract. In this study, we present facile fabrication of a miniaturized remote sensing SERS platform using highly tunable Nano-Sphere Lithography (NSL) technique. Using 200 μm diameter optical fibers with high numerical aperture (0.5NA), the SERS enhancement of remote sensing was found to be 98% of direct sensing configuration. Standard silica optical fibers were used for remote sensing using SERS without additional need of optical filtering to mitigate fluorescence and Raman background of these fibers which allows fabrication of miniaturized remote sensing platforms that can be used for remote biochemical sensing. © 2019 Journal of Biomedical Photonics & Engineering.

Keywords: SERS; Plasmonics; Nanoparticles; Nanosphere lithography; Remote fiber sensing.

Paper #3303 received 13 Nov 2018; revised manuscript received 26 Jan 2019; accepted for publication 27 Jan 2019; published online 9 Feb 2019. doi: 10.18287/JBPE19.01.010301.

1 Introduction

Raman spectroscopy (RS) is a widely used analytical technique that provides a molecular vibrational fingerprint of the analyte being examined based on inelastic scattering of light [1]. It has been successfully used in a wide range of applications such as detecting explosives, process analytical techniques and, medical endoscopy [2-5]. Remote sensing using RS poses a major challenge as it is a very weak process and intrinsic fluorescence routinely interferes with RS data collection because it is 4 to 5 orders of magnitude larger in magnitude [6]. Furthermore, miniaturizing RS probes in a form factor less than a millimeter leads to low signal throughput limiting the detection sensitivity. Remote sensing in microfluidic platforms, endoscopic devices, and industrial process analytical technologies is routinely desired. Hence, miniaturization of Raman probes is necessary while maintaining proper signal-to-background ratio allowing for efficient collection of RS spectra.

Standard silica based optical fibers produce large fluorescence background [7]. This is eliminated by using optical filters to limit excited optical fiber fluorescence through a laser line filter and backscattered Rayleigh light using a dichroic/notch filter at the fiber tip [7] These filters are expensive to manufacture and hard to miniaturize. Sapphire based optical fibers (SOF) and photonic crystal/hollow core optical fibers (PCF) have been proposed to minimize the background [8, 9]. Both SF and PCF are expensive to handle and manufacture while PCFs also have lower collection efficiencies and limited operational bandwidth. Thus, standard silica based optical fibers are lucrative for creating low cost (a few dollars/meter) and disposable RS platforms due to their wide availability with varying collection efficiencies.

Surface Enhanced Raman Spectroscopy (SERS) has been used to enhance the inherently weak Raman scattering and the large enhancement factors by SERS have resulted in lower limits of detection (up to single molecule sensitivity) [10-12]. SERS has been performed primarily using nanoparticles suspended in a solution mixed with an analyte or nanoparticles localized on a substrate that is incubated with the analyte [12,13]. SERS substrates need to be designed for single use to

limit cross contamination and to avoid physical and chemical degradation of substrates over time [14]. Using SERS with standard silica optical fibers presents a unique opportunity to extend the usage of optical fibers toward unfiltered RS probes.

Nanosphere lithography (NSL) is a versatile technique for fabricating nanostructures [15]. At first, a tightly packed array of nanospheres is created using dip coating, spin coating or assembly at the interface of two media [16]. After the self-assembly process, SERS active substrates are fabricated using two approaches: 1) Through deposition of a metal film over the nanosphere array to create metal film over nanospheres (MFON) substrates, and 2) Depositing a metal film over the nanosphere array and then removing nanosphere array mask to create periodic nanotriangle arrays matching the shape of the gap in between the tightly packed nanosphere array. Periodic nanotriangle arrays provide wavelength tunability and control of surface area that can be more suitable for quantitative calculation of enhancement factors and performing theoretical calculations of electromagnetic enhancements [17]. Since the size of nanospheres used as mask can be altered, nanoparticle size and distance between particles can be changed which allows for coupling effects between periodic particle arrays allowing for larger enhancements [18]. Thus, NSL is an inexpensive fabrication technique with flexible tunability that can be used for low cost disposable platforms with arbitrary and miniscule geometries.

Recently, more efforts have been focused on using SERS for remote sensing. Various studies have focused on creating optical fibers for remote SERS sensing. These include etched imaging fiber bundles coated with silver films [19], oblique angle deposition of silver films onto fiber tips [20], laser induced self-assembly of Ag nanocubes in a meniscus [21] and, D-shaped fiber tips ablated with femtosecond lasers to create SERS sensors [22]. Trapping nanospheres on fiber surfaces was achieved by Stokes et al. [23] and NSL for SERS on fiber tips was used more recently by Pisco et al. [24]. They focused on improved etching techniques to perform controlled nanoparticle formation and were performed directly on the NSL fabricated SERS tips inside a ferrule and remote sensing was not focused during these studies. A recent study performed by Quero et al. [25] characterized planar substrates using metal film over nanospheres and evaluated background generated by various optical fibers to indicate that fiber-optic optrodes can be created using their approach. Metal film over nanosphere substrates are robust but, they do not allow tunability and the presence of nanospheres on the fiber tips can result in generation of additional background peaks from Polystyrene to interfere with data collection [17, 26]. Moreover, using confocal Raman microscopes, as used by Quero et al., collection of spectra from a large area (such as 200μm optical fibers) is difficult due to rejection of photons because the confocal aperture is smaller than the projected image of the optical fiber on confocal imaging plane.

In this study, optical fiber SERS sensors are fabricated using NSL by removing nanospheres to create nanotriangles. Different Numerical Apertures (NA) were used in a remote sensing configuration using crystal violet (CV) dye as an analyte to test the feasibility of creating a disposal fiber SERS platform. A custom data collection setup was created to acquire spectra from the full diameter of the optical fibers (200 μm) to ascertain the projected image of the optical fiber matches the aperture of the collection optical fiber.

2 Methods

A custom designed Raman collection setup optimized for fiber excitation and collection was used. A 40× microscope objective (0.65 NA, Motic, China) was used to focus the collimated laser (785 nm, Ondax Inc, USA) into a 30 μm spot size on the fiber (Fig. 1D). Since the optical fiber was 200μm in diameter, the excitation spot was centered onto the fiber and a dichroic beamsplitter was used to direct light to and from the sample into a spectrometer. A fiber coupled high throughput spectrometer (16 bit digitization, Hyperflux PRO, Tornado Spectral Systems, Canada) was used to collect the Raman spectra (integration time 1 s). The collection was done using a 1 mm optical fiber due to the magnification achieved using a combination of 40× microscope objective and a coupling lens which resulted in collection of spectra from the whole diameter of the optical fiber. Calibration of the spectrum was performed using a silicon disc to account for laser variations. Laser power was measured at the sample using a thermal power sensor (PM160T, Thorlabs, USA). The fiber was micro-positioned to achieve the maximum detected signal at the spectrometer.

Standard silica based optical fibers were purchased from Thorlabs (NJ, USA) and were cut to 15 cm length. Optical fibers were made of silica glass as a concentric core, cladding and coating/buffer (for support) tube. For 200 μm core optical fibers used in this study, the cladding is 25 μm thick and the coating ranges from 100 μm to 275 μm. Fibers with a range of numerical apertures (0.22, 0.39 and 0.5) were used. The optical fibers used in this study contain a low OH concentration which was found to provide the lowest fluorescence/Raman background [27]. A fiber stripper tool was used to strip the coating from both ends. Fiber tips were prepared by scoring them using a fiber scribe (S90R, Thorlabs, NJ, USA) and pulling them to create flat cleaves (Fig. 1A & B). The prepared tips were sonicated in ethanol solution for 5 minutes and then rinsed off with Miili-Q ultrapure water. The optical fibers were then treated with oxygen plasma (5 minutes – High setting, PDC-32 G – 150W, Harrick Plasma, USA) to further prepare the fiber tips for NSL by improving their hydrophilic properties. The prepared tips were immediately soaked in an ultrapure water solution.

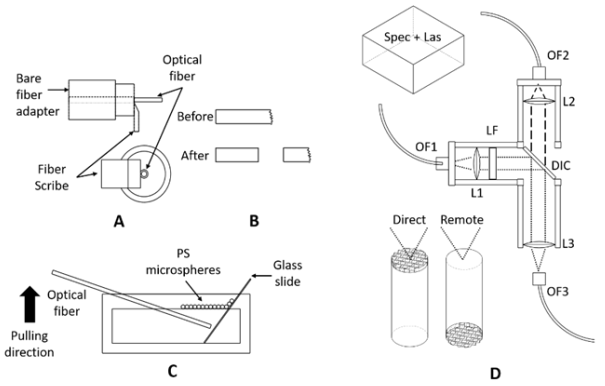


Fig. 1 Fabrication of SERS fibers and RS collection setup (A) Optical fiber guided into a bare fiber adapter with 1 cm tip protruding through the bore. A fiber scribe scores the fiber tip perpendicularly at the base guided by the ferrule surface. (B) The fiber is then pulled so that it breaks at score line to obtain a flat fiber tip. (C) The plasma treated fiber tip is immersed into a water bath containing a glass slide. PS microspheres are dispersed onto the surface of water through controlled deposition via the glass slide. Upon formation of a monolayer, the optical fiber is pulled out of the water bath to transfer the monolayer onto the fiber tip. (D) Using a 105 µm optical fiber (OF1), laser light is collimated using lens (L1) and filtered using a band pass laser line filter (LF). The collimated laser light passes through a dichroic mirror (DIC) which reflects the laser lights on the SERS fiber (OF3) in direct or remote configurations. Red shifted wavelengths passed through the DIC and another lens (L2) focused light into a 1mm optical fiber which is connected to a Raman spectrometer.

To perform NSL, a plasma treated microscopic glass slide was placed in a custom Polytetrafluoroethylene (PTFE) tank filled with water and the optical fiber was lowered into the water at an oblique angle 10 using a 3D translation stage (MTS50-Z8, Thorlabs, NJ, USA) as depicted in Fig. 1C. 5 µL solution of 50% ethanol and 50% polystyrene microsphere solution (5 µm – 4 wt%) ThermoFisher, USA) was pipetted onto the glass slide and the spheres transferred from the glass slide onto the water surface (Fig. 1C). The process was repeated until the surface was filled with microspheres and an iridescent pattern was obtained. A PTFE bar was used to sweep the surface for a tighter packed monolayer. Once a monolayer was achieved, the optical fiber was pulled out at a steady rate of 10 µm/s as depicted in Fig. 1C. The slow draw of the optical fiber allows the spheres to be coated onto the fiber tip gradually. Sputter coating (Denton Desk IV) was used to coat 25 nm Au layer on the tightly packed monolayer and ultrasonication was used to remove polystyrene nanospheres.

Fig. 2 shows the background signals from prepared optical fibers. The background from 0.22 NA fiber was consistently distinct from the other fibers showing some interference from fiber coating which was made of acrylate. In general, the region higher than 1300 cm^{-1} was free from the background generated by the optical fiber. The fluorescence intensity was highest for 0.5 NA below 700 cm^{-1}. The trend was opposite for higher wavenumbers which can be attributed to the variation in material properties of the optical fibers. The laser power at the focal spot was 16 mW and the power output through the fiber was 3.6 mW, 8.2 mW and 12.4 mW for 0.2 NA, 0.39 NA and 0.5 NA respectively.

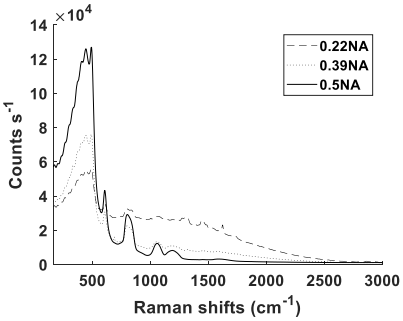


Fig. 2 Background spectra from optical fibers normalized by the integration time.

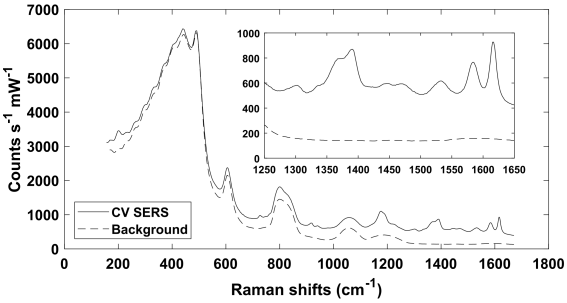


Fig. 3 Background suppression performed via iteratively fitting and removing the known background spectrum from the collected SERS spectrum.

An iterative algorithm with non-negative constraint was used to match the background spectra to the collected SERS spectra. For this study, a fiber background was experimentally obtained, and a simple subtraction resulted in either negative values of intensity or improper suppression of the background. To improve the background suppression, a simple iterative algorithm with non-negative constraints was used to match the background spectra to the collected SERS spectra. The background spectrum was multiplied iteratively by a factor. The factor was initialized to 1 and in each iteration, the factor is increased or decreased by 0.001 depending on the background being larger or smaller than the SERS spectra until the difference is minimized and non-negative (Fig. 3). This allowed to perform an optimized matching of the fiber backgrounds to the SERS spectra. The spectrum was multiplied iteratively by a factor of 0.001. In each iteration, the background spectrum was subtracted from or added to the SERS spectrum (depending on the background being larger or smaller than the SERS spectra) until the difference was minimized and non-negative. All the SERS intensity comparisons were performed on raw spectra and background suppression was mainly used for visualizing the peaks.

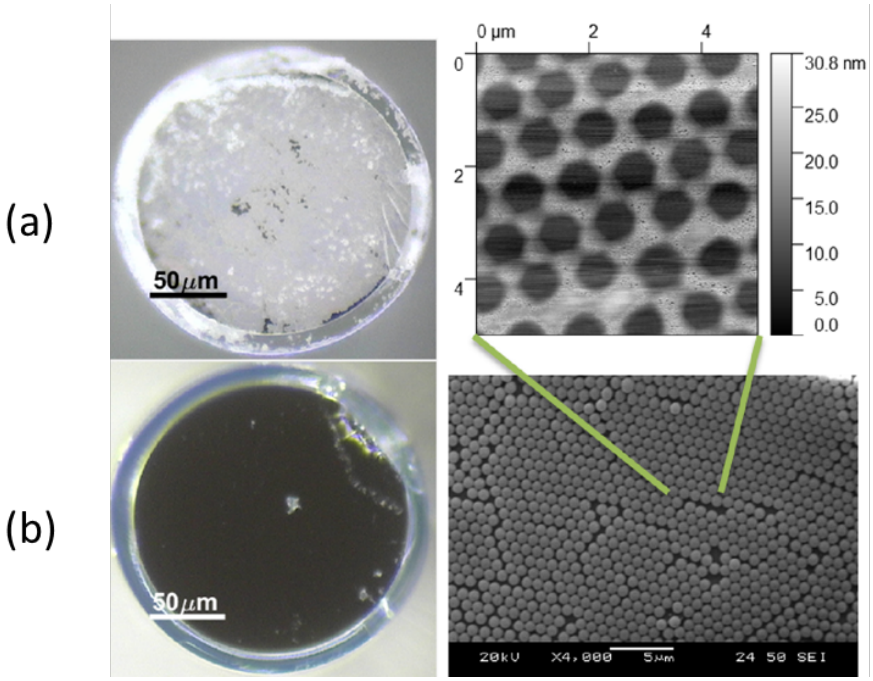


Fig. 4 The left column shows microscopic images of prepared fiber tips which are coated with PS microspheres (a) and uncoated (b). The notch on the top right indicates the location of the fiber score. The right column depicts an AFM image (c) corresponding to the SEM image (d).

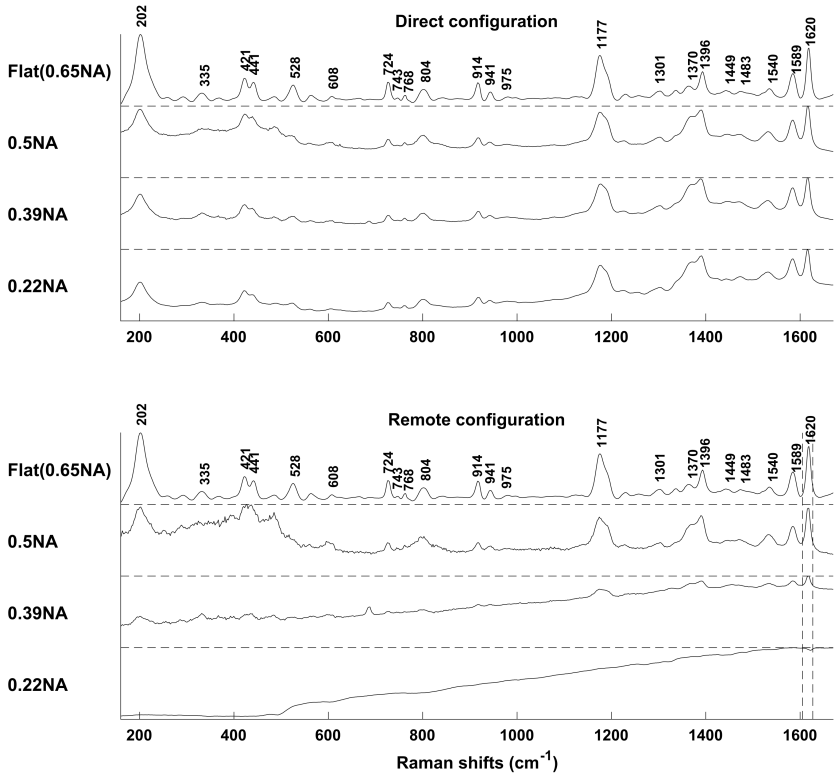


Fig. 5 The spectra are arranged in decreasing order of NA from top to bottom. The topmost spectrum was acquired using a flat substrate fabricated on a microscopic cover slip. The vertical dashed lines in the remote configuration mark the peak that was used to compare the peak intensity for different NA. The spectra are normalized (the scales of each subplot separated by dashed horizontal lines is between 0 and 1) for better depiction of peaks. (a) shows results for direct SERS acquisition configuration and (b) shows results for remote SERS acquisition configuration.

3 Results and discussion

Fig. 4 shows the stages of NSL fabrication and evaluation. The optical fibers were treated with oxygen plasma to prepare the fiber tips for NSL by improving their hydrophilic properties [28] before the fabrication process. This aided in the formation of a monolayer of the polystyrene (PS) microspheres to form an effective mask. Flat cleaved optical fibers were imaged before (Fig. 4b) and after (Fig. 4a) NSL fabrication. The optical image showed full coverage of the fiber tip and corresponding SEM image (Fig. 4d) revealed the monolayer formation. AFM image (Fig. 4c) depicts the hexagonal periodic array of curved triangular Au nanoparticles created after removal of the polystyrene mask. Line defects (line-like discontinuities in the tightly packed hexagonal lattice structure) were observed in the SEM images which are characteristic to the NSL fabrication process. NSL was also performed on square microscopic cover slips 22 mm×22 mm×0.17 mm made of silica glass.

Following the fabrication of SERS fibers, their performance was evaluated by using Crystal Violet (CV) as an analyte. For maximal efficiency of SERS, the SERS optical fibers and flat substrates were immersed in 244 μM Crystal Violet (CV) solution for 3 hours and were rinsed with ultra-pure water for 30 s to remove non-adsorbed CV molecules from the surface before performing spectral measurements. For SERS fibers, Raman spectra were collected in the direct (laser incident on the nanofabricated face directly) and remote configurations (laser incident on the remote face opposite to the nanofabricated face). Fig. 5 depicts the spectra obtained through direct and remote configurations. In the direct configurations, acquired spectra for all fiber NAs were within 15% intensity variation (from the maximum value) confirming the similar performance of the nanostructured tips for all three cases when illuminated directly on the fabricated tips. All the spectra obtained were normalized by the integration time and the laser power coupled through the optical fibers for different NA values. All spectra were corrected for background for visualization purposes as described in the methods section. The optical fibers exhibit strong background below 1100 cm^{-1}. This decreases the quality of Raman spectra below this range. Fig. 6 compares integrated intensity calculated using the tangent skim approach [29] of the peak centered at 1620 cm^{-1} in the region depicted by the dashed vertical lines in Fig. 5. This was chosen to ensure minimal interference from the background signals generated by the optical fiber. As the collection efficiency of a fiber scales to the square of the NA, a trendline (NA^2) is presented that depicts the trend of integrated Raman intensity. The integrated peak intensity variation shows good agreement with the trend-line.

For non-SERS spectral collection, fiber probes were immersed in CV solution and spectra were collected from the fibers remotely through the distal end $I_{\mathrm{RS}}^{\mathrm{fiber}}$. These spectra were used as non-SERS spectra for both remote and direct configurations since the fibers did not have any patterned surfaces. For flat glass substrates, instead of immersion, a 10μL of CV droplet was placed on the substrate for spectral collection $I_{\mathrm{RS}}^{\mathrm{flat}}$. This allowed for data to be acquired for spontaneous Raman scattering with glass background. For SERS spectral collection, spectra were acquired from fabricated flat SERS substrates $I_{\mathrm{SERS}}^{\mathrm{flat}}$ and SERS fiber probes in the remote ($I_{\mathrm{SERS}}^{\mathrm{remote}}$) and direct ($I_{\mathrm{SERS}}^{\mathrm{direct}}$) configurations. All SERS substrates were immersed in CV solution for 3 hours and then rinsed before collecting spectra.

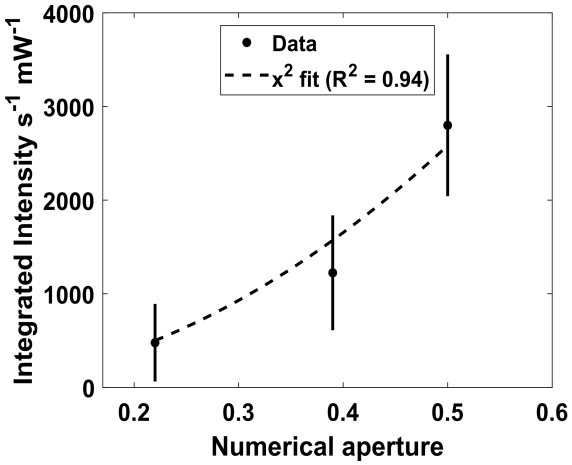


Fig. 6 Integrated peak corresponding to the dashed lines in Fig. 5 depicted against NA^2 trendline. The vertical lines for each point represent ±1 standard deviation.

For practical performance evaluation, Intensity Enhancement Factors (IEF) were calculated using the following equations

$$IEF^{\mathrm{direct}} = \frac{\mathrm{I}_{\mathrm{SERS}}^{\mathrm{direct}}}{\mathrm{I}_{\mathrm{RS}}^{\mathrm{fiber}}},$$
$$IEF^{\mathrm{remote}} = \frac{\mathrm{I}_{\mathrm{SERS}}^{\mathrm{remote}}}{\mathrm{I}_{\mathrm{RS}}^{\mathrm{fiber}}}, \quad (1)$$
$$IEF^{\mathrm{flat}} = \frac{\mathrm{I}_{\mathrm{SERS}}^{\mathrm{flat}}}{\mathrm{I}_{\mathrm{RS}}^{\mathrm{flat}}}.$$

IEF^{direct} was calculated as 31 and 37 for 0.39 NA and 0.5 NA optical fibers respectively. IEF^{remote} was found to be 11 and 36 for 0.39 NA and 0.5 NA optical fibers respectively. The IEF^{remote} for 0.5 NA was 98% of IEF^{direct} showing that 0.5 NA performed similar in remote and direct configurations. The IEF^{remote} for 0.39 NA was 35% of IEF^{direct} showing that for 0.39 NA, performance degraded in the remote configuration when compared to 0.5 NA. The IEF^{flat} was found to be 30 indicating that the 0.5 NA fiber performed slightly better which can be attributed to the larger area of collection. SERS was shown to partially mitigate the fluorescence background allowing fabrication of unfiltered miniscule Raman probes. Increasing the NA improved the signal-to-background ratio for optimized collection. Since the magnitude of fluorescence scales with the path length of light in the fiber, the fiber

lengths used in this study were 15cm (±1cm). These lengths are generally acceptable when being inserted into cavities as well as small microfluidic devices. Flat glass SERS substrates with NSL as well as fiber substrates were fabricated using the same masks. Non-patterned substrates were also used as control to identify the enhancements achieved. For highest SERS efficiency, a disposable SERS fiber is necessary and thus a low-cost, tunable and reproducible manufacturing process was warranted. NSL technique allows for low-cost, tunable and rapid fabrication procedure with a wide range of enhanced fabrication techniques. Thus, using NSL to create SERS optical fiber sensors is very lucrative to design tailored disposable probes for usage in miniscule and arbitrary sampling environments.

4 Conclusion

Disposable SERS fiber probes were fabricated using the NSL technique. Increasing the NA was found to resolve Raman spectra for a wide range of wavenumbers. Direct measurements show similar SERS performance of the optical fibers for all different NAs while remote measurements show that larger NA is required to obtain better Raman characterization. Hence, NA plays a significant role in fabricating SERS fiber probes. A simple iterative matching algorithm with non-negative constraints was sufficient at removing the fluorescence background from the optical fibers. Characterization of SERS optical fibers showed that 0.5 NA had same performance in direct/remote configurations and had the largest enhancement factors indicating advantages of using a high NA optical fiber for SERS measurements. CV dye was used for a proof of concept to observe the performance of SERS fiber probes in a remote sensing configuration and further experiments should be performed to optimize NSL process and evaluate the limit of detection. This platform can be optimized by changing the size of the microspheres for NSL as well as using advanced etching techniques. Using NSL, bare optical fibers with SERS tips can be easily fabricated and employed for remote sensing. It is envisioned that these fibers can be readily used in miniature environments such as microfluidic devices, and endoscopic devices to perform SERS sensing.

Disclosures

All authors declare that there is no conflict of interests in this paper.

Acknowledgements

Authors would like to acknowledge the support for this study from NSERC Discovery grant (Douplik), Ryerson Health Fund, NSERC Engage support, and infrastructural support from Institute for Biomedical Engineering, Science and Technology (IBEST), a partnership between Ryerson University and St. Michael's Hospital (Toronto).

References

1. C. V Raman, K. S. Krishnan, "A New Type of Secondary Radiation," Nature 121(3048), 501-502 (1928).
2. X. Fan, I. M. White, "Optofluidic Microsystems for Chemical and Biological Analysis," Nature Photonics 5(10), 591-597 (2011).
3. C. Eliasson, N. A. Macleod, and P. Matousek, "Noninvasive detection of concealed liquid explosives using Raman spectroscopy," Analytical Chemistry 79(21), 8185-8189 (2007).
4. S. Ben-Jaber, W. J. Peveler, R. Quesada-Cabrera, C. W. O. Sol, I. Papakonstantinou, and I. P. Parkin, "Sensitive and specific detection of explosives in solution and vapour by surface-enhanced Raman spectroscopy on silver nanocubes," Nanoscale 9(42), 16459-16466 (2017).
5. K. A. Esmonde-White, M. Cuellar, C. Uerpmann, B. Lenain, and I. R. Lewis, "Raman spectroscopy as a process analytical technology for pharmaceutical manufacturing and bioprocessing," Analytical Bioanalytical Chemistry 409(3), 637-649 (2017).
6. M. Jermyn, J. Desroches, K. Aubertin, K. St-Arnaud, W.-J. Madore, E. De Montigny, M.-C. Guiot, D. Trudel, B. C. Wilson, K. Petrecca, and F. Leblond, "A review of Raman spectroscopy advances with an emphasis on clinical translation challenges in oncology," Physics in Medicine and Biology 61(23), R370–R400 (2016).
7. I. Latka, S. Dochow, C. Krafft, B. Dietzek, and J. Popp, "Fiber optic probes for linear and nonlinear Raman applications - Current trends and future development," Laser & Photonics Reviews 7(5), 698-731 (2013).
8. L. Yuan, X. Lan, J. Huang, H. Wang, L. Jiang, and H. Xiao, "Comparison of silica and sapphire fiber SERS probes fabricated by a femtosecond laser," IEEE Photonics Technology Letters 26(13), 1299-1302 (2014).
9. S. O. Konorov, C. J. Addison, H. G. Schulze, R. F. B. Turner, and M. W. Blades, "Hollow-core photonic crystal fiber-optic probes for Raman spectroscopy," Optics Letters 31(12), 1911-1913 (2006).
10. E. C. Le Ru, E. J. Blackie, M. Meyer, and P. G. Etchegoin, "Surface Enhanced Raman Scattering Enhancement Factors: A Comprehensive Study," The Journal of Physical Chemistry C 111(37), 13794-13803 (2007).
11. K. Kneipp, H. Kneipp, R. Manoharan, E. B. Hanlon, I. Itzkan, R. R. Dasari, and M. S. Feld, "Extremely large enhancement factors in surface-enhanced Raman scattering for molecules on colloidal gold clusters," Applied Spectroscopy 52(12), 1493-1497 (1998).
12. P. Mosier-Boss, "Review of SERS Substrates for Chemical Sensing," Nanomaterials 7(6), 142 (2017).

13. B. Sharma, M. Fernanda Cardinal, S. L. Kleinman, N. G. Greeneltch, R. R. Frontiera, M. G. Blaber, G. C. Schatz, and R. P. Van Duyne, "High-performance SERS substrates: Advances and challenges," MRS Bulletin 38(8), 615-624 (2013).
14. L. Yang, P. Li, and J. Liu, "Progress in multifunctional surface-enhanced Raman scattering substrate for detection," RSC Advances 4(91), 49635-49646 (2014).
15. J. C. Hulteen, R. P. Van Duyne, "Nanosphere lithography: A materials general fabrication process for periodic particle array surfaces," Journal of Vacuum Science & Technology A: Vacuum, Surfaces, and Films 13(3), 1553-1558 (1995).
16. P. Colson, C. Henrist, and R. Cloots, "Nanosphere Lithography: A Powerful Method for the Controlled Manufacturing of Nanomaterials," Journal of Nanomaterials 2013, 1-19 (2013).
17. J. A. Dieringer, A. D. McFarland, N. C. Shah, D. A. Stuart, A. V. Whitney, C. R. Yonzon, M. A. Young, X. Zhang, and R. P. Van Duyne, "Introductory Lecture : Surface enhanced Raman spectroscopy: new materials, concepts, characterization tools, and applications," Faraday Discussions 132, 9-26 (2006).
18. C. L. Haynes, A. D. McFarland, L. Zhao, R. P. Van Duyne, G. C. Schatz, L. Gunnarsson, J. Prikulis, B. Kasemo, and M. Käll, "Nanoparticle Optics: The Importance of Radiative Dipole Coupling in Two-Dimensional Nanoparticle Arrays†," The Journal of Physical Chemistry B 107(30), 7337-7342 (2003).
19. D. J. White, and P. R. Stoddart, "Nanostructured optical fiber with surface-enhanced Raman scattering functionality," Optics Letters 30(6), 598-600 (2005).
20. J. S. Hartley, S. Juodkazis, and P. R. Stoddart, "Optical fibers for miniaturized surface-enhanced Raman-scattering probes," Applied Optics 52(34), 8388-93 (2013).
21. Y. Liu, Z. Huang, F. Zhou, X. Lei, B. Yao, G. Meng, and Q. Mao, "Highly sensitive fibre surface-enhanced Raman scattering probes fabricated using laser-induced self-assembly in a meniscus," Nanoscale 8(20), 10607-10614 (2016).
22. Z. Yin, Y. Geng, Q. Xie, X. Hong, X. Tan, Y. Chen, L. Wang, W. Wang, and X. Li, "Photoreduced silver nanoparticles grown on femtosecond laser ablated, D-shaped fiber probe for surface-enhanced Raman scattering," Applied Optics 55(20), 5408-5412 (2016).
23. D. L. Stokes, T. Vo-Dinh, "Development of an integrated single-fiber SERS sensor," Sensors and Actuators B: Chemical 69(1-2), 28-36 (2000).
24. M. Pisco, F. Galeotti, G. Quero, G. Grisci, A. Micco, L. V. Mercaldo, P. D. Veneri, A. Cutolo, and A. Cusano, "Nanosphere lithography for optical fiber tip nanoprobes," Light: Science & Applications 6(5), 1–13 (2017).
25. G. Quero, G. Zito, S. Managò, F. Galeotti, M. Pisco, A. C. De Luca, and A. Cusano, "Nanosphere lithography on fiber: Towards engineered lab-on-fiber SERS optrodes," Sensors 18(3), 680 (2018).
26. X. Zhang, C. R. Yonzon, M. A. Young, D. A. Stuart, and R. P. Van Duyne, "Surface-enhanced Raman spectroscopy biosensors: excitation spectroscopy for optimisation of substrates fabricated by nanosphere lithography," IEEE Proc. - Nanobiotechnology 152(6), 195 (2005).
27. L. F. Santos, R. Wolthuis, S. Koljenović, R. M. Almeida, and G. J. Puppels, "Fiber-optic probes for in vivo Raman spectroscopy in the high-wavenumber region," Analytical Chemistry 77(20), 6747-6752 (2005).
28. A. U. Alam, M. M. R. Howlader, and M. J. Deen, "The effects of oxygen plasma and humidity on surface roughness, water contact angle and hardness of silicon, silicon dioxide and glass," Journal of Micromechanics and Microengineering 24(3), 035010 (2014).
29. J. F. Rusling, "Minimizing errors in numerical analysis of chemical data," Journal of Chemical Education 65(10), 863 (1988).

Differentiation of basal cell carcinoma and healthy skin using multispectral modulation autofluorescence imaging: A pilot study

Nikita V. Chernomyrdin[1,2*], Anastasiya D. Lesnichaya[2], Egor V. Yakovlev[2], Konstantin G. Kudrin[3], Olga P. Cherkasova[4], Elena N. Rimskaya[2,3], Vladimir N. Kurlov[5], Valeriy E. Karasik[2], Igor V. Reshetov[3], Valery V. Tuchin[6,7,8], and Kirill I. Zaytsev[1,2§]

[1] Prokhorov General Physics Institute of the Russian Academy of Sciences, Moscow 119991, Russia
[2] Bauman Moscow State Technical University, Moscow 105005, Russia
[3] Sechenov University, Moscow 119991, Russia
[4] Institute of Laser Physics of Siberian Branch of RAS, Novosibirsk 630090, Russia
[5] Institute of Solid State Physics of RAS, Chernogolovka 142432, Moscow Obl., Russia
[6] Saratov State University, Saratov 410012, Russia
[7] Tomsk State University, Tomsk 634050, Russia
[8] Institute of Precision Mechanics and Control of the Russian Academy of Sciences, Saratov 410028, Russia

*** e-mail:** chernik-a@yandex.ru

§ e-mail: kirzay@gmail.com

Abstract. An approach for differentiating basal cell carcinoma (BCC) and healthy skin by combining a multispectral modulation autofluorescence imaging with the linear discriminant analysis has been proposed. The experimental setup, which employs a 365-nm narrowband excitation, 4 replaceable bandpass filters and a digital camera, has been assembled and applied to study freshly excised samples of BCC. In the experimental setup, modulation of the UV-excitation and demodulation of the visible light images allow for both increasing a signal-to-noise ratio and suppressing a non-fluorescence background in the autofluorescence images of tissues. The observed results demonstrate an ability for distinguishing both ordinary and keratinized BCC from healthy skin justifying the perspectives of the multispectral modulation autofluorescence imaging use for non-invasive and intraoperative diagnosis of BCC and other low-pigmented malignancies of the skin. © 2019 Journal of Biomedical Photonics & Engineering.

Keywords: multispectral fluorescence imaging; autofluorescence phenomenon; medical diagnosis; basal cell carcinoma; linear discriminant analysis.

Paper #3309 received 17 Dec 2018; accepted for publication 20 Mar 2019; published online 27 Mar 2019. doi: 10.18287/JBPE19.05.010302.

1 Introduction

In the past decades, a rapid development of fluorescent spectroscopy, imaging and microscopy has been observed [1–3]. The list of fluorescence sensing techniques includes steady-state and time-resolved fluorescence spectroscopy [4], multi-spectral and hyper-spectral imaging [5–10], two-photon fluorescence correlation spectroscopy and imaging [11–14], scattered-light fluorescence microscopy [15–18], etc.

Fluorescence spectra of biological tissues are formed by individual spectra of fluorophores [19]. By studying the shape of the fluorescence spectra or processing the data of multi-spectral fluorescence imaging, one could analyze the biochemical content and metabolic state of tissues, differentiate biological samples, and investigate

its physiological stress sensitivity [4, 20, 21]. Fluorescence spectroscopy and imaging are widely applied in biomedical science and for medical diagnosis in clinics [1, 22, 23], including non-invasive, minimally-invasive and intraoperative diagnosis of cancers. The fluorescence imaging has been recently applied to diagnose malignancies of the colon [24–26], the esophagus [27–29], the gastric [30], the breast [31], the ovarian [32–34] and the brain [35–37].

One of the most promising applications of fluorescence spectroscopy and imaging is non-invasive and least-invasive diagnosis of skin cancers based on excitation either endogenous or exogenous fluorophores [1, 4, 38]. The methods of exogenous fluorescence diagnosis [39] employ various fluorescent dyes, which are injected into the skin, accumulated in cancer cells, fluoresce under a proper illumination, and, in some cases, could provide the photodynamic effect during the subsequent therapy [40–46]. This technique yields high sensitivity; however, it is also characterized by numerous disadvantages significantly limiting its reliability: (i) the procedure of dye delivery is rather time-consuming; (ii) it requires invasive delivery protocols (injection) or minimally-invasive topical or per-oral administration, and its further elimination from patient body; (iii) exogenous fluorescent dyes cannot provide satisfactory differentiation between similar pathologies (i.e. the specificity of the method is not high [4]).

The autofluorescence (AF) spectroscopy and imaging relying on endogenous fluorophores represent non-invasive and fast approach for skin cancers diagnosis. However, due to high pigmentation of pigmentary skin nevi [47] and early malignant melanomas of the skin [48, 49], this method has a significant limitation because of low light penetration depth [4]. The non-melanoma cancers of the skin [50], such as basal cell carcinoma (BCC) and squamous cell carcinoma (SCC), are usually less pigmented and, as a consequence, appear to be promising goal for the AF diagnosis [4, 51–58]. Despite the significant progress in this field of fluorescence biomedical technologies, the development of novel techniques for skin diagnosis based on AF remains a challenging problem.

In this paper, we propose an approach for differentiating BCC and healthy skin using the multispectral modulation AF imaging combined with linear discriminant analysis (LDA). We assemble an experimental setup employing a 365-nm narrowband excitation of the tissue sample AF, 4 replaceable bandpass filters and a digital camera. It allows for both increasing a signal-to-noise ratio and suppressing a non-fluorescent background in the AF images of tissues using modulation of the UV-excitation and demodulation of the AF visible light images. We use the experimental setup to study *in vitro* samples of freshly excised BCC from 6 patients. The results of this pilot study demonstrate ability for distinguishing ordinary and keratinized BCC from healthy skin using the proposed imaging approach. We analyze the accuracy of the tissue differentiation using this multispectral modulation AF imaging. We qualitatively compare the proposed technique with the existing developments in the area of multispectral AF imaging of BCC, which allows us to highlight the potentials of its use for non-invasive and intraoperative diagnosis of BCC and other low-pigmented skin malignancies.

2 Experimental setup

To study the images of non-melanoma skin cancer AF, we assembled a setup for the modulated multi-spectral fluorescence imaging [59, 60]. It includes excitation and detection channels (see Fig. 1).

In the excitation channel, a polychromatic light of a mercury lamp radiates the sample of interest after passing a 365-nm narrowband excitation filter, a rectangular beam homogenizer, and a $f_{\mathrm{mod}} = 5$ Hz mechanical chopper. The homogenizer shapes the UV-beam to rectangular form leading to the spatially-homogeneous irradiance of the sample, which is placed behind a non-fluorescent reference window (see Fig. 1(c)). Despite the polychromatic mercury lump with a total power of 100 W is employed in our study, a monochromatic UV-irradiance of the sample is only about 10 mW/cm^2 fulfilling the guidelines limiting an exposure of the skin *in vivo* to the electromagnetic waves [61], as specifically, the permissible UV-irradiance of the skin is of about 100 mW/cm^2 for a typical measurement time of 10 sec.

The UV-radiation being interacted with tissue via scattering and emittance of fluorescence [62] is comprised of both the sharp line of the residual UV-excitation light and the broadband fluorescence varying for different regions of the sample under study. In the detection channel, a set of the bandpass interference filters and a digital camera are used for detection of the quasi-monochromatic visible light images $I_\lambda(t, \mathbf{x})$ of the object fluorescence, where index λ defines a certain bandpass filter, $\mathbf{x}$ is the radius vector at the image plane, and t is the time. Spectral transparency curves $T(\lambda)$ of the bandpass filters with different central wavelengths $\lambda \simeq 400, 450, 500,$ and 550 nm, respectively, and similar full-width at half-maximum (FWHM) of $\Delta\lambda \simeq 40$ nm for all filters are shown in Fig. 1(b). We select the described set of the bandpass filters from commercially available ones to both almost continuously cover the most intense part of healthy skin and BCC AF spectra [4] and divide AF spectra into four initially-orthogonal ranges – i.e. separate channels of the multispectral imaging. We use a digital camera with complementary metal-oxide-semiconductor (CMOS) sensor and the frame rate of $f_{\mathrm{rep}} = 25$ Hz.

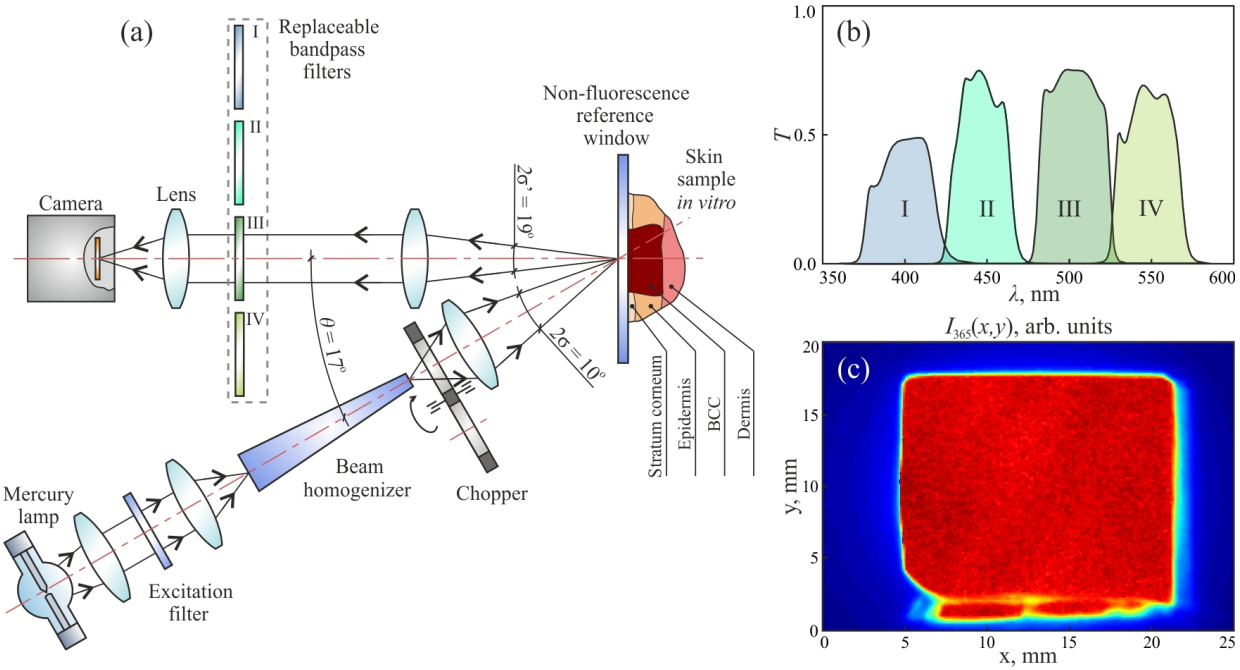


Fig. 1 An experimental setup for the multispectral modulated AF imaging: (a) a scheme of the experimental setup; (b) a spectral transmission of the optical bandpass filters in the detection channel; (c) a spatial distribution of the UV-excitation intensity at the object plane.

In the experimental setup (see Fig. 1), the average angle of the UV radiation incidence on the sample surface (i.e. the angle between the optical axis of the UV-excitation channel and the perpendicular to the sample surface) and the angle of the image detection (i.e. the angle between the optical axis of the imaging channel and the perpendicular to the sample surface) are $\theta \simeq 17°$ and $\theta' \simeq 0°$, respectively. Numerical apertures of the UV-excitation and the fluorescence imaging system are $\mathrm{NA} = 0.09$ ($2\sigma \simeq 10°$) and $\mathrm{NA}' = 0.16$ ($2\sigma' \simeq 19°$), respectively. Along with simplification of the experimental setup and minimization of its dimensions, the use of conventional low-aperture optics in excitation and detection channels allows for providing both a homogeneous irradiance of the sample surface and a spatial resolution of about 0.1 mm at the object plane for the entire field of view.

We perform fluorescence imaging in non-polarized light and assume isotropic character of the sample fluorescence indicatrix. This assumption is correct in case of the small apertures along with the close-to-normal angles of incidence and imaging [63]. At the same time, numerous researches, who are studying the fluorescence of turbid media (including, the fluorescence of tissues), have shown complex polarization-dependent and anisotropic character of this phenomenon [64–70]. By combining optimized geometry of fluorescence excitation and collection with modern fluorescence data processing techniques, one could mitigate an impact of the light scattering in a tissue, reconstruct its intrinsic fluorescence [71–75] and improve an efficiency of fluorescence collection [76–78]. Furthermore, a polarization-dependent character and an anisotropy of tissue fluorescence can serve as a source of additional information for differentiating healthy and pathological tissues [79–81].

During the experimental study, the *in vitro* tissue sample is rigidly fixed behind the non-fluorescent reference window (see Fig. 1(a)). By rigidly fixing the sample surface towards the reference window, we eliminate the influence of various negative factors on the images: (i) an accuracy of the sample positioning; (ii) fluctuations of an incident angle of the UV-radiation; and (iii) non-normal geometry of imaging (i.e. non-orthogonality of the imaging optical axis towards the sample surface). In our work, we consider low-pigmented malignancies of the skin – pigmentation of BCC is insignificant compared to highly-pigmented nevi and melanomas of the skin [4]. Therefore, we neglect the influence of a laterally-inhomogeneous tissue pigmentation on the data of the fluorescence imaging [82].

3 Visible light image processing

Using Fourier-domain analysis, we reconstruct the fluorescence images $f_\lambda(\mathrm{x})$ corresponding to various bandpass filters λ [83]:

$$I_\lambda(t, \mathbf{x}) \propto f_\lambda(\mathbf{x})\,(1 + \sin(2\pi f_{\mathrm{mod}} t)). \quad (1)$$

This technique employs modulation of the UV-radiation intensity and demodulation of the image sequences in the visible range. It yields detecting a set of the sample AF images $f_\lambda(\mathbf{x})$ with both an increased signal-to-noise ratio and a reduced impact of the non-fluorescent background [59, 60]. In order to provide accurate demodulation of the data, a frame rate of the

imaging system f_{img} should be much lower compared to the frame rate of the camera f_{rep} and the modulation frequency f_{mod}. In the described experimental setup (see Fig. 1), the frame rate of the multispectral modulation AF imaging is about $f_{\mathrm{img}} = 0.5$ Hz; it is primarily limited with the inertness of the CMOS sensor and could be further increased (even to real-time operation) by substituting the CMOS camera with the advanced one characterized with improved performance.

In order to study an ability for the differentiation of healthy and pathological tissues using the proposed multispectral AF imaging technique, we examined a set of freshly excised BCC samples provided by the Sechenov University (Moscow, Russia). The tissue samples came from 1 male and 5 female patients aged between 57 and 78 were investigated. The abnormal tissue specimens were investigated within 3 hours after the surgical removal. Classification of the normal skin and BCC tissues was done on the basis of initial clinical diagnosis and proved by a further histological examination of the biopsies. Table 1 summarizes the data on the BCC samples, including the final diagnosis, histological image, patient gender and age, side and size of excision.

Table 1 Data for *in vitro* BCC samples.

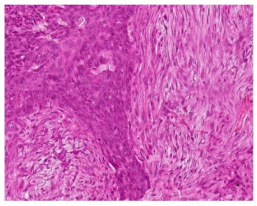
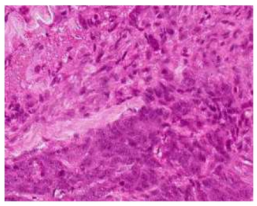
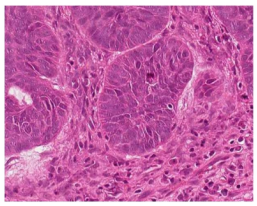
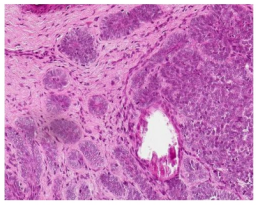
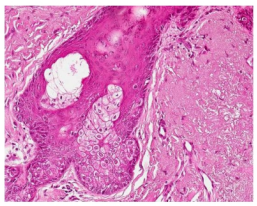
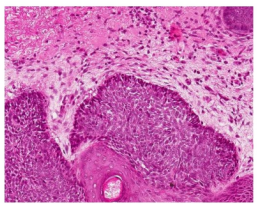
Sample #	Final diagnosis	Patient gender	Patient age	Side of excision	Size of excision	Appearance in paper	Histological image
1	Metatypical BCC with ulceration	Female	59	Back of the head	4.0 cm × 9.0 cm × 1.5 cm	Fig. 2 Fig. 3 Fig. 4(a)	
2	Metatypical BCC with ulceration	Female	63	The cheek	1.5 cm × 3.0 cm × 1.0 cm	Fig. 4(b)	
3	Solid BCC with invasion into dermis	Male	78	The chest	1.7 cm × 1.5 cm × 0.4 cm	Fig. 4(c)	
4	Solid BCC with invasion into dermis	Female	57	The neck	2.0 cm × 2.5 cm × 1.0 cm	Fig. 4(d)	
5	Multicentric BCC with invasion into dermis	Female	73	The nose	3.0 cm × 1.7 cm × 0.4 cm	Fig. 4(e)	
6	Multicentric BCC with invasion into dermis	Female	74	The cheek	4.0 cm × 9.0 cm × 1.5 cm	Fig. 4(f)	

Figure 2 shows results of the multispectral modulation AF imaging of the 1st BCC sample from Table 1. Panel (a) shows digital image of the sample, where the borders mark the healthy skin (I), BCC (II), flake of keratinized BCC (III) and imaged area (IV). Panel (b) visualizes reverse contrast frames from AF image $I_\lambda(t,\mathbf{x})$ at $\lambda = 500$ nm. Panel (c) shows a set of reverse contrast AF images $f_\lambda(\mathbf{x})$ of BCC extracted from the modulated AF sequences (see Eq. (1)). In complete accordance with the Refs. [53, 84], the experimental results show lower AF intensity for the ordinary BCC tissues. At the same time, the highest fluorescence intensity corresponds to the flake of keratinized BCC (region III in Fig. 2(a)).

The theoretical background for distinctive AF changes in cancer tissue was investigated earlier [4, 24, 85, 86]. The altered metabolic state of cancer cells and resulting abnormal concentration of nicotinamide adenine dinucleotide (NADH) were suggested to be the origin of cancer AF changes [86, 87], which allows using the AF phenomenon for discriminating malignancies from normal tissues [87–91]. The changes of the AF spectrum in malignant skin tissues (under the UV-excitation in the spectral range of 260 to 400 nm) were reported to originate from the decreased collagen and elastin content in tissues, as well as from the decreased NADH levels [84, 92–98]. Furthermore, the differences in optical properties of healthy and pathological tissues (i.e. absorption and scattering of the UV-radiation and the fluorescence component) provide the contrast between the healthy skin and BCC in the AF spectra and images, which is originated owing to the listed features of malignant tissues.

A set of the four fluorescence images $f_\lambda(\mathbf{x})$ (see Fig. 2(c)) represents information about the sample AF intensity in different spectral channels. Such data could not be directly used for differentiation of tissues, for example, using simple intensity threshold, since AF intensity depends on a number of factors (the shape of the skin surface, its pigmentation and hydration, and others). For instance, according to the data of Fig. 2(c), the ordinary BCC tissue fluoresces less intensively comparing to the healthy skin; but, oppositely, the keratinized BCC fluoresces much intensively. Therefore, novel approach for tissue segmentation, which does not rely on simple AF intensity analysis should be introduced.

4 LDA-based differentiation of tissues

For differentiation of healthy and abnormal tissues, we perform statistical analysis of normalized fluorescence intensities in all of the four spectral channels using the LDA approach [93, 99] – i.e. a linear transformation technique, which yields reduction of the experimental data dimensionality and maximization of the separation between classes.

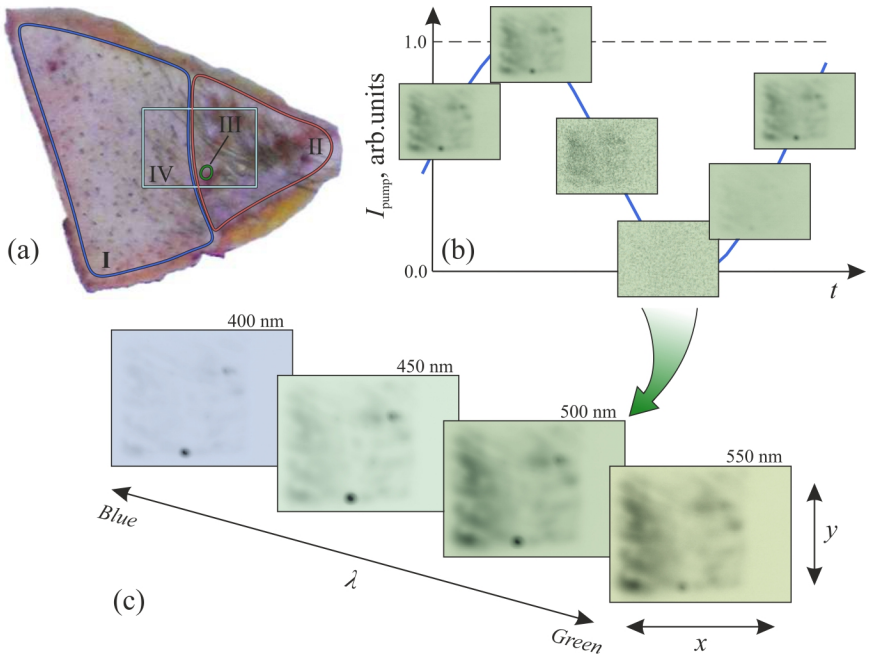


Fig. 2 A multispectral modulation AF imaging of BCC: (a) a clinical photo of the 1st BCC sample (see Table 1), where characters I to IV define the healthy skin, BCC, flake of keratinized BCC and imaging areas, respectively; (b) reverse contrast frames of the multispectral AF image $I_\lambda(t,\mathbf{x})$ at λ =500 nm; (c) reverse contrast demodulated multispectral AF images $f_\lambda(\mathbf{x})$ at λ =400, 450, 500, 550 nm.

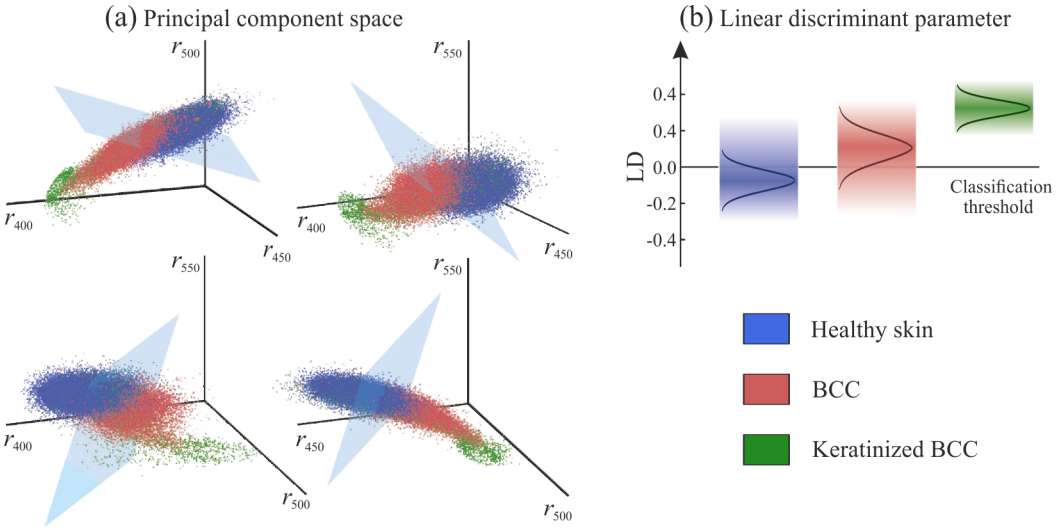


Fig. 3 A statistical analysis of the results of the multispectral modulation AF imaging: (a) a principal component space for the 1st BCC sample (see Fig. 2 and Table 1); (b) LDA space for the 1st BCC sample (see Fig. 2 and Table 1). Classes of the healthy skin, BCC and keratinized BCC are represented with blue, red and green areas, respectively. Light blue 4D plane in (a) and line in (b) show the threshold for discriminating healthy skin and BCC.

We introduce the principal components based on normalized intensities of the tissue AF. The intensities of each $\mathbf{x}_i$-pixel in the AF images $f_\lambda(\mathbf{x})$ define a radius-vector $\mathbf{r}_i$ in a four-dimensional (4D) principal component space

$$\mathbf{r}_i = \left(r_{400,i}, r_{450,i}, r_{500,i}, r_{550,i}\right)^{\mathrm{T}}, \quad (2)$$

where

$$r_{\lambda,i} = \frac{f_\lambda(\mathbf{x}_i)}{\frac{1}{K}\sum_n^K f_n(\mathbf{x}_i)}, \quad (3)$$

is a normalized intensity corresponding to the i^{th}-pixel fluorescence in a certain spectral channel n =400, 450, 500 or 550 nm, and $K = 4$ is a number of the spectral channels. These principal components are basically orthogonal due to initial orthogonality of the spectral transparency curves $T(\lambda)$ of the bandpass filters (see Fig. 1(b)). The full size of the AF image f_λ is $M\times N$ points; thus, it allows for calculating $M\times N$ radius vectors in the principal component space.

Fig. 3(a) demonstrates an example of the principal component space, which is calculated based on the data of the 1st BCC sample imaging (see Fig. 2 and Table 1). Namely, it shows three-dimensional (3D) projections of the four-dimensional principal component space, where various points are colored according to areas of the healthy skin (blue), BCC (red) and keratinized BCC (green). This data set represents a typical character of the principal component plot, which is observed for all BCC samples. The sets of points in the principal component space by BCC and healthy skin tissues form classes, which are principally distinguishable.

We have implemented the Fisher LDA approach [99] to highlight an ability for the differentiation of healthy skin and BCC based on the proposed AF imaging technique. In order to find the procedure of the data projection into the 1D Fisher LDA subspace and to estimate the threshold value, we perform the following data analysis.

- We perform multispectral modulation AF imaging of all six BCC samples (see Table 1).
- We manually choose a number of healthy skin and BCC points in the AF images $f_\lambda(\mathbf{x})$ in order to form healthy skin and BCC classes in the principal component space for further threshold selection. The amounts of healthy skin and BCC points, which are assigned *a priori* basing on the data of histological analysis and expert visual examination, varies from sample to sample. However, this amounts account at least 30 points for each tissue sample and each class.
- Using all the manually selected points, we form two groups of radius vectors $\mathbf{r}_{i,\mathrm{skin}}$, $\mathbf{r}_{i,\mathrm{bcc}}$ representing healthy skin and BCC classes in the principal space. For these two classes, we calculate mean vectors $\langle\mathbf{r}\rangle_{\mathrm{skin}}$, $\langle\mathbf{r}\rangle_{\mathrm{bcc}}$ and scatterers S_{skin}, S_{bcc}:

$$\langle\mathbf{r}\rangle_{\mathrm{skin}} = \frac{1}{N_{\mathrm{skin}}}\sum_i \mathbf{r}_{i,\mathrm{skin}};$$

$$\langle\mathbf{r}\rangle_{\mathrm{bcc}} = \frac{1}{N_{\mathrm{bcc}}}\sum_i \mathbf{r}_{i,\mathrm{bcc}};$$

$$S_{\mathrm{skin}} = \frac{1}{N_{\mathrm{skin}}}\sum_i (\mathbf{r}_{i,\mathrm{skin}} - \langle\mathbf{r}\rangle_{\mathrm{skin}})(\mathbf{r}_{i,\mathrm{skin}} - \langle\mathbf{r}\rangle_{\mathrm{skin}})^{\mathrm{T}};$$

$$S_{\mathrm{bcc}} = \frac{1}{N_{\mathrm{bcc}}}\sum_i (\mathbf{r}_{i,\mathrm{bcc}} - \langle\mathbf{r}\rangle_{\mathrm{bcc}})(\mathbf{r}_{i,\mathrm{bcc}} - \langle\mathbf{r}\rangle_{\mathrm{bcc}})^{\mathrm{T}},$$

where N_{skin} and N_{bcc} are numbers of priory selected points of healthy and abnormal tissues, respectively. Since LDA employs linear data projection into 1D subspace $\mu_i = \mathbf{w}^{\text{T}}\mathbf{r}_i$ (here, $\mathbf{w}^{\text{T}}$ is a projection operator), in 1D space we define the points of healthy skin and BCC classes $\mu_{i,\text{skin}}$, $\mu_{i,\text{bcc}}$, the related mean values $\langle\mu\rangle_{\text{skin}}$, $\langle\mu\rangle_{\text{bcc}}$ and the scatterers s_{skin}, s_{bcc}:

$$\langle\mu\rangle_{\text{skin}} = \frac{1}{N_{\text{skin}}}\sum_i \mu_{i,\text{skin}};$$

$$\langle\mu\rangle_{\text{bcc}} = \frac{1}{N_{\text{bcc}}}\sum_i \mu_{i,\text{bcc}};$$

$$s^2_{\text{skin}} = \frac{1}{N_{\text{skin}}}\sum_i (\mu_{i,\text{skin}} - \langle\mu\rangle_{\text{skin}})^2;$$

$$s^2_{\text{bcc}} = \frac{1}{N_{\text{bcc}}}\sum_i (\mu_{i,\text{bcc}} - \langle\mu\rangle_{\text{bcc}})^2.$$

- The LDA should maximize separation of healthy skin and BCC classes in 1D subspace, and this is equal to maximizing the following criterion

$$F(\mathbf{w}) = \frac{|\langle\mu\rangle_{\text{skin}} - \langle\mu\rangle_{\text{bcc}}|^2}{s^2_{\text{skin}} + s^2_{\text{bcc}}} = \frac{\mathbf{w}^{\text{T}} S_{\text{between}}\mathbf{w}}{\mathbf{w}^{\text{T}} S_{\text{within}}\mathbf{w}}, \quad (4)$$

where

$$S_{\text{between}} = (\langle\mathbf{r}\rangle_{\text{skin}} - \langle\mathbf{r}\rangle_{\text{bcc}})(\langle\mathbf{r}\rangle_{\text{skin}} - \langle\mathbf{r}\rangle_{\text{bcc}})^{\text{T}}$$

and

$$S_{\text{within}} = S_{\text{skin}} + S_{\text{bcc}}$$

are between-class and within-class scatterers, respectively. By maximizing the criterion (4), we obtain the following solution for the projection operator

$$\mathbf{w}^{\text{T}} = \text{argmax}[F(\mathbf{w})] = S^{-1}_{\text{within}}(\langle\mathbf{r}\rangle_{\text{skin}} - \langle\mathbf{r}\rangle_{\text{bcc}}). \quad (5)$$

Thereby, by solving Eq. (5) with the priory-characterize healthy skin and BCC points, we find the projection of the data to 1D Fisher LDA subspace.

- Knowing the mean values and the scatterers for the healthy and abnormal tissues, we set a threshold for the discrimination of these two classes in the LDA space. This threshold divides the space between the mean values $\langle\mu\rangle_{\text{skin}}$, $\langle\mu\rangle_{\text{bcc}}$ into two parts, in direct ratio to the values of scatterers S_{skin}, S_{bcc}.

Figure 3(b) shows an LDA representation of the 1st BCC sample measurements (see Table 1). The observed distributions of the data sets in the LDA space could be well-described by normal (Gaussian) probability density functions. Light blue line in Fig. 3(b) illustrates the value of the LDA threshold, which was determined using the described procedure based on the measurements of all six samples. In Fig. 3(a), equal linear threshold is shown as a light blue 4D plane in the principal component space. This threshold allows for differentiating both ordinary and keratinized BCC from healthy tissues of the skin.

After determining the projection operator $\mathbf{w}^{\text{T}}$ and the threshold value, we could apply the following procedure to discriminate healthy and BCC tissue.

- Detection of the multispectral modulation AF images of the sample $I_\lambda(t, \mathbf{x})$. Demodulation of the AF images (see Eq. (1)) for obtaining the multispectral AF images $f_\lambda(\mathbf{x})$.
- Calculation of the experimental data representation in the principal component space (see Eqs. (2)-(3)) for the entire number of the image pixels.
- Projection of the data from the principal component space to the LDA space using the operator $\mathbf{w}^{\text{T}}$ (see Eq. (5)).
- Differentiation of healthy skin and BCC tissues in the LDA space using the prior defined threshold value.
- Back-projection of the discriminated LDA data onto the initial visual image (clinical photo) of the sample.

In the LDA space (see Fig. 3(b)), both ordinary and keratinized BCC data appear to be shifted in one direction towards healthy skin data. The separation of tissues becomes possible because the LDA of the multi-spectral AF images allows studying spectrally-dependent data on the tissue AF instead of analyzing only the AF intensity.

5 LDA-Based Mapping of the Skin

In order to highlight an ability for discrimination of BCC from healthy skin tissue using the proposed AF imaging approach, we implement equal projection operator $\mathbf{w}^{\text{T}}$ and LDA threshold value for differentiating healthy and cancer tissues of all six BCC samples from Table 1. Figure 4 shows results of the tissue mapping: semi-transparent green masks represent the BCC area, which is estimated via the proposed multispectral AF imaging; red lines show the actual area of lesions. Since all of the imaged BCC samples correspond to the clinically identified type of BCC lesions (i.e. these samples do not contain any subsurface or clinically undetected BCC fragments), in our research, we estimate the actual area of the lesions by combining the visual examination of tissues by medical expert with the further histological study of tissue fragments.

Considering the results of the 1st BCC sample mapping (see Fig. 4(a) and Table 1), we could observe

high efficiency of the proposed technique. For this sample, we correctly identified 96.8% of BCC area and 85.7% of healthy skin area, while the mistakes of BCC and healthy skin identification were 3.2% and 14.3%, respectively. For other BCC samples (panels from (b) to (f) in Fig. 4 corresponding to the BCC samples 2 to 6 in Table 1), we observed lower accuracy of tissue discrimination; Table 2 summarizes an analysis of the proposed technique accuracy, as well as reports averaged values – 76.4 % and 82.5 % of BCC and healthy skin tissues were accurately characterized. The minimal amount of imaged BCC samples is enough to highlight the ability for tissue differentiation using the proposed multispectral modulation AF imaging technique. However, this amount is not enough to perform in-depth statistical analysis of experimental data – i.e. to analyze sensitivity and specificity, type I and type II errors of tissue differentiation.

The accuracy of the tissue mapping could suffer from a number of factors, including laterally-inhomogeneous absorption [4, 82] and anisotropic polarization-dependent scattering [64, 73] of both the UV-radiation and the AF component in tissues. For further increase of imaging efficiency and tissue discrimination accuracy, the listed features of tissue should be taken into account during the analysis of the multispectral AF imaging data [74, 75, 100]. Furthermore, by increasing the number of tissue samples at the stage of algorithm calibration, we could also significantly improve the proposed technique performance.

6 Discussions

The results of this pilot study involving *in vitro* tissue examination allow us to perform preliminary analysis, i.e. to perform feasibility test, which aims to objectively uncover strengths and weaknesses of the proposed AF imaging approach before committing to a full-blown study. Since physical properties of *in vitro* and *in vivo* tissues, including their AF spectra, could differ significantly depending on the time passed between surgery excision and experimental study, obviously, our future work should be dedicated to extensive clinical research focused on *in vivo* measurements. Nothing but the clinical research of *in vivo* samples, which involves the stage of method calibration based on large amount of samples and the stage of extensive statistical analysis of method performance, could form a basis for development of novel techniques for skin cancer diagnosis based on the multispectral modulation AF imaging.

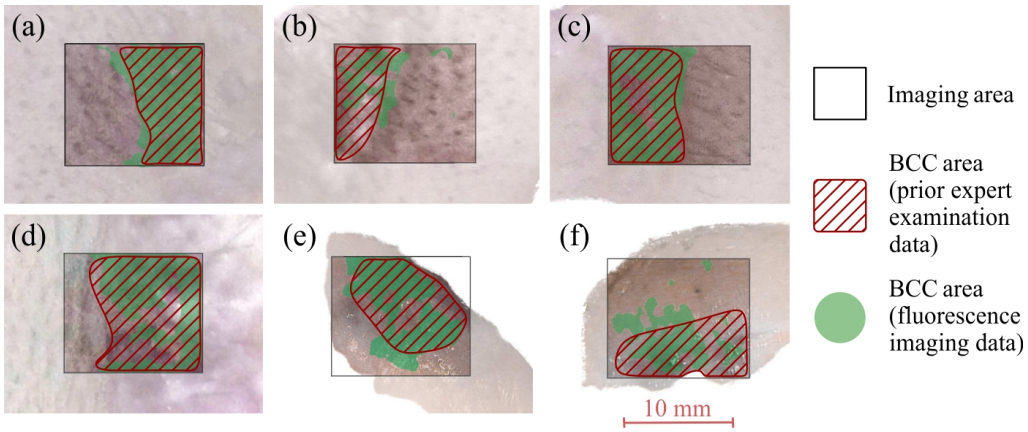


Fig. 4 Mapping healthy and BCC tissue using the multi-spectral AF imaging: semi-transparent green masks represent the BCC area estimated via the proposed approach; red lines show the actual BCC area estimated via the visual examination of tissues by medical expert combined with the further histological study of tissues.

Table 2 Accuracy of healthy and abnormal tissue mapping.

Sample #	1	2	3	4	5	6	Average	SD
Correctly identified BCC tissue, %	96.8	50.7	81.3	71.6	88.2	70.1	76.4	±14.7
Correctly identified healthy skin, %	85.7	79.3	82.7	86.5	84.7	76.1	82.5	±3.7

In our future research, we would also focus on the development of a portable experimental setup with improved operation rate, up to real-time imaging. For this purpose, we would: (i) increase the sensitivity of digital camera; (ii) optimize the UV-radiation parameters – i.e. select the optimal wavelength and increase the excitation power to the maximal permissible value; (iii) optimize a set of the bandpass optical filters for accommodating the spectrum of tissue AF and improving separability of classes of healthy and pathological tissues in the LDA-space; (iv) manage the LDA threshold value to maximize the tissue discrimination accuracy, and (v) use the advance methods of image processing to eliminate an impact of background tissue properties on differentiation accuracy. Other technical improvements, such as (i) substitution of the mercury lamp with UV-diode, (ii) increase of the number of UV-excitation channels to combine the AF imaging with the concept of fluorescent matrix [4], and (iii) improvement of the performance of optical systems in both excitation and imaging branches, can bring the system operation to a much higher level.

From a viewpoint of the spatial resolution and the examined object dimensions, all the existing fluorescence imaging methods can be divided into two classes – the methods of microscopic and macroscopic fluorescence imaging [3]. The microscopic techniques of the fluorescence imaging [84, 101–103] are characterized with very high lateral and depth spatial resolution, as well as advanced sensitivity, which yields visualizing the internal structure of the skin. These methods allow for studying separate cells and analyzing intravascular and interstitial cell processes. An AF microscopy was combined with Raman micro-spectroscopy for diagnosis of tissues and, in particular, for detection of BCC in tissue specimens excised during Mohs micrographic surgery [104, 105]. Despite the tremendous resolution and sensitivity, microscopic fluorescence imaging techniques are characterized with limited field of view and excessive laboriousness, which makes them unreliable for use in a clinical practice.

The macroscopic fluorescence imaging techniques aim distinguishing between different types of tissues and finding their margins in a large fields of view and with a smaller (compared to microscopy) spatial resolution [58, 103, 106]. A modern trend in development of novel instruments for fluorescence diagnosis of the skin is associated with the use of multimodal imaging technologies – i.e combining endogenous and exogenous fluorescence phenomena [107] or combining fluorescence imaging with Raman micro-spectroscopy [108]. Furthermore, approaches of multispectral fluorescence imaging, which combine either several excitation and/or several detection channels with advanced methods of signal processing, are extensively developed during the past decades based on exogenous and endogenous fluorescence phenomena [106, 109–111].

The multispectral AF imaging approach proposed in this paper belongs to the group of the macroscopic fluorescence imaging techniques. Despite its technical simplicity, the proposed method provides relatively high performance, sensitivity and specificity of tissue differentiation compared to the existing methods of macroscopic AF diagnosis of low-pigmented skin malignancies [106, 109, 111]. The developed method allows for distinguishing both ordinary and keratinized BCC lesions from healthy skin thanks to the favorable combination of the narrow-line-width UV-excitation, the four orthogonal channels of image detection and the LDA-based approach for tissue discrimination, which relies on the use of normalized spectral AF intensities. The latter problem cannot be solved by simple analysis of the AF intensity since the AF intensity of ordinary BCC is lower, and the AF intensity of keratinized BCC is higher, compared to healthy skin [58]. The developed method provides discrimination of tissues even in case of simple low-aperture optical elements and standard uncooled CMOS-cameras are employed. This makes the proposed technique rather cheap; thus, more attractive and reliable for practical use in a clinic, when compared to the complex and expensive methods of the AF microscopy [84, 101–103] and the techniques, which combine fluorescence and Raman scattering phenomena [104, 105, 108].

In our opinion, the most promising application of the proposed multispectral AF imaging technique is associated with accomplishing the complete removal of the tumor and maximal preservation of the normal skin [112] by complementing such well-known techniques as Mohs micrographic surgery [113] and micrographic Doppler velocimetry [114], which are widely applied nowadays for removing BCC and SCC of the skin. In Mohs micrographic surgery, microscopic examination of all excised tissues occurs during the surgery, thereby providing tremendous accuracy and eliminating the need to estimate how far laterally or deep the cancer spreads [115]. In case of further increase of the described technique sensitivity, it could be applied in order to limit the amount of the tissue to be examined via microscopy during the cancer removal, and, as a consequence, to reduce the laboriousness and duration of the Mohs surgical procedure. Furthermore, this technique could be generalized for studying other types of biological objects, such as bacteria, or even for applications in pharmaceutical and material sciences, in chemical industry and food inspection.

7 Conclusions

In conclusion, in this paper, we proposed an approach for differentiating BCC and healthy skin, which relies on the use of the multispectral modulation AF imaging combined with the LDA-based processing of the normalized tissue AF intensities in four spectrally-orthogonal imaging channels. We enhanced the signal-to-noise ratio and suppress the non-fluorescent background in the AF images by employing the modulation of the UV-radiation and the Fourier-domain demodulation of the AF visible images. We assembled the experimental setup and applied it for studying the

samples of freshly excised BCC *in vitro*. The observed results demonstrate an ability for distinguishing both ordinary and keratinized BCC from healthy skin justifying the perspectives of the proposed technique use for diagnosis of BCC and other low-pigmented malignancies of the skin.

Disclosures

All authors declare that there is no conflict of interests in this paper.

Acknowledgements

Development of the approach for statistical analysis of the multispectral images, which yields differentiating healthy and pathological tissues, was supported by the grant of the Russian Foundation for Basic Research, Project #18-29-02060. The authors are thankful to Prof. Larisa P. Safonova for fruitful discussions.

References

1. G. A. Wagnieres, W. M. Star, and B. C. Wilson, "In vivo fluorescence spectroscopy and imaging for oncological applications," Photochemistry and Photobiology 68(5), 603–632 (1998).
2. S. Andersson-Engels, C. af Klinteberg, K. Svanberg, and S. Svanberg, "In vivo fluorescence imaging for tissue diagnostics," Physics in Medicine & Biology 42(5), 815–824 (1997).
3. R. Weissleder, M. J. Pittet, "Imaging in the era of molecular oncology," Nature 452(7187), 580–589 (2008).
4. E. G. Borisova, L. P. Angelova, and E. P. Pavlova, "Endogenous and exogenous fluorescence skin cancer diagnostics for clinical applications," IEEE Journal of Selected Topics in Quantum Electronics 20(2), 211–222 (2014).
5. I. Munro, J. McGinty, N. Galletly, J. Requejo-Isidro, P. M. P. Lanigan, D. S. Elson, C. Dunsby, M. A. A. Neil, M. J. Lever, G. W. H. Stamp, and P. M. W. French, "Toward the clinical application of time-domain fluorescence lifetime imaging," Journal of Biomedical Optics 10(5), 51403 (2005).
6. S. Shrestha, B. E. Applegate, J. Park, X. Xiao, P. Pande, and J. A. Jo, "High-speed multispectral fluorescence lifetime imaging implementation for in vivo applications," Optics Letters 35(15), 2558–2560 (2010).
7. F. Fereidouni, K. Reitsma, and H. C. Gerritsen, "High speed multispectral fluorescence lifetime imaging," Optics Express 21(10), 11769–11782 (2013).
8. O. Gutierrez-Navarro, D. U. Campos-Delgado, E. Arce-Santana, M. O. Mendez, and J. A. Jo, "A fully constrained optimization method for time-resolved multispectral fluorescence lifetime imaging microscopy data unmixing," IEEE Transactions on Biomedical Engineering 60(6), 1711–1720 (2013).
9. J. Bec, D. M. Ma, D. R. Yankelevich, J. Liu, W. T. Ferrier, J. Southard, and L. Marcu, "Multispectral fluorescence lifetime imaging system for intravascular diagnostics with ultrasound guidance: In vivo validation in swine arteries," Journal of Biophotonics 7(5), 281–285 (2014).
10. S. Cheng, R. M. Cuenca, B. Liu, B. H. Malik, J. M. Jabbour, K. C. Maitland, J. Wright, Y.-S. L. Cheng, and J. A. Jo, "Handheld multispectral fluorescence lifetime imaging system for in vivo applications," Biomedical Optics Express 5(3), 921–931 (2014).
11. E. L. Elson, D. Magde, "Fluorescence correlation spectroscopy. I. Conceptual basis and theory," Biopolymers 13(1), 1–27 (1974).
12. D. Magde, E. L. Elson, and W. W. Webb, "Fluorescence correlation spectroscopy. II. An experimental realization," Biopolymers 13(1), 29–61 (1974).
13. W. Denk, J. H. Strickler, and W. W. Webb, "Two-photon laser scanning fluorescence microscopy," Science 248(4951), 73–76 (1990).
14. K. M. Berland, P. T. C. So, and E. Gratton, "Two-photon fluorescence correlation spectroscopy: Method and application to the intracellular environment," Biophysical Journal 68(2), 694–701 (1995).
15. G. Tarrach, M. A. Bopp, D. Zeisel, and A. J. Meixner, "Design and construction of a versatile scanning near-field optical microscope for fluorescence imaging of single molecules," Review of Scientific Instruments 66(6), 3569–3575 (1995).
16. L. M. Miller, P. Dumas, N. Jamin, J.-L. Teillaud, J. Miklossy, and L. Forro, "Combining IR spectroscopy with fluorescence imaging in a single microscope: Biomedical applications using a synchrotron infrared source (invited)," Review of Scientific Instruments 73(3), 1357–1360 (2002).
17. H. Muramatsu, J. M. Kim, S. Sugiyama, and T. Ohtani, "Simultaneous multicolor fluorescence imaging by scanning near-field optical/atomic force microscopy," Review of Scientific Instruments 74(1), 100–103 (2003).
18. I. M. Vellekoop, C. M. Aegerter, "Scattered light fluorescence microscopy: Imaging through turbid layers," Optics Letters 35(8), 1245–1247 (2010).
19. J. W. Hastings, "Chemistries and colors of bioluminescent reactions: A review," Gene 173(1), 5–11 (1996).

20. K. Nikolova, M. Zlatanov, T. Eftimov, D. Brabant, S. Yosifova, E. Halil, G. Antova, and M. Angelova, "Fluoresence spectra from vegetable oils using violet and blue LD/LED exitation and an optical fiber spectrometer," International Journal of Food Properties 17(6), 1211–1223 (2014).
21. E. V. Demidova, T. N. Goryachkovskaya, I. A. Mescheryakova, T. K. Malup, A. I. Semenov, N. A. Vinokurov, N. A. Kolchanov, V. M. Popik, and S. E. Peltek, "Impact of terahertz radiation on stress-sensitive genes of E.Coli cell," IEEE Transactions on Terahertz Science and Technology 6(3), 435–441 (2016).
22. H. J. C. M. Sterenborg, M. Motamedi, R. F. Wagner, M. Duvic, S. Thomsen, and S. L. Jacques, "In vivo fluorescence spectroscopy and imaging of human skin tumours," Lasers in Medical Science 9(3), 191–201 (1994).
23. A. N. Bashkatov, E. A. Genina, V. I. Kochubey, and V. V. Tuchin, "Optical properties of human skin, subcutaneous and mucous tissues in the wavelength range from 400 to 2000 nm," Journal of Physics D: Applied Physics 38(15), 2543–2555 (2005).
24. K. T. Schomacker, J. K. Frisoli, C. C. Compton, T. J. Flotte, J. M. Richter, N. S. Nishioka, and T. F. Deutsch, "Ultraviolet laser-induced fluorescence of colonic tissue: Basic biology and diagnostic potential," Lasers in Medical Science 12(1), 63–78 (1992).
25. R. M. Cothren, M. V Sivak, J. Van Dam, R. E. Petras, M. Fitzmaurice, J. M. Crawford, J. Wu, J. F. Brennan, R. P. Rava, R. Manoharan, and M. S. Feld, "Detection of dysplasia at colonoscopy using laser-induced fluorescence: a blinded study," Gastrointestinal Endoscopy 44(2), 168–176 (2009).
26. T. E. Renkoski, B. Banerjee, L. R. Graves, N. S. Rial, S. A. H. Reid, V. L. Tsikitis, V. N. Nfonsam, P. Tiwari, H. Gavini, and U. Utzinger, "Ratio images and ultraviolet C excitation in autofluorescence imaging of neoplasms of the human colon," Journal of Biomedical Optics 18(1), 16005 (2013).
27. I. Georgakoudi, B. C. Jacobson, J. Van Dam, V. Backman, M. B. Wallace, M. G. Müller, Q. Zhang, K. Badizadegan, D. Sun, G. A. Thomas, L. T. Perelman, and M. S. Feld, "Fluorescence, reflectance, and light-scattering spectroscopy for evaluating dysplasia in patients with Barrett's esophagus," Gastroenterology 120(7), 1620–1629 (2001).
28. T. J. Pfefer, D. Y. Paithankar, J. M. Poneros, K. T. Schomacker, and N. S. Nishioka, "Temporally and spectrally resolved fluorescence spectroscopy for the detection of high grade dysplasia in Barrett's esophagus," Lasers in Surgery and Medicine 32(1), 10–16 (2003).
29. M. Kara, R. S. DaCosta, B. C. Wilson, N. E. Marcon, and J. Bergman, "Autofluorescence-based detection of early neoplasia in patients with Barrett's esophagus," Digestive Diseases 22(2), 134–141 (2004).
30. M. Tatsuta, H. Iishi, M. Ichii, M. Baba, R. Yamamoto, S. Okuda, and K. Kikuchi, "Diagnosis of gastric cancers with fluorescein-labeled monoclonal antibodies to carcinoembryonic antigen," Lasers in Surgery and Medicine 9(4), 422–426 (1989).
31. V. G. Peters, D. R. Wyman, M. S. Patterson, and G. L. Frank, "Optical properties of normal and diseased human breast tissues in the visible and near infrared," Physics in Medicine & Biology 35(9), 1317–1334 (1990).
32. S. D. Kamath, R. A. Bhat, S. Ray, and K. K. Mahato, "Autofluorescence of normal, benign, and malignant ovarian tissues: A pilot study," Photomedicine and Laser Surgery 27(2), 325–335 (2009).
33. T. E. Renkoski, K. D. Hatch, and U. Utzinger, "Wide-field spectral imaging of human ovary autofluorescence and oncologic diagnosis via previously collected probe data," Journal of Biomedical Optics 17(3), 36003 (2012).
34. R. George, M. Michaelides, M. A. Brewer, and U. Utzinger, "Parallel factor analysis of ovarian autofluorescence as a cancer diagnostic," Lasers in Surgery and Medicine 44(4), 282–295 (2012).
35. A. A. Potapov, S. A. Goryaynov, V. A. Okhlopkov, L. V. Shishkina, V. B. Loschenov, T. A. Savelieva, D. A. Golbin, A. P. Chumakova, M. F. Goldberg, M. D. Varyukhina, and A. Spallone, "Laser biospectroscopy and 5-ALA fluorescence navigation as a helpful tool in the meningioma resection," Neurosurgical Review 39(3), 437–447 (2016).
36. I. A. Shikunova, D. O. Stryukov, S. N. Rossolenko, A. M. Kiselev, and V. N. Kurlov, "Neurosurgery contact handheld probe based on sapphire shaped crystal," Journal of Crystal Growth 457, 265–269 (2017).
37. I. A. Shikunova, G. M. Katyba, K. I. Zaytsev, I. N. Dolganova, I. A. Shikunova, N. V. Chernomyrdin, S. O. Yurchenko, G. A. Komandin, I. V. Reshetov, V. V. Nesvizhevsky, and V. N. Kurlov, "Sapphire shaped crystals for waveguiding, sensing, and exposure applications," Progress in Crystal Growth and Characterization of Materials (2018).
38. M. Monici, "Cell and tissue autofluorescence research and diagnostic applications," Biotechnology Annual Review 11, 227–256 (2005).
39. F. Fischer, E. F. Dickson, J. C. Kennedy, and R. H. Pottier, "An affordable, portable fluorescence imaging device for skin lesion detection using a dual wavelength approach for image contrast enhancement and aminolaevulinic acid-induced protoporphyrin IX. Part II. In vivo testing," Lasers in Medical Science 16(3), 207–212 (2001).
40. B. Zhao, Y.-Y. He, "Recent advances in the prevention and treatment of skin cancer using photodynamic therapy," Expert Review of Anticancer Therapy 10(11), 1797–1809 (2010).
41. G. Terentyuk, E. Panfilova, V. Khanadeev, D. Chumakov, E. Genina, A. Bashkatov, V. Tuchin, A. Bucharskaya, G. Maslyakova, N. Khlebtsov, and B. Khlebtsov, "Gold nanorods with a hematoporphyrin-loaded silica shell for dual-modality photodynamic and photothermal treatment of tumors in vivo," Nano Research 7(3), 325–337 (2014).

42. B. Khlebtsov, E. Tuchina, V. Tuchin, and N. Khlebtsov, "Multifunctional Au nanoclusters for targeted bioimaging and enhanced photodynamic inactivation of Staphylococcus aureus," RSC Advances 5(76), 61639–61649 (2015).
43. V. P. Zharov, E. I. Galanzha, E. V. Shashkov, N. G. Khlebtsov, and V. V. Tuchin., "In vivo photoacoustic flow cytometry for monitoring of circulating single cancer cells and contrast agents," Optics Letters 31(24), 3623 (2006).
44. J.-W. Kim, E. I. Galanzha, E. V. Shashkov, H.-M. Moon, and V. P. Zharov, "Golden carbon nanotubes as multimodal photoacoustic and photothermal high-contrast molecular agents," Nature Nanotechnology 4(10), 688–694 (2009).
45. J. T. Alander, I. Kaartinen, A. Laakso, T. Pätilä, T. Spillmann, V. V. Tuchin, M. Venermo, and P. Välisuo, "A Review of indocyanine green fluorescent imaging in surgery," International Journal of Biomedical Imaging 2012, 940585 (2012).
46. E. I. Galanzha, R. Weingold, D. A. Nedosekin, M. Sarimollaoglu, J. Nolan, W. Harrington, A. S. Kuchyanov, R. G. Parkhomenko, F. Watanabe, Z. Nima, A. S. Biris, A. I. Plekhanov, M. I. Stockman, and V. P. Zharov, "Spaser as a biological probe," Nature Communications 8, 15528 (2017).
47. K. I. Zaytsev, K. G. Kudrin, V. E. Karasik, I. V. Reshetov, and S. O. Yurchenko, "In vivo terahertz spectroscopy of pigmentary skin nevi: Pilot study of non-invasive early diagnosis of dysplasia," Applied Physics Letters 106(5), 053702 (2015).
48. S. Andersson-Engels, R. Berg, K. Svanberg, and S. Svanberg, "Multi-colour fluorescence imaging in connection with photodynamic therapy of delta-amino levulinic acid (ALA) sensitised skin malignancies," Bioimaging 3(3), 134–143 (1995).
49. G. E. Pierard, C. Pierard-Franchimont, L. Dewalque, C. Charlier, T. Hermanns-Le, S. Pierard, and P. Delvenne, "In vivo skin fluorescence imaging in young Caucasian adults with early malignant melanomas," Clinical, Cosmetic and Investigational Dermatology 7, 225–230 (2014).
50. C. S. Joseph, R. Patel, V. A. Neel, R. H. Giles, and A. N. Yaroslavsky, "Imaging of ex vivo nonmelanoma skin cancers in the optical and terahertz spectral regions optical and terahertz skin cancers imaging," Journal of Biophotonics 7(5), 295–303 (2014).
51. R. Cubeddu, A. Pifferi, P. Taroni, A. Torricelli, G. Valentini, and E. Sorbellini, "Fluorescence lifetime imaging: an application to the detection of skin tumors," IEEE Journal of Selected Topics in Quantum Electronics 5(4), 923–929 (1999).
52. A. M. Wennberg, F. Gudmundson, B. Stenquist, A. Ternesten, L. Mölne, A. Rosén, and O. Larkö, "In vivo detection of basal cell carcinoma using imaging spectroscopy," Acta Dermato-Venereologica 79(1), 54–61 (1999).
53. R. Na, I. M. Stender, and H. C. Wulf, "Can autofluorescence demarcate basal cell carcinoma from normal skin? A comparison with protoporphyrin IX fluorescence," Acta Dermato-Venereologica 81(4), 246–249 (2001).
54. A. N. Yaroslavsky, V. Neel, and R. R. Anderson, "Fluorescence polarization imaging for delineating nonmelanoma skin cancers," Optics Letters 29(17), 2010–2012 (2004).
55. R. Cicchi, D. Massi, S. Sestini, P. Carli, V. De Giorgi, T. Lotti, and F. S. Pavone, "Multidimensional non-linear laser imaging of Basal Cell Carcinoma," Optics Express 15(16), 10135–10148 (2007).
56. I. Kopriva, A. Peršin, H. Zorc, A. Pašić, J. Lipozenčić, K. Kostović, and M. Lončarić, "Visualization of basal cell carcinoma by fluorescence diagnosis and independent component analysis," Photodiagnosis and Photodynamic Therapy 4(3), 190–196 (2007).
57. T. Gambichler, G. Moussa, and P. Altmeyer, "A pilot study of fluorescence diagnosis of basal cell carcinoma using a digital flash light-based imaging system," Photodermatology, Photoimmunology & Photomedicine 24(2), 67–71 (2008).
58. N. P. Galletly, J. McGinty, C. Dunsby, F. Teixeira, J. Requejo-Isidro, I. Munro, D. S. Elson, M. A. A. Neil, A. C. Chu, P. M. W. French, and G. W. Stamp, "Fluorescence lifetime imaging distinguishes basal cell carcinoma from surrounding uninvolved skin," British Journal of Dermatology 159(1), 152–161 (2008).
59. K. I. Zaytsev, A. V. Perchik, N. V. Chernomyrdin, K. G. Kudrin, I. V. Reshetov, and S. O. Yurchenko, "Hyper-spectral modulation fluorescent imaging using double acousto-optical tunable filter based on TeO2 - crystals," Journal of Physics: Conference Series 584(1), 012017 (2015).
60. N. V. Chernomyrdin, K. I. Zaytsev, A. D. Lesnichaya, K. G. Kudrin, O. P. Cherkasova, V. N. Kurlov, I. A. Shikunova, A. V. Perchik, S. O. Yurchenko, and I. V. Reshetov, "Principle component analysis and linear discriminant analysis of multi-spectral autofluorescence imaging data for differentiating basal cell carcinoma and healthy skin," Proceeding of SPIE 9976, 99760B (2016).
61. G. Ziegelberger, "ICNIRP guidelines on limits of exposure to laser radiation of wavelengths between 180 nm and 1,000 um," Health Physics 105(3), 271–295 (2013).
62. V. V. Tuchin, Tissue Optics: Light Scattering Methods and Instruments for Medical Diagnostics, 3rd ed., SPIE Press, Bellingham, USA (2015).
63. S. Holopainen, F. Manoocheri, and E. Ikonen, "Non-Lambertian behaviour of fluorescence emission from solid amorphous material," Metrologia 46(4), 197 (2009).

64. M. Keijzer, R. R. Richards-Kortum, S. L. Jacques, and M. S. Feld, "Fluorescence spectroscopy of turbid media: Autofluorescence of the human aorta," Applied Optics 28(20), 4286 (1989).
65. J. Wu, F. Partovi, M. S. Field, and R. P. Rava, "Diffuse reflectance from turbid media: an analytical model of photon migration," Applied Optics 32(7), 1115 (1993).
66. A. J. Durkin, S. Jaikumar, N. Ramanujam, and R. Richards-Kortum, "Relation between fluorescence spectra of dilute and turbid samples," Applied Optics 33(3), 414 (1994).
67. M. A. O'Leary, D. A. Boas, X. D. Li, B. Chance, and A. G. Yodh, "Fluorescence lifetime imaging in turbid media," Optics Letters 21(2), 158 (1996).
68. B. B. Das, F. Liu, and R. R. Alfano, "Time-resolved fluorescence and photon migration studies in biomedical and model random media," Reports on Progress in Physics 60(2), 227–292 (1997).
69. S. C. Gebhart, A. Mahadevan-Jansen, and W.-C. Lin, "Experimental and simulated angular profiles of fluorescence and diffuse reflectance emission from turbid media," Applied Optics 44(23), 4884 (2005).
70. L. G. Coppel, N. Johansson, and M. Neuman, "Angular dependence of fluorescence from turbid media," Optics Express 23(15), 19552 (2015).
71. J. Wu, M. S. Feld, and R. P. Rava, "Analytical model for extracting intrinsic fluorescence in turbid media," Applied Optics 32(19), 3585 (1993).
72. C. M. Gardner, S. L. Jacques, and A. J. Welch, "Fluorescence spectroscopy of tissue: recovery of intrinsic fluorescence from measured fluorescence," Applied Optics 35(10), 1780 (1996).
73. J. Y. Qu, Z. Huang, and J. Hua, "Excitation-and-collection geometry insensitive fluorescence imaging of tissue-simulating turbid media," Applied Optics 39(19), 3344 (2000).
74. Q. Zhang, M. G. Müller, J. Wu, and M. S. Feld, "Turbidity-free fluorescence spectroscopy of biological tissue," Optics Letters 25(19), 1451 (2000).
75. M. G. Müller, I. Georgakoudi, Q. Zhang, J. Wu, and M. S. Feld, "Intrinsic fluorescence spectroscopy in turbid media: disentangling effects of scattering and absorption," Applied Optics 40(25), 4633 (2001).
76. K. Koyama, M. Yoshita, M. Baba, T. Suemoto, and H. Akiyama, "High collection efficiency in fluorescence microscopy with a solid immersion lens," Applied Physics Letters 75(12), 1667–1669 (1999).
77. C. A. Combs, A. Smirnov, D. Chess, D. B. Mcgavern, J. L. Schroeder, J. Riley, S. S. Kang, M. Lugar-Hammer, A. Gandjbakhche, J. R. Knutson, and R. S. Balaban, "Optimizing multiphoton fluorescence microscopy light collection from living tissue by noncontact total emission detection (epiTED)," Journal of Microscopy 241(2), 153–161 (2011).
78. J. P. Zinter, M. J. Levene, "Maximizing fluorescence collection efficiency in multiphoton microscopy," Optics Express 19(16), 15348 (2011).
79. T. Ruckstuhl, D. Verdes, "Supercritical angle fluorescence (SAF) microscopy," Optics Express 12(18), 4246 (2004).
80. J. J. Fisz, "Fluorescence polarization spectroscopy at combined high-aperture excitation and detection: Application to one-photon-excitation fluorescence microscopy," The Journal of Physical Chemistry A 111(35), 8606–8621 (2007).
81. J. J. Fisz, "Another treatment of fluorescence polarization microspectroscopy and imaging," The Journal of Physical Chemistry A 113(15), 3505–3516 (2009).
82. A. Curtis, K. Calabro, J.-R. Galarneau, I. J. Bigio, and T. Krucker, "Temporal Variations of Skin Pigmentation in C57Bl/6 Mice Affect Optical Bioluminescence Quantitation," Molecular Imaging and Biology 13(6), 1114–1123 (2011).
83. J. R. Lakowicz (ed), Principles of Fluorescence Spectroscopy, Springer, Boston, MA, USA (2006).
84. E. Drakaki, C. Dessinioti, A. J. Stratigos, C. Salavastru, and C. Antoniou, "Laser-induced fluorescence made simple: implications for the diagnosis and follow-up monitoring of basal cell carcinoma," Journal of Biomedical Optics 19(3), 30901 (2014).
85. E. Mitrani, R. Marks, "Procollagen localisation in normal, premalignant and malignant lesions of the epidermis," Archives of Dermatological Research 274(1), 21–28 (1982).
86. J. C. Zhang, H. E. Savage, P. G. Sacks, T. Delohery, R. R. Alfano, A. Katz, and S. P. Schantz, "Innate cellular fluorescence reflects alterations in cellular proliferation," Lasers in Surgery and Medicine 20(3), 319–331 (1997).
87. W. Lohmann, M. Nilles, and R. H. Bodeker, "In situ differentiation between nevi and malignant melanomas by fluorescence measurements," Naturwissenschaften 78(10), 456–457 (1991).
88. N. Ramanujam, M. F. Mitchell, A. Mahadevan, S. Warren, S. Thomsen, E. Silva, and R. Richards-Kortum, "In vivo diagnosis of cervical intraepithelial neoplasia using 337-nm-excited laser-induced fluorescence," Proceedings of the National Academy of Sciences 91(21), 10193–10197 (1994).
89. F. Koenig, F. J. McGovern, A. F. Althausen, T. F. Deutsch, and K. T. Schomacker, "Laser induced autofluorescence diagnosis of bladder cancer," Journal of Urology 156(5), 1597–1601 (1996).
90. M. Zellweger, D. Goujon, R. Conde, M. Forrer, H. van den Bergh, and G. Wagnières, "Absolute autofluorescence spectra of human healthy, metaplastic, and early cancerous bronchial tissue in vivo," Applied Optics 40(22), 3784–3791 (2001).

91. E. Borisova, P. Troyanova, P. Pavlova, and L. Avramov, "Diagnostics of pigmented skin tumors based on laser-induced autofluorescence and diffuse reflectance spectroscopy," Quantum Electronics 38(6), 597 (2008).
92. Q. Liu, "Role of optical spectroscopy using endogenous contrasts in clinical cancer diagnosis," World Journal of Clinical Oncology 2(1), 50–63 (2011).
93. G. McLachlan, Discriminant Analysis and Statistical Pattern Recognition, Wiley, New York, USA (2004).
94. R. R. Anderson, J. A. Parrish, "The optics of human skin," Journal of Investigative Dermatology 77(1), 13–19 (1981).
95. Z. Volynskaya, A. S. Haka, K. L. Bechtel, M. Fitzmaurice, R. Shenk, N. Wang, J. Nazemi, R. R. Dasari, and M. S. Feld, "Diagnosing breast cancer using diffuse reflectance spectroscopy and intrinsic fluorescence spectroscopy," Journal of Biomedical Optics 13(2), 24012 (2008).
96. I. Bliznakova, E. Borisova, and L. Avramov, "Laser- and Light-Induced Autofluorescence Spectroscopy of Human Skin in Dependence on Excitation Wavelengths," Acta Physica Polonica A 112(5), 1131–1136 (2007).
97. E. Borisova, P. Pavlova, E. Pavlova, P. Troyanova, and L. Avramov, "Optical biopsy of human skin - A tool for cutaneous tumours' diagnosis," International Journal Bioautomation 16(1), 53–72 (2012).
98. R. Richards-Kortum, R. P. Rava, R. E. Petras, M. Fitzmaurice, M. Sivak, and M. S. Feld, "Spectroscopic diagnosis of colonic dysplasia," Photochemistry and Photobiology 53(6), 777–786 (1991).
99. R. A. Fischer, "The use of multiple measurements in taxonomic problems," Annals of Eugenics 7(2), 179–188 (1936).
100. R. Na, I.-M. Stender, M. Henriksen, and H. C. Wulf., "Autofluorescence of human skin is age-related after correction for skin pigmentation and redness," Journal of Investigative Dermatology 116(4), 536–540 (2001).
101. J. Paoli, M. Smedh, A.-M. Wennberg, and M. B. Ericson, "Multiphoton laser scanning microscopy on non-melanoma skin cancer: morphologic features for future non-invasive diagnostics," Journal of Investigative Dermatology 128(5), 1248–1255 (2008).
102. R. Patalay, C. Talbot, Y. Alexandrov, I. Munro, M. A. A. Neil, K. König, P. M. W. French, A. Chu, G. W. Stamp, and C. Dunsby, "Quantification of cellular autofluorescence of human skin using multiphoton tomography and fluorescence lifetime imaging in two spectral detection channels," Biomedical Optics Express 2(12), 3295 (2011).
103. D. Göppner, N. Mechow, J. Liebscher, E. Thiel, G. Seewald, H. Gollnick, C. M. Philipp, and K.-H. Schönborn, "Wide-field, high-resolution two-photon tissue mapping of human skin ex vivo," Medical Laser Application 26(4), 158–165 (2011).
104. K. Kong, C. J. Rowlands, S. Varma, W. Perkins, I. H. Leach, A. A. Koloydenko, H. C. Williams, and I. Notingher, "Diagnosis of tumors during tissue-conserving surgery with integrated autofluorescence and Raman scattering microscopy," Proceedings of the National Academy of Sciences 110(38), 15189–15194 (2013).
105. S. Takamori, K. Kong, S. Varma, I. Leach, H. C. Williams, and I. Notingher, "Optimization of multimodal spectral imaging for assessment of resection margins during Mohs micrographic surgery for basal cell carcinoma," Biomedical Optics Express 6(1), 98 (2015).
106. A. Lihachev, A. Derjabo, I. Ferulova, M. Lange, I. Lihacova, and J. Spigulis, "Autofluorescence imaging of basal cell carcinoma by smartphone RGB camera," Journal of Biomedical Optics 20(12), 120502 (2015).
107. M. B. Ericson, C. Berndtsson, B. Stenquist, A.-M. Wennberg, O. Larko, and A. Rosen, "Multispectral fluorescence imaging of basal cell carcinoma assisted by image warping," Proceeding of SPIE 5141, 114–121 (2003).
108. F. Sinjab, K. Kong, G. Gibson, S. Varma, H. Williams, M. Padgett, and I. Notingher, "Tissue diagnosis using power-sharing multifocal Raman micro-spectroscopy and auto-fluorescence imaging," Biomedical Optics Express 7(8), 2993 (2016).
109. B. Stenquist, M. B. Ericson, C. Strandeberg, L. Molne, A. Rosen, O. Larko, and A. M. Wennberg, "Bispectral fluorescence imaging of aggressive basal cell carcinoma combined with histopathological mapping: a preliminary study indicating a possible adjunct to Mohs micrographic surgery," British Journal of Dermatology 154(2), 305–309 (2006).
110. F. Fischer, E. F. Gudgin Dickson, and R. H. Pottier, "In vivo fluorescence imaging using two excitation and/or emission wavelengths for image contrast enhancement," Vibrational Spectroscopy 30(2), 131–137 (2002).
111. M. B. Ericson, J. Uhre, C. Strandeberg, B. Stenquist, O. Larkö, A.-M. Wennberg, and A. Rosén, "Bispectral fluorescence imaging combined with texture analysis and linear discrimination for correlation with histopathologic extent of basal cell carcinoma," Journal of Biomedical Optics 10(3), 034009 (2005).
112. N. Zhu, C.-Y. Huang, S. Mondal, S. Gao, C. Huang, V. Gruev, S. Achilefu, and R. Liang, "Compact wearable dual-mode imaging system for real-time fluorescence image-guided surgery," Journal of Biomedical Optics 20(9), 96010 (2015).
113. R. Chuong, "Mohs surgery. Techniques, indications, applications, and the future," Journal of Oral and Maxillofacial Surgery 42(4), 274 (1984).
114. R. S. Kirsner, M. Haiken, and L. D. Garland, "Margin assessment of selected basal cell carcinomas utilizing laser doppler velocimetry," International Journal of Dermatology 32(4), 290–292 (1993).
115. G. R. Mikhail, Mohs Micrographic Surgery, W.B. Saunders, Philadelphia, PA, USA (1991).

Laser photoacoustic spectroscopy applications in breathomics

Yury V. Kistenev[1,2*], Alexey V. Borisov[1,2], Victor V. Nikolaev[1,3], Denis A. Vrazhnov[1,3], and Dmytry A.Kuzmin[2]

[1] Tomsk State University, Tomsk 634050, Russia

[2] Siberian State Medical University, Tomsk 634050, Russia

[3] Institute of Strength Physics and Materials Science of Siberian Branch of the RAS, Tomsk 634055, Russia

*** e-mail:** yv.kistenev@gmail.com

Abstract. The breathomics approach to express-diagnosis of bronchopulmonary diseases based on spectral analysis of volatile organic compounds in a patient's exhaled air is discussed. The basic demands and possible technical solutions to laser photoacoustic spectroscopy equipment in a framework of breathomics are presented. An example of differential diagnostics of the set of bronchopulmonary diseases, including lung cancer (LC) patients (N = 9); patients with chronic obstructive pulmonary disease (COPD) (N = 12); patients with pneumonia (N = 11) and a control group of healthy volunteers using breath air analysis by laser photoacoustic spectroscopy and machine learning is presented. © 2019 Journal of Biomedical Photonics & Engineering.

Keywords: Breathomics; exhaled air analysis; laser photoacoustic spectroscopy; optical parametric oscillator; machine learning; lung cancer.

Paper #3307 received 25 Nov 2018; accepted for publication 20 Mar 2019; published online 28 Mar 2019. doi: 10.18287/JBPE19.05.010303.

1 Introduction

Control of metabolites in exhaled air produced by biochemical reactions in cells and organs being called as "breathomics" provides ability of express and noninvasive medical screening. Typical metabolites, produced by pathological processes in the body, include:

— inorganic substances, e.g., carbon dioxide, oxygen, and nitric oxide;

— non-volatile substances, e.g., isoprostanes, cytokines, leukotrienes and hydrogen peroxide;

— volatile organic compounds (VOCs), which include saturated hydrocarbons (ethane, pentane, aldehydes), unsaturated hydrocarbons (isoprene), oxygen containing (acetone), sulphur containing (ethyl mercaptane, dimethylsulfide) and nitrogen containing (dimethylamine, ammonia) [1].

In spite of gas chromatography is a "gold standard" for content analysis of biological origin gas mixtures, this method is quite complicated for routine medicine use.

A set of electrochemical sensors, each of which corresponds to a particular substance (called by "electronic nose" or "e-nose") is one of instrumental methods of exhaled air VOCs control, being suitable for routine measurements. For example "Cyranose 320" includes 32 polymer chemiresistors [2]. The main disadvantages of contact sensors are low selectivity and fast degradation due to surface contamination.

IR laser absorption spectroscopy (LAS) has high sensitivity of molecular species control on the level of ppb and below, as they frequently occur in environmental, medical or biological applications [3]. Most sensitive detection provides photoacoustic spectroscopy, Faraday modulation spectroscopy, cavity ring-down spectroscopy (CRDS) or cavity leak-out spectroscopy (CALOS) which is a CW version of CRDS [3].

Faraday modulation spectroscopy is suitable only for detection of paramagnetic species in gas phase. A significant limitation of the CRDS is technical complexity of wavelength tuning, because this method is based on using of a resonator with high reflected mirrors, but a high reflection is achieved only in a narrow spectral range [4].

Laser photoacoustic spectroscopy (LPAS) is based on registration of pressure wave which is generated in

an analyzed gas sample due to absorption of amplitude modulated laser beam tuned on a frequency of resonant absorption of a specific substance of the sample. Some examples of breathomics LPAS applications are presented below.

In lipid peroxidation, reactive oxygen species react with polyunsaturated fatty acids to form a variety of products, including pentane, ethane, and ethylene (ET). ET concentration was monitored in real time by using a LPAS gas analyzer [5]. The gas analyzer consists of a line-tunable CO_2 laser and a photoacoustic detector (PAD). A sodalime and a KOH scrubbers were used to remove CO_2 from the air sample. A $CaCl_2$ scrubber was used to decrease the water content. Volatile gases were removed using a liquid nitrogen-cooled cryogenic trap (125 K). The CO_2 laser lines 10P(14) ($\lambda = 948.48$ cm^{-1}) and 10P(12) ($\lambda = 951.19$ cm^{-1}) were used for ET concentration measurement. This system has ET detection limit of 6 ppt.

The levels of ET and ammonia in exhaled breath samples (EBS) from patients with cancer and renal failure were measured at sub ppb concentration sensitivities using CO_2 LPAS analyzer [6]. The ET concentration was measured on 10P(14) CO_2 laser line, where the ET absorption coefficient is maximal (30.4 cm^{-1}atm^{-1}), the ammonia concentration was measured on 9R(30) CO_2 laser line, where the ammonia absorption coefficient is 57 cm^{-1}atm^{-1}.

LPAS sensitivity can be improved using PAD intracavity placement [7]. The C_2H_4 detection limit by CO_2 laser intracavity PAD cell in purified from other hydrocarbons ambient air was about 6 ppt [8, 9].

The sensitivity of LPAS can be essentially increased, when the laser beam is modulated by a resonance frequency of the photoacoustic cell. It this case the generated photoacoustic signal is amplified by the quality factor (Q-factor) of the acoustic resonance, which can be achieved up to several hundred [10].

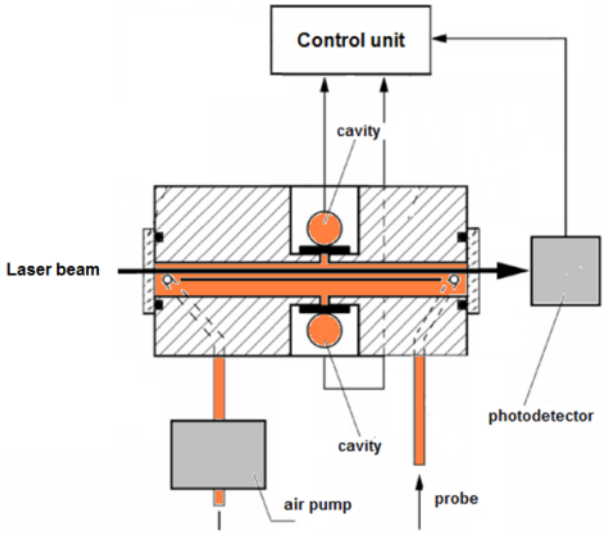
The most frequently used types of resonant LPAS detectors are based on Helmholtz resonators, one-dimensional cylindrical resonators and cavity resonators [11, 12]. The example of construction and sensitivity curve of PAD with two Helmholtz resonators is presented in the Fig. 1 [13].

LPAS gas analyzer with tunable CO_2 laser and intracavity PAD with two Helmholtz resonators was used to measure the spectral characteristics of EAS of the following groups of patients [7]: healthy participants (control group), patients with a bronchopulmonary disease (chronic obstructive pulmonary disease (COPD), asthma, pneumonia), patients with a nonbronchopulmonary disease (coronary heart disease, gastric ulcer, duodenal ulcer), patients with tuberculosis. In total, the quantity of participants was about 200.

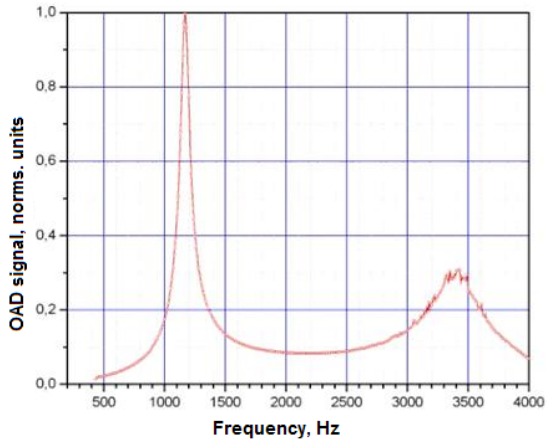
The comparison of measured absorption spectra of EBS for a group under study S was carried out in terms of Mahalanobis distance relatively to the reference group S_0. Let mark measured set of absorption coefficients of the EBS spectra for a group under study S as $\overrightarrow{y_j}, j = \overline{1, N_S}$ and the same values for the reference group as $\overrightarrow{x_i}, i = \overline{1, N_{S_0}}$, correspondently. Here, sets $\vec{x}_j, \vec{y}_j$ can be considered as feature vectors of the state, N_S and N_{S_0} are the total quantity of measured spectra of EAS in the every group. So, the average square of the Mahalanobis distance (ASMD) can be defined as

$$ASMD(\vec{y}_j) = \frac{1}{2mN_{S_0}} \sum_{i=1}^{N_{S_0}} d_M^2(\vec{y}_j, \vec{x}_i),$$

where $d_M(\vec{x}, \vec{y}) = \sqrt{(\vec{x} - \vec{y})^T C^{-1} (\vec{x} - \vec{y})}$ is the Mahalanobis distance, C is the covariance matrix of the feature vectors for participants from the reference group S_0, m is the dimension of the feature space.



a



b

Fig. 1 The design of PAD with two Helmholtz resonators (a) and its sensitivity dependency on the frequency of amplitude modulation of the laser source (b).

In the Fig. 2 the set of absorption coefficients of EBS from patients with tuberculosis is used as feature vectors $\vec{x}_i$ of the reference group S_0, the set of absorption coefficients of EBS from other participants are used as feature vectors $\vec{y}_j$ of the group S. The AVMD of EBS absorption spectrum in the 10P and 10R spectral bands of CO_2 laser generation for participants are marked in the Fig. 2 as "integral estimations 1" and "integral estimations 2", correspondently [7].

The photoacoustic signal is proportional to absorbed volume fraction of input light source energy. Therefore, a high-power light sources are preferable. Light sources that have been used in photoacoustic spectroscopy include broadband infrared radiation sources, that is, black-body radiators and light-emitting diodes; but in most cases various lasers (CO_2, CO, diode, quantum cascade, and Nd:YAG lasers) are used [14].

Optical parametric oscillator (OPO) systems provide light power from few 100 mW to more than 1 W in the wavelength range of 2–4 μm. OPOs were first used in photoacoustic detection of organic compounds near 3.3 μm at ppm-level and successfully applied later to measure formaldehyde with ppb and ethane with sub-ppb accuracy [15].

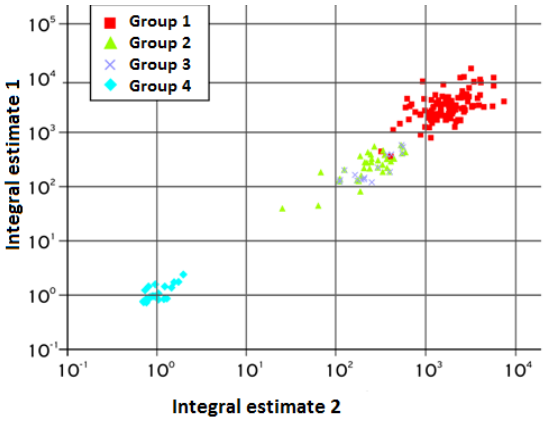


Fig. 2 Distribution of point estimates of absorption spectra of exhaled air. The Group 1 includes healthy participants, the Group 2 includes patients with bronchopulmonary diseases (COPD, asthma, pneumonia), the Group 3 includes nonbronchopulmonary diseases (coronary heart disease, gastric ulcer, duodenal ulcer), the Group 4 includes patients with tuberculosis.

An IR gas sensor combining a continuous-wave (CW) OPO with Cavity Leak-Out spectroscopy (CALOS) was presented [3]. The PPLN nonlinear crystal (19 mm long) contains 19 gratings with poling periods between 28.64 μm and 30.16 μm and is mounted inside a self designed oven for operation at temperatures between 150 and 200 °C. The temperature stability is 8 mK (standard deviation) over 4 hours. The first crystal surface is HR coated for both pump (94.3%) and signal (99.9%) waves thus serving as the common first mirror for both resonators. The PPLN crystal was pumped at 1064 nm (2 W). Dual cavity design in OPO was used for wavelength selection within the tuning range of the OPO (3.1 – 3.8 μm). CALOS cell was based on a high finesse optical resonator (L = 52.5 cm) formed by two highly reflective mirrors (R = 99.985%, Los Gatos). A noise-equivalent absorption coefficient of $1.6 \cdot 10{-}10 \mathrm{cm}^{-1}/\sqrt{\mathrm{Hz}}$ was achieved for integration times up to 180 sec. This corresponds to a detection limit for ethane at sub-ppt level.

The OPO-based spectrometer with PAD (wavelength near 3 μm, 8 MHz linewidth, output power ~1 W) was used for the detection of hydrogen cyanide (HCN) emission from clover leaves, and Pseudomonas bacteria; in addition, the presence of HCN in exhaled human breath was measured [16]. For specific experiments, the spectrometer is operated continuously up to 10 days and has a detection limit of 0.4 ppbv of HCN in air over 10 s, using the P8 rotational line in the ν_3 vibrational band of HCN at 3287.25 cm^{-1}. This provided an overall sensitivity of the system of 2.5×10^{-9} cm^{-1} $Hz^{-1/2}$.

Table 1 Technical characteristics of the spectrometer LaserBreeze [17].

Parameter	Value
Source of radiation	Optical parametric oscillator
The spectral tuning range	2.5 – 10.7 μm
Concentration detection sensitivity, not worse	1 ppb
The number of detected substances, not less	20
The relative error in measuring of the concentration of biomarkers, not more	30 %
The accuracy and selectivity of biomarkers detection, not less	95 %
The volume of the analyzed gas samples for registration of the composition and concentration of biomarkers, not more	50 cm^3
Time of registration of one biomarker in the sample, not more	3 s
Time of registration of 10 biomarkers in the sample, not more	2 min

We used developed by Special technologies Ltd. laser photoacoustic gas analyzer LaserBreeze based on the dual OPO with tuning range 2.5–10.7 μm [17]. Two types of nonlinear elements are used in this OPO: periodically poled lithium niobate structure (PPLN) and mercury thiogallate crystal $HgGa_2S_4$ (HGS). Nd:YLF laser (10 ns, 0.5–1.5 kHz, 1.5 mJ) was used as a pump source. The linewidth of developed OPOs was 3-4 cm^{-1}. The average power of OPO based on PPLN structure was 20mW (1700 Hz). The average power of OPO

Table 2 The binary "One-vs-One" SVM classification quality of the groups under study.

Groups	Kernel parameter	Principal components	Sensitivity		Specificity	
			Mean	Dispersion	Mean	Dispersion
LC- Pneumonia	0.7152	2 and 6	0.96	0.0014	0.93	0.0012
LC- COPD	1.2216	2 and 6	0.98	0.0003	0.94	0.0007
LC - healthy volunteers	0.2698	1 and 5	0.96	0.0011	0.90	0.0013
COPD-Pneumonia	1.2041	2 and 5	0.95	0.0016	0.95	0.0012
COPD-healthy volunteers	1.2414	1 and 5	0.86	0.0022	0.83	0.0020
Pneumonia-healthy volunteers	0.5641	2 and 6	0.96	0.0009	0.92	0.0019

based on HGS crystal was 9 mW (900 Hz). The double channel resonant photo-acoustic cell was used for recording absorption spectra of gaseous samples. Technical characteristics of the LaserBreeze gas analyzer are shown in the Table 1.

The aim of the paper is to show abilities of laser photoacoustic gas analyzer based on OPO with extra wide tuning range for breathomics.

2 Materials and methods

The protocol of the research was approved by the Ethic Committee of the Siberian State Medical University (Tomsk, Russia), Ref. Number 2882 at 24.11.2011. All participants were preliminary informed about details of research and signed "Informed agreement" on the actions carried out. The interaction with the patients was limited by the sampling of a part of exhaled air into a disposable container.

The sampling procedure was carried out before eating or 2 hours thereafter. Before sampling, participants rinsed the mouth with water without any oral cavity cleaning agents. Then participant did some calm breaths through a sterile plastic tube into the sample container (syringe). The "dead volume" was exhaled outside the container.

The study involved four groups: patients with bronchopulmonary diseases including lung cancer (LC) patients (N = 9); patients with chronic obstructive pulmonary disease (COPD) (N = 12); patients with pneumonia (N = 11) and a control group of healthy volunteers (N = 29). All patients had been treated in medical organizations, so the diagnosis has been verified by clinical methods.

Exhaled breath samples were collected in 150 ml disposable plastic containers (syringe) and analyzed using the LaserBreeeze gas analyzer. All measurements were carried out at room temperature (20–25 °C) and humidity (50–60%). We repeat measurements of the EAS absorption spectrum 5 times.

The first step in data analysis was consisted in informative features extraction. The principal component analysis (PCA) is one of the most effective methods in this field. The basic idea of PCA is to transform data to reduced number of new orthogonal variables, termed the principal components [18].

Often, the final goal of breathomics analysis consists in predictive model construction, which can be used for further diagnostics. One of the most efficient approaches to this task is machine learning methods usage, including supervised and unsupervised learning. Usually, the classification model a based on using supervised learning methods. These methods are based on using of a part of experimental data for training of algorithm of classification and other – for testing.

Below we used the support vector machine (SVM) method for classification. SVM provides binary classification and it is based on building up the maximum-width stripe, which spatially separate groups under study. The algorithm is based on analysis of scalar product of the feature vectors. When the building of such stripe is impossible, the kernel transform can help to provide classification, which is based on analysis of scalar product of the feature vectors functions [19].

3 Analysis of the experimental data

Initially we construct all variants of the "One-vs-One" binary classifies between groups under study, using SVM approach with radial basis function (RBF) kernel. First fifteen principal components were used for SVM classification. The random splitting of initial data on teaching and testing sets was repeated 250 times. The optimal kernel parameters had been evaluated using machine learning approach. The Table 2 shows the

Table 3. Results of differential diagnosis of the groups under study

Group	Diagnosis					
	Set right		Set wrong		Did not set	
	Mean	Dispersion	Mean	Dispersion	Mean	Dispersion
LC	0.9565	0.0013	0.0341	0.0011	0.0094	0.0013
COPD	0.8112	0.0091	0.0981	0.0082	0.0907	0.0047
Pneumonia	0.8412	0.0048	0.0991	0.0032	0.0597	0.0025
Healthy volunteers	0.8946	0.0038	0.0901	0.0024	0.0153	0.0018

results of the binary "One-vs-One" classification in terms of the specificity and sensitivity.

These "One-vs-One" classifiers allow one to construct differential diagnosis rules. One of the possible approaches to this task is enumeration of these classifiers for a feature vector of an object under study [20]. Below the differential diagnostics rule was based on the result of "One-vs-One" classifications, which was appeared more times. Diagnosis did not set, if several results of classification (LC-COPD-Healthy-Pneumonia) for definite feature vector from the testing set met the same number of times. The approach was applied to various splitting of the initial data training and testing data sets, while a variation of the average value of accuracy of each diagnosis within the last 20 iterations exceeded 1%. Results of differential diagnosis are presented in table 3.

4 Conclusion

Breathomics is a promising tool for fast and noninvasive medical diagnosis. LPAS is one of the most sensitive and universal methods of VOCs detection in a breath air.

The ability of LPAS technique significantly depends on a range of the used laser source spectral tuning. The presented data of breath air analysis using IR laser photoacoustic spectrometer LaserBreeze based on the dual optical parametric oscillator with extra-wide spectral tuning range shows its high potential in diagnostics of bronchopulmonary diseases. The "profiling" approach, based on of the set of markers control or profile of the absorption spectrum of breath sample as a "fingerprint" of the state is presented. The accuracy of multiclass classification using a set of binary SVM "One-vs-One" classifiers based on spectral analysis of exhaled air of patients is high enough for using in routine practices, especially for screening tests.

On the whole, the future of breathomics practical use demands cost-effective and informative measurement equipment, standardization of the sampling, discovery of most specific biomarkers/profiles of biomarkers, effective methods of data analysis.

Disclosures

All authors declare that there is no conflict of interests in this paper.

Acknowledgments

The presented results were carried out with partial financial support of the FCPIR Contract No. 14.578.21.0082 (ID RFMEFI57814X0082). This work was also performed within the frame of the Fundamental Research Program of the State Academies of Sciences for 2013-2020, line of research III.23.

References

1. A. G. Dent, T. G. Sutedja, and P. V. Zimmerman, "Exhaled breath analysis for lung cancer," Journal of Thoracic Disease 5, 540–550 (2013).
2. M. P. Fernandes, S. Venkatesh, and B. G. Sudarshan, "Early Detection of Lung Cancer Using Nano-Nose - A Review," Open Biomedical Engineering Journal 9(1), 228–233 (2015).
3. F. Kühnemann, F.Müller, G. von Basum, D. Halmer, A. Popp, S. Schiller, P. Hering, and M. Muertz, "CW-OPO based cavity-leak-out spectrometer for ultra-sensitive and selective mid infrared trace gas analysis," Proceedings of SPIE 5337, 117–127 (2004).
4. V. Nikolaev, V. N. Ochkin, and S. N. Tskhai, "Fast recording of weak absorption spectra in optical cavity using tunable laser," Laser Physics Letters 10(11), 115701 (2013).

5. H. W. A. Berkelmans, B. W. M. Moeskops, J. Bominaar, P. T. J. Scheepers, and F. J. M. Harren, "Pharmacokinetics of ethylene in man by on-line laser photoacoustic detection," Toxicology and Applied Pharmacology 190(3), 206–213 (2003).
6. C. Popa, A. M. Bratu, C. Matei, R. Cernat, A. Popescu, and D. C. Dumitras, "Qualitative and Quantitative Determination of Human Biomarkers by Laser Photoacoustic Spectroscopy Methods," Laser Physics 21(7), 1336–1342 (2011).
7. Y. V. Kistenev, A. A. Karapuzikov, "Methods of spectral analysis of exhaled air suitable for routine diagnostics of diseases of the respiratory system," Advanced biomaterials and devices in biomedicine 2, 79–87 (2015).
8. J. A. de Gouw, S. Te Lintel Hekkert, J. Mellqvist, C. Warneke, E. L. Atlas, F. C. Fehsenfeld, A. Fried, G. J. Frost, F. J. M. Harren, J. S. Holloway, B. Lefer, R. Lueb, J. F. Meagher, D. D. Parrish, M. Patel, L. Pope, D. Richter, C. Rivera, T. B. Ryerson, J. Samuelsson, J. Walega, R. A. Washenfelder, P. Weibring, and X. Zhu, "Airborne Measurements of Ethene from Industrial Sources Using Laser Photo-Acoustic Spectroscopy," Environmental Science & Technology 43 (7), 2437–2442 (2009).
9. F. G. C. Bijnen, J. Reuss, and F. J. M. Harren, "Geometrical optimization of a longitudinal resonant photoacoustic cell for sensitive and fast trace gas detection," Review of Scientific Instruments 67(8), 2914 (1996).
10. C.-M. Lee, K. V. Bychkov, V. A. Kapitanov, A. I. Karapuzikov, Y. N. Ponomarev, I. V. Sherstov, and V. A. Vasiliev, "High-sensitivity laser photoacoustic leak detector," Optical Engineering 46(6), 064302 (2007).
11. A. Miklós, P. Hess, and Z. Bozóki, "Application of acoustic resonators in photoacoustic trace gas analysis," Review of scientific instruments 72(4), 1937–1955 (2001).
12. V. Zéninari, R. Vallon, C. Risser, and B. Parvitte, "Photoacoustic detection of methane in large concentrations with a Helmholtz sensor: Simulation and experimentation", International Journal of Thermophysics 37(1), 7 (2016).
13. Y. V. Kistenev, A. I. Karapuzikov, N. Y. Kostyukova, M. K. Starikova, A. A. Boyko, E. B. Bukreeva, A. A. Bulanova, D. B. Kolker, D. A. Kuzmin, K. G. Zenov, and A. A. Karapuzikov, "Screening of patients with bronchopulmonary diseases using methods of infrared laser photoacoustic spectroscopy and principal component analysis," Journal of Biomedical Optics 20(6), 065001 (2015).
14. Yu V. Kistenev, A. V. Borisov, D. A. Kuzmin, O. V. Penkova, N. Y. Kostyukova, and A. A. Karapuzikov, "Exhaled air analysis using wideband wave number tuning range IR laser photoacoustic spectroscopy," Journal of Biomedical Optics 22(1), 017002 (2017).
15. J. Li , W. Chen, and B. Yu, "Recent Progress on Infrared Photoacoustic Spectroscopy Techniques," Applied Spectroscopy Reviews 46, 440–471 (2011).
16. D. D. Arslanov, M. P. P. Castro, N. A. Creemers, A. H. Neerincx, M. Spunei, J. Mandon, S. M. Cristescu, P. Merkus, and F. J. M. Harren, "Optical parametric oscillator-based photoacoustic detection of hydrogen cyanide for biomedical applications," Journal of Biomedical Optics 18(10), 107002 (2013).
17. A. A. Karapuzikov, I. V. Sherstov, D. B. Kolker, A. I. Karapuzikov, Y. V. Kistenev, D. A. Kuzmin, M. Y. Shtyrov, N. Y. Dukhovnikova, K. G. Zenov, A. A. Boyko, M. K. Starikova, I. I. Tikhonyuk, I. B. Miroshnichenko, M. B. Miroshnichenko, Y. B. Myakishev, and V. N. Lokonov, "LaserBreeze gas analyzer for noninvasive diagnostics of air exhaled by patients," Physics of Wave Phenomena 22(3), 189–196 (2014).
18. L. Pomerantsev, O. Y. Rodionova, "Concept and role of extreme objects in PCA/SIMCA," Journal of Chemometrics 28(5), 429–438 (2014).
19. G. R. G. Lanckriet, N. Cristianini, P. Bartlett, L. El Ghaoui, and M. I. Jordan, "Learning the kernel matrix with semidefinite programming," Journal of Machine Learning Research 5, 27–72 (2004).
20. A. V. Borisov, Y. V. Kistenev, D. A. Kuzmin, V. V. Nikolaev, A. V. Shapovalov, and D. A. Vrazhnov, "Development of classification rules for a screening diagnostics of lung cancer patients based on the spectral analysis of metabolic profiles in the exhaled air," Proceedings of the Scientific-Practical Conference "Research and Development - 2016", 573–580 (2016).

Optoacoustic gas-analysis for diagnostics of biosystems

Boris G. Ageev, Olga Y. Nikiforova, Yurii N. Ponomarev*, and Valeria A. Sapozhnikova
V. E. Zuev Institute of Atmospheric Optics SB RAS, Tomsk 634055, Russia

*** e-mail:** yupon@iao.ru

Abstract. A possibility of detecting biogenic gases by the laser optoacoustic gas-analysis method is shown. The construction and specifications of instruments, developed for this purpose, are described. Examples of the analysis of gas samples of various biological objects, like air, expired by patients, suffered from different illnesses, and residual gases in the wood of year rings of conifers are given together with recommendations on applying the received information. © 2019 Journal of Biomedical Photonics & Engineering.

Keywords: spectroscopy; absorption spectra; CO_2 laser; carbon dioxide; tree rings; human breath.

Paper #3311 received 24 Dec 2018; revised manuscript received 20 Mar 2019; accepted for publication 20 Mar 2019; published online 29 Mar 2019. doi: 10.18287/JBPE19.05.010304.

1 Introduction

Optoacoustic method (OA) refers to the group of calorimetric ones. A studying sample (gas, liquid, solid) is the detector of the absorbed power. The OA method is widely used in molecular spectroscopy and gas analysis with the use of different lasers, generating radiation in interval from UV to far IR range. It is characterized by the following properties [1–3]:

1. The OA signal is zero in the absence of the absorption in the sample.
2. The signal-to-noise ratio increases proportionally to the radiation source power, up to the mode of the absorption saturation.
3. The OA signal depends linearly on the concentration of absorbing gas molecules at the concentration variation within 4–5 orders of magnitude.
4. The OA signal amplitude is the intensive parameter of the studied sample, i.e., it does not depend on its sizes. This circumstance allows us to work with gas cells of small volumes, easily controlling in them temperature, pressure, and gas composition.

In High-Resolution Spectroscopy the OA method is successfully used in smoothly wavelength-generating narrow-band lasers, particularly, in the diode ones [4–6]. In the diode-laser spectrometers the resonant OA detector in the form of differential Helmholtz resonator [4] is successfully used, providing for measurements of absorption cross-sections at vibrational-rotational molecular transitions of up to $4 \cdot 10^{-23}$ cm^2/mol.

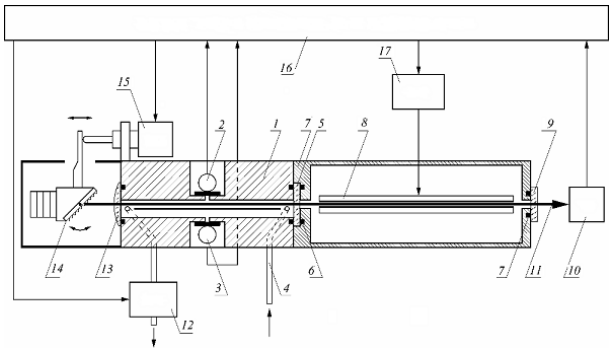
A wide class of gas lasers, generating radiation at molecular transitions of active media, such as CO, CO_2, NH_3, are used in laser OA gas-analyzers for the ecological control of atmospheric contaminations, analysis of the expired air composition, aiming at the diagnostics of bronchopulmonary illnesses, diagnostics of vapors of dangerous chemical compounds, and in series of other applications [7–11].

In this paper, the application of the laser OA gas-analysis to detection of biogenic gases is demonstrated; the constructions and specifications of the used instruments are described; examples of the analysis of different biological samples are presented, such as air, expired by patients, suffering from different illnesses; residual gases in the wood of yearly rings of conifers; and recommendations are formulated on the use of the obtained information.

2 Optoacoustic instrumentation for the analysis of biogenic gases

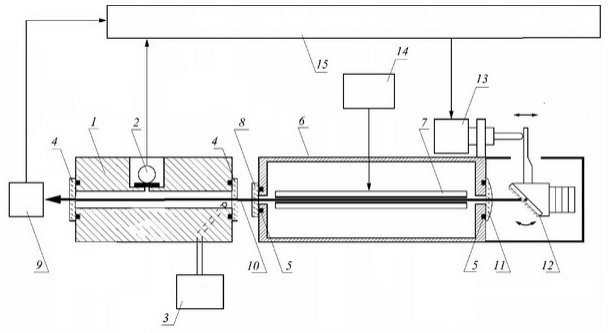
2.1 Description of the construction and specifications of the used instruments

The analytical investigation of gaseous samples from biological objects in the framework of this work conducting was performed with two gas-analyzers: ILPA-1 and OAD-1. The instruments were assembled by one principal scheme (Fig. 1, *a*, *b*) on the base of waveguide frequency-tunable CO_2 lasers [12]. The lasers emit in bands of 10 and 9 μm at more than 70 lines of *P* and *R* branches at an output generation power up to 3 W at strong lines and up to 0.5 W at weak ones.



(a)

1 – optoacoustic detector, 2,3 – microphones, 4 – input-output of gas sample, 5 – passage window, 6 – thickening, 7 – body of the emitter of waveguide CO_2 laser, 8 – waveguide, 9 – output mirror of the laser, 10 – receiver of radiation, 11 – output radiation of the laser, 12 – air pump, 13 – adjusting lens, 14 – unit of retuning of radiation wavelength with diffraction grating, 15 – step actuator of the retuning unit, 16 – unit of control and indication, 17 – HF generator of laser pumping.



(b)

1 – optoacoustic detector, 2 – microphone, 3 – vacuum post, 4 – passage window, 5 – thickening, 6 – body of emitter of waveguide CO_2 laser, 7 – waveguide, 8 – output mirror, 9 – receiver of radiation, 10 – output laser radiation, 11 – adjusting lens, 12 – unit of retuning of radiation wavelength with diffraction grating, 13 – step actuator of the retuning unit, 14 – HF generator of laser pumping, 15 – unit of control and indication.

Fig. 1 Schemes of laser optoacoustic gas-analyzers: ILPA-1 (a) and OAD-1 (b).

Each device has its own constructive properties: the ILPA-1 is a transportable instrument, produced in small series (company "Special technologies" Ltd, Novosibirsk), and has an intra-resonator location of the detector [13]. In the instrument, the resonant differential OA flow-type detector is used, which allows pumping of the gas sample with the air pump through the detector. The gas-analyzer sizes are 91.5×31.0×16.0 cm, and its weight is no more than 27 kg. The instrument exterior is shown in Fig. 2. The instrument OAD-1 (our proper elaboration) [10] is a stand variant of ILPA-1 one with the beyond-resonator detector of non-resonant type. The detector evacuation and filling in with a sample of the studying gas are performed with the help of the vacuum post. As well, there are differences in the element bases of the gas-analyzers, the most important of which are the modification of laser sources and the type of the used microphones.



Fig. 2 General view of gas-analyzer ILPA-1.

The operation of the gas-analyzers is based on the OA effect, arising in the result of absorption of CO_2 laser radiation by gases. The control for the radiation spectrum retuning is performed with the help of the personal computer through the control block with the use of the specially developed computer program ILPA Sensor. Laser radiation passes through the OA detector, which is a cylindrical cell with condenser microphones, build in the side wall. Gas molecules, having absorption lines at the CO_2 laser wavelengths, absorb the modulated radiation of the laser. In this case, acoustic vibrations at the modulation frequency are formed inside the OAD and are recorded by microphones. The value of the measured acoustic signal, normalized to the magnitude of the laser radiation power, is proportional to the magnitude of the molecular absorption at the given concentration of the absorbing gas in the sample. Signals of the detector microphone *mic* and radiation receiver *pyro* are put first to wideband preamplifiers and then to the system of measuring and recording, based on sound cart of the personal computer. As the measurement result, a file appears with recorded values of *mic*, *pyro*, and *absorption* = *mic*/*pyro* at corresponding generation lines, i.e., the analog of the sample absorption spectrum. The information on the recorded spectrum is displayed also on the monitor of the computer, controlling gas-analyzers.

In order to determine the concentration of gaseous components in the studied samples, it is necessary to transform values of gas-analyzer signals, measured in relative units into the value of concentration of the absorbing component in absolute units, for example, in ppm. For this purpose, it is necessary to calibrate gas-analyzers to a gas mixture with the known concentration. To do this, we used the reference gas

mixture CO_2-N_2 (PGS, "PGS service" Ltd, Zarechny town) with a certified content of CO_2, equal to 5000 ppm in N_2. Plots of the obtained gas-analyzer signals are shown in Fig. 3. Certain difference of derived curves from the CO_2 absorption spectrum profile is caused, apparently, by distinct measuring conditions, specifically, an intra-resonator location of the ILPA-1 gas-analyzer detector. This can matter for spectral line parameters study (form, half-width, strength, etc.). For gas-analysis measurements this circumstance can be take into account the detector calibration on utilized laser lines.

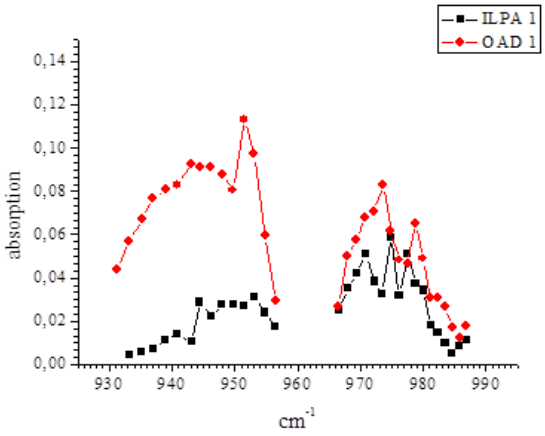


Fig. 3 Spectra of signals of laser optoacoustic gas-analyzers ILPA-1 and OAD-1 when filling in cells with a reference gas mixture of 0.5% CO_2 in N_2 at a general pressure of 1 atm (Y-axis – absorption in arbitrary unit of gas-analysers output signals, X-axis – laser line wavenumber in cm^{-1}).

Since the calibration mixture includes only two components, and the nitrogen does not absorb at generation lines of CO_2 laser, we can mind that the recorded signal depends only on CO_2 absorption. The absorption by the calibrated mixture at CO_2 laser lines was calculated in accordance with parameters of spectral lines from the HITRAN database.

2.2 Description of gaseous samples preparation

When conducting analytical measurements, the preparation of samples is very important. We also paid a sufficient attention to this problem. Note that measurements of expired air were conducted with the gas-analyzer ILPA-1, while the gas content in the wood annual rings was measured with the gas-analyzer OAD-1.

2.2.1 Preparation of gaseous samples of expired air

Under standard conditions, there are about 400 volatile compounds in expire air [14]. A part of compounds, for example, CO_2, N_2, O_2, couples of H_2O reside in the expiration of all peoples in some or other proportion, but the presence or increased concentration of other compounds can testify the fact that a person is ill or under certain stress impact. At the present time, facilities for gathering air, as a rule, make a series of nonstandard devices, produced by researchers themselves. In order to separate a definite gaseous component, the catchers are used, working on one or other principle.

One of the technological problems in gathering samples of expired air is in creating of comfortable conditions for patients, making easy the expiration into the gathering device. In our case, the calibrated gas injector from a serially made spirometer of a volume of 1 liter was used for gathering samples of the expired air. Its nozzle part was changeable in order to escape the risk of infecting.

Air, expired by peoples, is not homogeneous. An adult healthy person expires 0.5 liter of air or more at each breathing cycle. The first 150 ml are expired from the volume of upper breathing tracts, free of the exchange of gases. The informative air samples are to be taken from the pulmonary depth. Therefore, the reserve air volume was used for the gas analysis, expired by a patient into the injector after the corresponding instruction and under the control of medical nurse. Then the input end of the gas-analyzer's probe was put into injector and the mixture was pumped through the detector cell at operation of the gas-analyzer at a chosen radiation wavelength. At reaching the detector signal, maximal for the given value of the letting in, the pumping was cut off, and the wavelength has been scanned throughout the spectrum. At the first stage of investigations on spectroscopic analysis of the expired air by patients we used gas samples without any selection of gaseous components in order to escape any information losses.

The problem of gaseous samples contamination is actual, because there exist admixtures of volatile chemical compounds in any room. These trace compounds were taken into account as the background "noise" in the process of investigations. To increase the reliability of results, we conducted a spectral analysis of room air and air inside the injector immediately before and after series of measurements of expired air.

2.2.2 Preparation of gaseous samples from wooden annual rings of conifer cuts

In the analysis, cuts of conifers were used, which were stored from 6 months to several years under laboratory conditions, therefore, the wood of cuts can be thought room-dry. As it follows from the literature, the carbon dioxide is generated by living cells of the wood and stores in the tree stem, because the cambium (a layer of conducting tissues between the bark and wood of the stem) is relatively impermeable for diffusion of gases [15]. In order to develop the method for preparation of samples, we have conducted a testing experiment. An example of the wood ring sample was put into the hermetically sealed exposition chamber with room air under atmospheric pressure. The sample was in the

chamber during ~ 6 months, and then an air sample was taken from the chamber for measuring OA absorption signals. After so long exposition, we failed to fix any difference in the magnitude of OA signals from the sample and air. Therefore, in our following measurements we used the vacuum extraction of gaseous samples from wood rings.

The wood of rings was planed away with special chisels, weighted, and then put in sealed exposition chambers, which were subjected to a short-time evacuation for stimulating the output of the gas, and after 20 minutes measurements began. It was checked that just this time is required for the most intensive emission of gases from wood ring samples. During measurements the gaseous sample from each exposition chamber (at a pressure of ~ 6 Torr) was input into sealed OA cell and air was added up to a general pressure of the gaseous mixture of 100 Torr, at which the optimal sensitivity of the detector has been reached. Each series of measurements of values of absorption by analyzed samples was accompanied by measurements of magnitudes of the background absorption by air. The value of difference in absorption by the gaseous sample and by air was informative, it served for determination the relative content of the absorbing component in the sample for each ring with the help of calibrating plot.

3 Investigation of the carbon dioxide in expired air

The noninvasive diagnosis of the human organism state through the analysis of the expired air is very attractive, because together with molecules–biomarkers of different illnesses it contains a few percent of CO_2, which concentration also attests the state of the human health [16, 17].

The carbon dioxide itself is not a specific marker of certain illness. By data of [18], in expired air of healthy people its concentration is commonly about 4.5%, but higher values, were also observable, which were conditioned by different causes, such as: infecting by the *Helicobacter pylori* bacteria; the food passing through gastrointestinal tract; dysfunction of the liver, including cirrhosis; excessive growth of bacteria; dysfunction of the pancreas, metabolism of the bile; metabolism of the glucose, etc. In [19] and [20] somewhat less values were obtained: the concentration of the carbon dioxide in expired air of 39 healthy volunteers, aged from 21 to 61 turned out to fall into interval between 1.9 and 4%, at an averaged value of 2.8%; and about 4% of CO_2 was found in the sample of expired air of 16-aged patient-asthmatic. Possibilities of capnometry in the screening of illnesses of respiratory and cardiovascular organs were studied in [17], in which as the critical value of CO_2 concentration in the expired air for diagnostics of illnesses was proposed a magnitude of 4.6%, despite the fact, showing that it is impossible to separate these illnesses by the CO_2 concentration value.

Below we show measurement results for the carbon dioxide concentration in expired air of healthy persons and patients, suffering from different illnesses. The results were obtained from absorption spectra, recorded with the help of the ILPA-1 gas-analyzer. Since absorption coefficients for CO_2 at lines of CO_2 laser generation differ less than by two times, the CO_2 concentration in samples of expired air was determined by the single-wave method.

In the group of the examined patients with different somatic illnesses from the Tomsk Regional clinical hospital and City hospital no. 3: 11 persons with bronchial asthma and coronary heart ischemia (COI), 12 patients with the community-acquired pneumonia, 17 patients with chronic obstructive pulmonary disease (COPD), 4 patients with ulcer of stomach, and 3 patients with ulcer of duodenum. In the test sampling of expired air participated healthy persons (students of Siberian State Medical University (117 samples)).

Fig. 4 shows an example of the obtained absorption spectra of expired air from range 933-988 cm^{-1}.

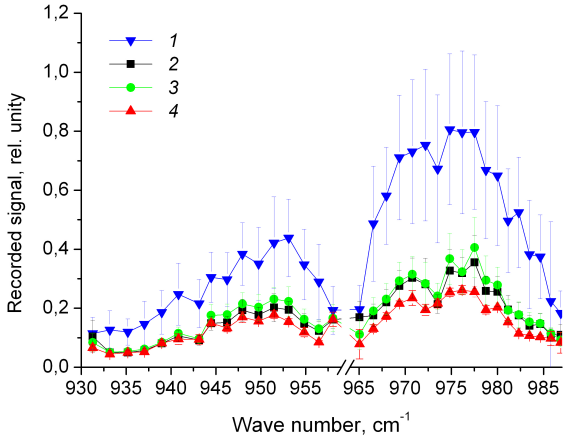


Fig. 4 Absorption spectra of expired air in range 933–988 cm^{-1} for healthy persons (*1*) and patients with bronchial asthma (*2*), COI (*3*), and duodenal ulcer (*4*).

Note that for the recorded spectra a wide dispersion is characteristic. Because such dispersion in measurements, made with the reference gaseous mixture, was not observed, we suppose that this dispersion is caused by the variability, characteristic for living objects.

That for range of wave numbers 967–985 cm^{-1} a greater dispersion of data is characteristic, than for 933–950 cm^{-1}, nonetheless, the CO_2 concentration was calculated for signals at each generation line in range 933–988 cm^{-1} and then the least value was chosen. It was found during the process that a lesser values of CO_2 concentration corresponded to the absorption at lines, close to 946 cm^{-1} for healthy persons and close to 975 cm^{-1} for patients with differing illnesses. The high values of the CO_2 concentration obtained by the magnitude of absorption at other lines can be conditioned by absorption by other gases, residing the expired air.

Fig. 5 and Table 1 show values of CO_2 concentrations in expired air for all groups of examined peoples. Since the obtained values of the CO_2 concentration not always corresponded to normal distribution law [11], results are presented in the form of the median Me and 25%- and 75%- quartiles Q_1 and Q_3.

Table 1 Values of CO_2 concentration (%) for all examined groups.

	Examined groups	Size of a group	Me (Q_1; Q_3)	Min	Max
1	Healthy peoples	117	5,6 (4,6; 6,8)	1,9	11,1
2	Patients with bronchial asthma	11	2,7 (2,0; 3,3)	1,8	3,6
3	Patients with COPD	17	3,2 (2,4; 3,4)	1,0	3,9
4	Patients with community-acquired pneumonia	12	2,8 (2,2; 3,7)	1,1	4,6
5	Patients with coronary heart disease	11	3,1 (2,4; 3,6)	1,9	3,9
6	Patients with duodenal ulcer	3	2,1	2,0	2,2
7	Patients with stomach ulcer	4	2,1 (2,0; 3,1)	1,9	3,5

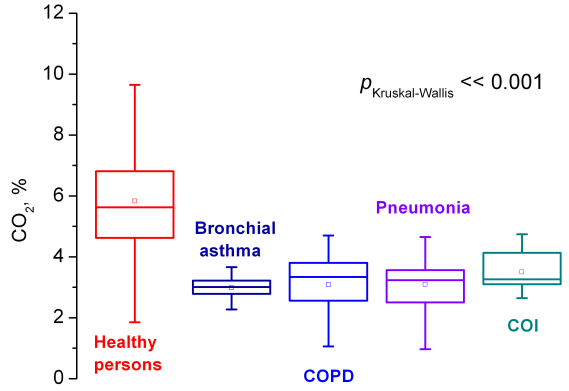


Fig. 5 CO_2 concentration in expired air of healthy persons and patients with bronchial asthma, COPD, pneumonia, and coronary heart disease.

Obtained values of the CO_2 concentration in expired air of healthy peoples are significantly higher, than of patients with different illnesses: the p-value by the Kruskal-Wallis test is $p << 0.001$, however, we failed to discern patients by illnesses, using the value of CO_2 concentrations. The highest differences are observed, when comparing patients with bronchopulmonary disease and coronary heart disease (51 persons) and patients with ulcer (7 persons); by Mann-Whitney test, p-value was 0.054, by the Student's t-test for equal variance assumed, $p = 0.053$, and only for equal variance not assumed $p = 0.026$, however, the application of the Student's t-test is rightful only for normally distributed data, but in accordance with Shapiro-Wilk normality test in this case it was not so ($p = 0.374$). Significant differences between these two groups of patients can be found only under supposition that CO_2 concentrations in expired air of patients with ulcer are lower than of patients with other diseases. In this case, when applying one-tailed Mann-Whitney test, $p = 0.028$. However, by data of work [18] the infecting by the bacteria *Helicobacter pylori* should cause the increase of the CO_2 concentration.

On the whole, the obtained values of CO_2 concentration in expired air of patient with bronchopulmonary and cardiovascular illnesses is somewhat lower than the corresponding literature data (4.6% [17] and 4% [20]), and in expired air of healthy persons they are a few higher (4.5% [18] and 1.9–4% [19]), however, by data from [21] the CO_2 concentration strongly depends on the state of the examined persons and conditions, in which they live: a variation of the CO_2 concentration, exceeding 1.5 times, was found in expired air of one and the same person, measured in the morning and in the evening. In addition, possibly, the age of persons also is significant for measurements. The age of healthy peoples did not exceed 22 years, and samples from these persons were taken in various time of a day, while ill patients mostly were significantly older, and samples of expired air were taken from them in the first half of a day.

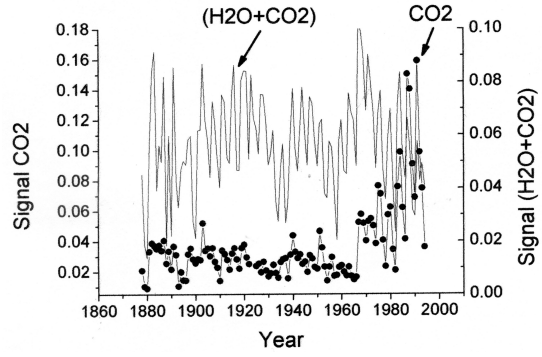
4 Investigation of gas content in the wood of annual rings of trees

Forest communities are self-regulating systems and possess of high resistance to varying environmental conditions, however, change drastically of climate can cause irreversible consequences. To forecast such nature-climatic changes, investigations of chronologies of annual tree ring widths are widely used [22, 23]. However, the investigation of solely chronologies of rings' width cannot give a complete notion about the influence of external conditions on the tree growth, therefore, the analysis of the common behavior of widths and gas components of rings is required, which can make deeper the understanding of complex processes, connected with the tree growing.

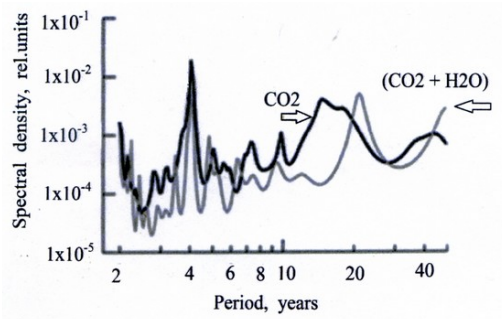
It is known that CO_2 is the basic gaseous component of the stem wood. This gas is formed during respiration of the stem cells and roots [24]. It is also known that a

certain quantity of water retains in wood stems even after wood drying. We put forward a hypothesis that the residual water of old discs (bound water) can include a part of those CO_2, which has been formed when the ring grew, and proposed to use the vacuum method for extracting a gaseous sample, containing CO_2 in the wood. To analyze the extracted sample, we used OA gas-analyzer OAD-1 with frequency-retuning CO_2 laser.

Applying a specially working out method [25] we have conducted the isotope analysis of the desorbed gas in order to argue that the extracted CO_2 is not introduced from the atmosphere. Results have shown that gas samples, desorbed from discs of pine, Siberian stone pine, larch, and spruce are enriched by the light isotope ^{12}C up to values ($\delta^{13}C$) = −25.3‰ for spruce; vary between −25‰ (1894) and −36.4‰ (1986) for Siberian stone pine, between $\delta^{13}C \approx -25$‰ and $\delta^{13}C \approx -30$‰ for larch, and between $\delta^{13}C \approx -25$‰ and $\delta^{13}C \approx -34$‰ for pine (Tomsk region, Russia), $\delta^{13}C = -27$‰ for Siberian stone pine root and $\delta^{13}C = -33.5$‰ for pine root. Evidently, the studied CO_2 is produced by stems and roots, but not introduced from the atmosphere, because the isotope composition of the atmospheric CO_2 is equal, on the average, to –8.5‰ [26].



(a)



(b)

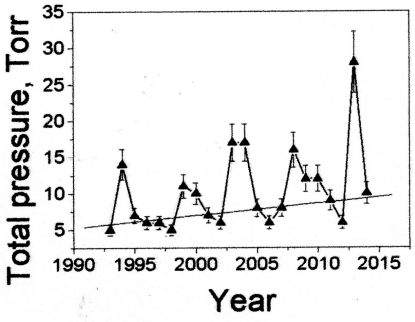
Fig. 6 The content of CO_2 and (CO_2 + H_2O) in annual rings of the Siberian stone pine (rel. units), depending on the year (*a*); power spectra of the CO_2 and H_2O + CO_2 (at 95% confidence intervals) (*b*).

In the result of the experiment we obtained chronologies of CO_2, (CO_2 + H_2O), H_2O, conserved in discs, and pressure variations of gas probes, desorbed from the tree ring wood, the analysis of which allowed revealing a series of characteristics:

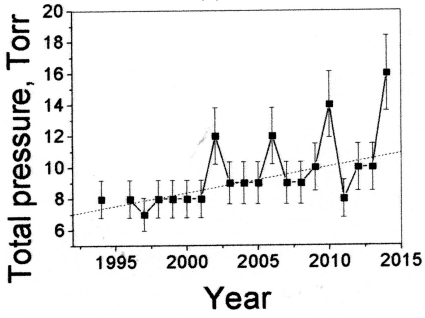
1. *The obtained chronologies are related with climatic parameters.* Investigations of discs of conifer trees (cedar, larch, spruce, pine), grew in the moderate band of West Siberia (Tomsk region), have shown stable fluctuations with the period, close to 4 years, in the obtained chronologies of CO_2, (CO_2 + H_2O) (Fig. 6).

Variations with such a period are found in the near-ground temperature, precipitations, and low cloudiness number near Tomsk. The analysis of chronologies of the CO_2 and CO_2 + H_2O for the Siberian stone pine (age of about 110 years) points to the possible leading role of precipitations in 4-year fluctuations of the content of gases in the disc. It is possible that there proceeded the synchronization of own quasi-periodical biological processes in the close period with a periodical external impact. Cross-spectral analysis of these chronologies with the index of the solar activity points to their phase synchronization with 11-year solar cycle [27].

2. *The emitting of CO_2 by large roots and pressure variation in wood rings has a cyclic character.* The question on the role of the root system in the CO_2 transfer to the tree stem remains controversial up to now [28]. Investigations of discs of large wood roots by the proposed method have shown that the year-by-year variations of CO_2, (CO_2+H_2O), and total pressure of a gas sample in the wood of root rings are characterized by the cycle, close to 4 years (Fig. 7, 8).

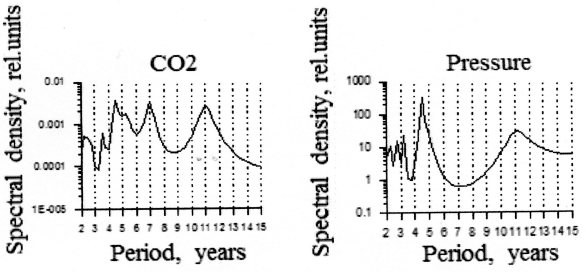


(a)



(b)

Fig. 7 Variation of total pressure of gaseous samples, extracted by the vacuum method from wood rings of the pine (a) and Siberian stone pine (b) roots.



(a) (b)

Fig. 8 Power spectra of variations of the CO_2 content (a) and total pressure (b) in the pine root rings.

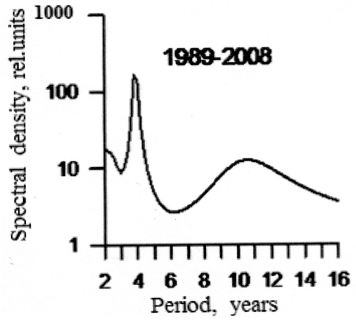
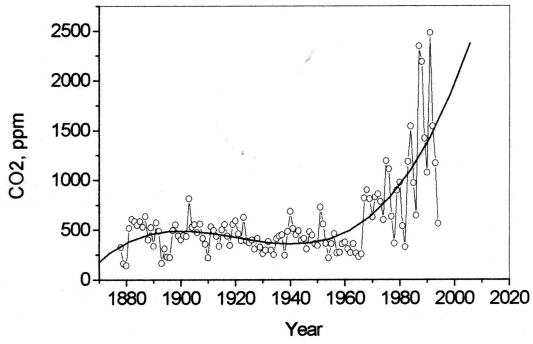
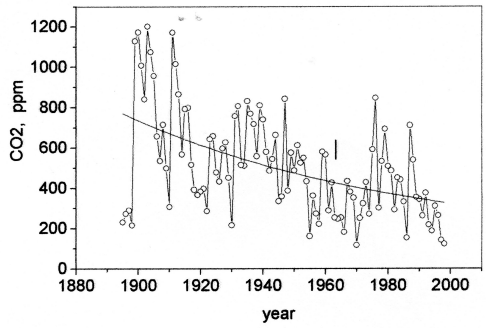


Fig. 9 The result of the spectral analysis of the digitized data from [29] on the global CO_2 efflux from the soil to the atmosphere (the trend is removed).



(a)



(b)

Fig. 10 The comparison of the year-by-year trends of CO_2 content by rings of the Tomsk Siberian stone pine (*a*) and the Siberian stone pine, grown on the Seminsky Range (b).

The hypothesis was proposed that the CO_2 diffuse efflux (root respiration) from large roots into the soil and then in the atmosphere also has a cyclic character. The data processing of the work [29] on the CO_2 extraction by the soil from this position has shown that the made proposition is true, because the result of the spectral analysis of digitized data from [29] distinctly discerns the 4-year cycle, which can be related with the root respiration (Fig. 9).

3. *CO_2 chronologies of trees from different sites are different*. The conducted investigations have shown that chronologies of trees, which were grown in different regions, turned to be different. For comparison, present data on the CO_2 content in rings of Siberian stone pine discs, grown in the south of the Tomsk region (Fig. 10, a) and on the Seminsky Range (Mountain Altai) (Fig. 10, *b*). In the first case (Fig. 10, a) the increase of the CO_2 content is attributed by us to the variations of atmospheric conditions: the increase of the atmospheric content of CO_2 and varying in it ratio of carbon isotopes [10]. In the second case (Fig. 10, *b*) in mountain conditions, the increased solar radiation and a shorter vegetation period, possibly, influence on the total decrease of CO_2 content.

In such a way, it was found that in old discs of conifers 1) the year-to-year distribution of the content of CO_2 exists, sorbed by the wood; 2) CO_2 concentrations in the wood of rings often exceed the atmospheric one; 3) with the increase of tree age the CO_2 content in disc rings is observed, correlating with the increase of the atmospheric CO_2; 4) the found variations of the pressure of residual gases in discs point to the fact that the diffuse emission of CO_2 by stems and roots into the atmosphere is of cyclic character, therefore, many-year measurements are required for the correct estimate of the forest CO_2 emission.

5 Conclusions

Investigations of the CO_2 content in gas samples of expired air by ill and healthy peoples, as well as CO_2 content in gas samples, extracted from wood rings of stems and roots of conifers, were conducted by the method of laser optoacoustic spectroscopy with the use of two types of OA spectrometers-gas analyzers.

The differences in the CO_2 concentration in the expirations of examined healthy persons and patients with different illnesses were found: *p*-value by the Kruskal-Wallis test is $p << 0.001$.

The analysis of the yearly content of CO_2 has shown that variations of CO_2 concentrations are characterized by the cyclicity with a period of 4 years both for woody rings of stems and for rings in large roots, which is related with cyclic characteristics of regional climate.

In the result of investigations, the method of the samples preparation and experimental data analysis was worked out, applicable to a wide range of investigations of gas emissions by biological systems both under stationary (laboratory stand) and mobile (medical institutes) conditions.

Disclosures

All authors declare that there is no conflict of interests related to this paper.

Acknowledgements

This work was made in framework of projects AAAA-A17-117033010037-0 and AAAA-A17-117021310151-7 of the program of fundamental scientific researches of state academies of sciences for 2013–2020 years.

References

1. A. B. Antipov, V. A. Kapitanov, Y. N. Ponomarev, and V. A. Sapozhnikova, Photo-Acoustic Technique in Laser Spectroscopy of Molecular Gases, Nauka, Novosibirsk (1984).
2. V. P. Zharov, V. S. Letokhov, Photo-Acoustic Spectroscopy, Nauka, Moscow (1984).
3. B. G. Ageev, Y. N. Ponomarev, and B. A. Tikhomirov, Nonlinear Photo-Acoustic Spectroscopy of Molecular Gases, Nauka, Novosibirsk (1987).
4. V. Zeninari, V. A. Kapitanov, D. Courtois, and Y. N. Ponomarev, "Design and characteristics of differential Helmholtz resonant photoacoustic cell for gas detection," Infrared Physics & Technology 40(1), 1–23 (1999).
5. V. A. Kapitanov, Y. N. Ponomarev, I. S. Tyryshkin, and A. P. Rostov, "Two-channel opto-acoustic diode laser spectrometer and fine structure of methane absorption spectra in 6070–6180 cm^{-1} region," Spectrochimica Acta Part A: Molecular and Biomolecular Spectroscopy 66(4–5), 811–818 (2007).
6. V. A. Kapitanov, Y. N. Ponomarev, "High resolution ethylene absorption spectrum between 6035 and 6210 cm^{-1}," Applied Physics B 90(2), 235–241 (2008).
7. S. Bernegger, M. W. Sigrist, "CO-laser photoacoustic spectroscopy of gases and vapours for trace gas analysis," Infrared Physics 30(5), 375–429 (1990).
8. P. L. Meyer, M. W. Sigrist, "Atmospheric pollution monitoring using CO_2-laser photoacoustic spectroscopy and other techniques," Review of Scientific Instruments 61(7), 1779–1807 (1990).
9. V. S. Starovoitov, S. A. Trushin, and V. V. Churakov, "Use of lasers on isotope-substituted CO_2 molecules in optoacoustic control of atmospheric pollution," Journal of Applied Spectroscopy 59(5-6), 855–859 (1993).
10. B. G. Ageev, Y. N. Ponomarev, and V. A. Sapozhnikova, "Laser photoacoustic method for disc tree-ring gas analysis," World Environment 2(2), 4–10 (2012).
11. B. G. Ageev, O. Y. Nikiforova, "Optoacoustic determination of carbon dioxide concentration in exhaled breath in various human diseases," Journal of Applied Spectroscopy 83(5), 820–825 (2016).
12. I. V. Sherstov, K. V. Bychkov, V. A. Vasiliev, A. I. Karapuzikov, V. V. Spitsin, and S. B. Chernikov, "Two-channel CO_2 laser system for heterodyne lidar," Atmospheric and oceanic optics 18(3), 248–253 (2005).
13. A. I. Karapuzikov, I. V. Sherstov, B. G. Ageev, V. A. Kapitanov, and Y. N. Ponomarev, "Laser sensors-gas analyzers based on smart waveguide CO_2 lasers and resonance photoacoustic detectors and their applications," Atmospheric and oceanic optics 20(5), 418–423 (2007).
14. M. Phillips, "Breath tests in medicine," Scientific American 267(1), 74–79 (1992).
15. P. J. Kramer, T. T. Kozlowski, Physiology of Woody Plants, Academic Press, New York (1979).
16. V. I. Kuznetsov, S. A. Tarakanov, N. I. Ryzhakov, V. T. Kogan, A. V. Kozlenyuk, and A. A. Rassadina, "Method of highly sensitive non-invasive diagnostics of functional states of organism," Journal of New Medical Technologies 1 (2013).
17. D. V. Lapitski, R. F. Ermolkevich, S. M. Metelski, A. N. Ryapolov, I. A. Manichev, and V. G. Scherbitski, "Capnometry screening ability of ventilatory and circulatory disorders," Military medicine 1(30), 54–57 (2014).
18. S. I. Lukash, "Problems of diagnostics of some diseases on exhaled air," Computer means, networks and systems, 9, 62–71 (2010).
19. K. Stamyr, O. Vaittinen, J. Jaakola, J. Guss, M. Metsälä, G. Johanson, and L. Halonen, "Background levels of hydrogen cyanide in human breath measured by infrared cavity ring down spectroscopy," Biomarkers 14(5), 285–291 (2009).
20. J. H. Shorter, D. D. Nelson, J. B. McManus, M. S. Zahniser, S. R. Sama, and D. K. Milton, "Clinical study of multiple breath biomarkers of asthma and COPD (NO, CO_2, CO and N_2O) by infrared laser spectroscopy," Journal of Breath Research 5(3), 037108 (2011).
21. S. I. Lukash, "Development of the technique of measurement CO_2 in exhaled air," Computer means, networks and systems 10, 119–125 (2011).
22. D. V. Tishin, "Dendroclimatological study of Picea x fennica (Reg.) Kom. on the south border of its geographical range," Uchenye Zapiski Kazanskogo Universiteta. Seriya Estestvennye Nauki 150(4), 219–225 (2008).
23. E. A. Vaganov, S. G. Shiyatov, and V. S. Mazepa, Dendroclimatic Study in Ural-Siberian Subarctic, Nauka, Novosibirsk (1996).

24. R. O. Teskey, A. Saveyn, K. Steppe, and M. A. McGuire, "Origin, fate and significance of CO_2 in tree stems," New Phytologist 177, 17–32 (2008).
25. B. Ageev, Y. Ponomarev, V. Sapozhnikova, and D. Savchuk, "A laser photoacoustic analysis of residual CO_2 and H_2O in Larch stems," Biosensors 5(1), 1–12 (2015).
26. M. Rubino, D. M. Etheridge, C. M. Trudinger, C. E. Allison, M. O. Battle, R. L. Langenfelds, L. P. Steele, M. Curran, M. Bender, J. W. C. White, T. M. Jenk, T. Blunier, and R. J. Francey, "A revised 1000 year atmospheric $\delta^{13}C$-CO_2 record from Law Dome and South Pole, Antarctica," Journal of Geophysical Research: Atmospheres 118(15), 8482-8499 (2013).
27. V. A. Sapozhnikova, A. N. Gruzdev, B. G. Ageev, Y. N. Ponomarev, and D. A. Savchuk, "Relationship between CO2 and H2O variations in tree rings of Siberian stone pine and meteorological parameters," Doklady Earth Sciences 450(2), 652–657 (2013).
28. S. E. Trumbore, A. Angert, N. Kunert, J. Muhr, and J. Q. Chambers, "What's the flux? Unfaveling how CO_2 fluxes from trees reflect underlying physiological processes," New Phytologist 197(2), 353–355 (2013).
29. B. Bond-Lamberty, A. Thomson, "Temperature-associated increases in the global soil respiration record," Nature 464(7288), 579–582 (2010).

Application of Yb,Er:Glass laser radiation for active drug delivery at the treatment of onychomycosis

Andrey V. Belikov, Anastasia D. Tavalinskaya*, Sergey N. Smirnov, and Andrey N. Sergeev
ITMO University, 49 Kronverksky Pr., Saint Petersburg 197101, Russian Federation

*** e-mail:** ntavalin@gmail.com

Abstract. The paper discusses the active delivery of a drug (methylene blue solution) through the Er:YLF-laser-perforated nail plate using pulsed radiation of microsecond Yb,Er:Glass laser. Different methods of laser impact on liquid drug are considered: by focused and diverging laser beam. It was established that both discussed methods can provide sufficient dose of the drug for the treatment of onychomycosis. © 2019 Journal of Biomedical Photonics & Engineering.

Keywords: laser; drug delivery; nail; hydrodynamic effects; treatment of onychomycosis; photodynamic therapy.

Paper #3318 received 15 Jan 2019; revised manuscript received 15 Mar 2019; accepted for publication 23 Mar 2019; published online 30 Mar 2019. doi: 10.18287/JBPE19.05.010305.

1 Introduction

Drug delivery remains an important task, including in the treatment of one of the common pathologies of the nail – onychomycosis. Currently, the treatment of onychomycosis with the help of local drugs, including photodynamic preparations, is ineffective, since the low permeability of the nail plate limits the delivery of a therapeutically sufficient amount of the drug to the lesion. Solutions of methylene blue [1], radachlorin [2], photoditazine [3], etc. are often used as photodynamic preparations. The permeability of the nail plate can be increased using chemical (acids, alcohols, glycols, etc.), physical (microperforation, iontophoresis, sonophoresis, electroporation; ultrasonic and laser drug delivery) and mechanical (injection, nail plate removal or mechanical perforation) [4–12] methods. Delivery can be passive or active. The latter occurs as a result of any external impact.

To accelerate the delivery of drugs under the nail plate, an array of microholes is used, created, among other methods, as a result of exposure to laser radiation. Amount of the drug delivered increases in proportion to the increase in the number of microholes in the array. In the paper [11] CO_2-laser-produced microperforation of the nail plate allowed to target the "Exelderm" in the form of liquid solution and cream with 1% Sulconazole nitrate concentration to the depth of more than 370 μm. In Ref. [13] the fractional CO_2-laser assisted drug delivery for effective and safe treatment of onychomycosis is discussed. It is shown that tazarotene 0.1% gel and tioconazole 28% solution are effective in onychomycosis treatment, moreover, the thermal impact of CO_2-laser radiation is suggested to play a positive role in fungi destruction. For efficient microperforation, Er:YLF laser radiation [14] can also be used.

Unfortunately, drugs have an extremely low penetration rate in passive delivery including through an array of microholes. The passive drug delivery of water-alcohol methylene blue (MB) solution requires about 60–120 s, and water solution of MB do not penetrate through microholes with diameter 220–350 μm [15].

The impact of pulsed radiation of near and middle IR lasers can initiate hydrodynamic effects in liquids. Experimental studies shown that irradiation of water with pulses of Er:YAG [15], Er:YSGG [17], Ho:YAG [17,18] and Yb,Er:Glass [19–21] lasers, whose wavelengths lie near its intense absorption bands, can stimulate the appearance of thermoelastic waves and cavitation processes in water, accompanied by the generation of pressure transients. In Refs. [19–21] the hydrodynamic effects initiated in water by microsecond pulses of Yb,Er:Glass laser with a wavelength of 1.54 μm are considered in detail. A significant influence of these effects on the removal efficiency of soft tissue was established [20, 22].

The rate of penetration of drugs into biological tissue can be increased due to the excitation of laser-induced hydrodynamic effects [23, 24]. In Ref. [24], a method used laser-induced hydrodynamic shock waves was proposed and investigated for the rapid delivery of solid microparticles, nanoparticles and fluids into tissues through multiple microchannels created as a result of Er:YAG laser fractional microablation. Among

other things, it was shown that the active delivery of ZrO_2 particles to microchannels induced by hydrodynamic shock waves generated by Er:YAG laser pulses performed at very high speed.

Unfortunately, the method combining effective laser microperforation and effective active laser delivery of drugs for the treatment of onychomycosis is not still described in literature. This stimulated the authors of this work to study the active delivery of a photodynamic drug (0.25% methylene blue aqueous solution) to the nail bed through a single microhole (created in the nail plate by Er:YLF laser pulses) as a result of the excitation of hydrodynamic processes in the drug solution by the radiation of Yb,Er:Glass laser.

Thus, the purpose of the current study is to determine the possibility of active laser delivery of the aqueous solution of methylene blue through a single microhole in the nail plate *in vitro*, determining the dependence of the number of pulses required for active laser drug delivery and the mass of the drug penetrated under the nail plate on the thickness of the drug layer, with diverging and focused Yb,Er:Glass laser radiation.

2 Materials and methods

In experiments *in vitro*, the samples used represented fragments of healthy nail plates of 7 volunteers aged 22–45 years (2 men and 5 women). Fragments were obtained as a result of mechanical cutting of the upper edge of the nail as it grows normally. A total of 250 samples were examined. Samples were stored outdoors at room temperature in a dark place for no more than 30 days. Before experiments, the samples were mechanically cleaned of dirt and washed with distilled water. The average thickness of the samples was 350 ± 20 μm.

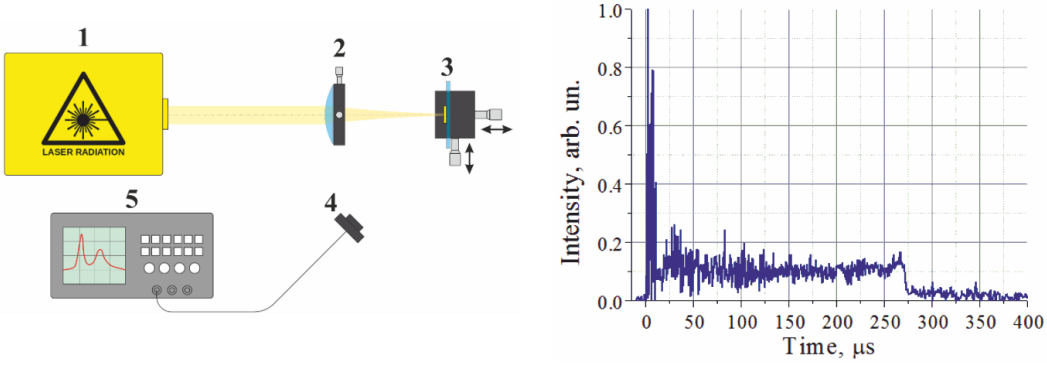
To produce microholes in the nail plate, Er:YLF laser radiation (λ = 2.81 μm) was used. The scheme of the experimental setup is shown in Fig. 1(a). The pulse duration of the Er:YLF laser was 270 ± 10 μs (base) (Fig. 1(b)).

The laser pulse energy (E) was 4.0 ± 0.1 mJ at a pulse repetition frequency (f) of 30 Hz. The diameter of the laser beam on the surface of the nail plate was 220 ± 15 μm. To control the shape and depth of the microholes, an optical microscopic registration of the appearance of laser-induced microdamages of the nail plate and the appearance of their longitudinal sections was carried out using an "Axio Scope A1" microscope (Carl Zeiss, Germany). A single through microhole with a diameter of ~300 μm was formed in the nail plate when exposed to 30 pulses of laser radiation. In Ref. [15] was obtained that at 300 μm hole's diameter the rate of 0.25% alcohol MB solution penetration is closed to maximal. The further increase in hole's diameter influenced the penetration rate not significant.

Experimental setup for the study of the process of active delivery of the aqueous methylene blue solution through a single microhole in the nail plate is presented in Fig. 2(a).

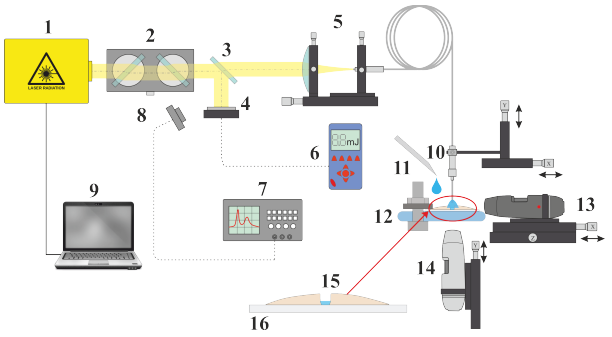
The time structure of Yb,Er:Glass laser pulse was obtained using the "FGA01" (Thorlabs, Inc., USA) InGaAs photodiode with 300 ps rise time connected to oscilloscope through a 50 Ω load. The pulses of Yb,Er:Glass laser radiation used for active delivery had a pronounced high-intensity "leading" spike (Fig. 2(b)), which makes it possible to amplify the excitation hydroacoustic effects [20]. The energy of Yb,Er:Glass laser pulse varied in the range from 10 to 100 mJ, the pulse duration was 1.5 ± 0.5 μs (base).

To visualize the penetration of the drug the paper with a density of 80 g/m and a thickness of 100 μm was placed under the sample. Coloration of the paper indicated the penetration of the drug through a microhole in the nail plate. The nail plate and paper were pressed against the glass substrate in such a way as to ensure tight contact between them. A 0.25% aqueous solution of methylene blue (250 mg of methylene blue powder per 100 g of distilled water) was used as a drug.

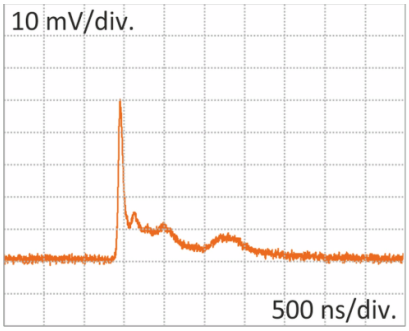


a b

Fig. 1 Scheme of the experimental setup for creating microholes in the nail plate (a): 1 – Er:YLF laser; 2 – plano-convex lens (F = 50 mm), 3 – nail plate on a glass substrate; 4 – germanium photodetector, 5 – oscilloscope; Er:YLF laser pulse (E = 4 mJ) (b).



a



b

Fig. 2 Scheme of the experimental setup for investigating the process of active delivery of a methylene blue solution through a perforated nail plate (a): 1 – Yb,Er:Glass laser (λ = 1.54 μm); 2 – Fresnel attenuator; 3 – beam splitter; 4 –"PE50BF-C" sensor (Ophir Optronics Ltd., Israel); 5 – unit for coupling laser radiation into the optical fiber; 6 – energy meter "Nova II" (Ophir Optronics Ltd., Israel); 7 – oscilloscope; 8 – InGaAs photodetector; 9 – computer; 10 – fiber output; 11 – drug injection needle (methylene blue solutions); 12 – glass substrate; 13 – "DTX 50" USB digital microscope (Levenhuk, Inc., USA); 14 – "Prima Expert" digital USB-microscope (LOMO OJSC, Russia); 15 – nail plate; 16 – paper; Yb,Er:Glass laser pulse (E = 100 mJ) (b).

This concentration is safe for the human body and effective against fungi and bacteria. Methylene blue is a widely used photosensitizer for photodynamic therapy of fungal diseases [1]. The choice of this drug is also because it has a rich blue color and is well visualized on the paper. A layer of the aqueous methylene blue solution was applied to the surface of the nail plate with a single microhole using a micropipette. The thickness of the drug (MB) layer h was controlled by an optical method, while photographs of the nail plate without and with the drug layer were analyzed.

Active delivery was carried out in two ways: 1) by diverging Yb,Er:Glass laser radiation from the output of quartz fiber (NA = 0.18, d = 470 μm, the distal end of the fiber was placed at different distances from the drug solution surface); 2) by focused radiation of Yb,Er:Glass laser (F = 11 mm, laser beam diameter d_b = 250 ± 20 μm, focus on the surface of the nail plate). The laser impact was implemented coaxially to the center of the microhole. The moment of paper coloration as a result of penetration of the drug under the nail plate was recorded using a digital USB microscope "Prima Expert" (LOMO OJSC, Russia). This moment corresponded to the "initialization" of the drug delivery. So, the fact of active drug delivery was detected by paper coloration. The experiment determined the number of laser pulses required for this "initialization".

The mass of the drug applied to the surface of the nail was determined by multiplying the drop volume by the density of the drug solution, which was taken equal to the density of water due to the low concentration of the dye. The mass penetrated under the nail plate with a single microhole was determined by weighing a piece of paper before and after the "initialization". For methylene blue, a dose of 5–10 mg/cm^2 can be considered as therapeutically sufficient [25]. In the experiment, the dose of the drug penetrated under the nail plate was determined as the ratio of the mass of the drug penetrated during "initialization" to the area of a single microhole in the nail plate.

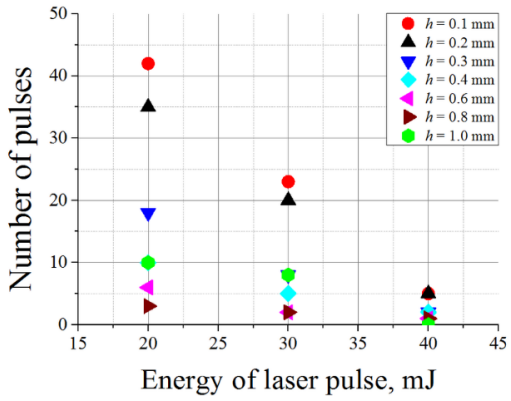
3 Research results

Using pulsed diverging Yb,Er:Glass laser radiation delivered via optical fiber whose distal end is located at a distance of H = 0.1 mm from the surface of drug drop applied to the nail plate it was possible to initiate the active drug delivery (detected by paper coloration) for h up to 1 mm at pulse energies $E \geq 20$ mJ (Fig. 3(a)).

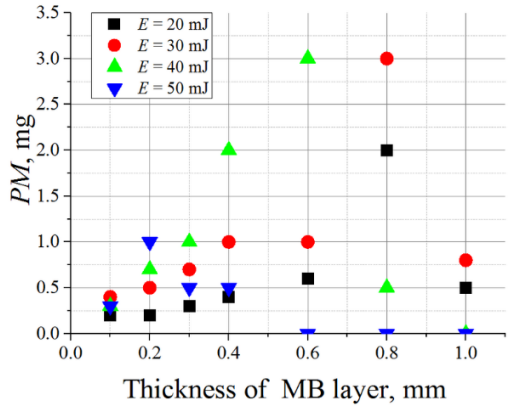
In the studied range of h (0.1 ÷ 1.0 mm), except for the range h = 0.9 ÷1 mm for E = 20 and 30 mJ, an increase in h resulted in a decrease in the number of pulses required for "initialization". The fastest "initialization" was obtained for h = 1.0 mm with E = 40 mJ, the number of pulses required for "initialization" in this case was N = 1.

The dependences of the mass of the drug (PM) penetrated through a single microhole in the nail plate at "initialization" on h at different energies of Yb,Er:Glass laser pulses and N = 50 are shown in Fig. 3(b). It can be seen that the dependences are not monotonic, but have a pronounced maximum, which depends on the pulse energy. For E = 20 mJ, the maximum PM = 2 mg was observed at h = 0.8 mm; for E = 30 mJ, the maximum PM = 3 mg was also observed at h = 0.8 mm; for E = 40 mJ, the maximum PM = 3 mg was observed at h = 0.6 mm and for E = 50 mJ – at h = 0.2 mm (maximum PM = 1 mg).

The influence of the distance H from the distal end of the optical fiber to the surface of drug drop on its "initialization" was also investigated. The diameter of laser spot d_s in a plane perpendicular to the beam axis and passing through the upper point of the drop, took values 0.83 ÷ 3.35 mm. It was established that when the optical fiber is at the distance H = 1 mm up from the drop surface (d_s = 0.83 mm), the "initialization" of drug delivery through a microhole occurs when applying three Yb,Er:Glass laser pulses with an energy of 60 mJ.



a



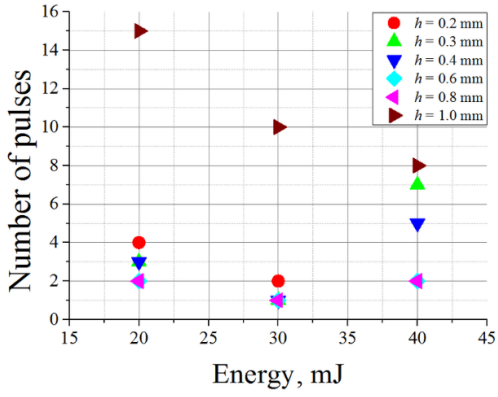
b

Fig. 3 Dependence of the number of pulses necessary for active laser drug delivery from the energy of laser pulse (a) and the mass of the drug penetrated (*PM*) under the nail plate from the thickness of MB layer *h* (b) when using diverging Yb,Er:Glass laser radiation ($H = 0.1$ mm, $N = 50$).

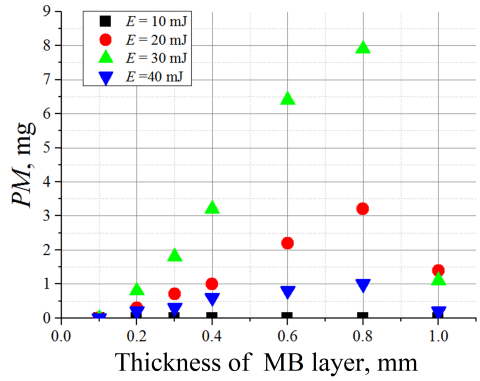
When $E = 80$ mJ and 100 mJ, "initialization" occurs after just one pulse. When the optical fiber was at the distance $H = 5$ mm up from the drop surface ($d_s = 2.27$ mm), "initialization" of drug delivery was observed only when applying 100 mJ Yb, Er:Glass laser pulse, but also after the one laser pulse. When the optical fiber was at $H = 8$ mm ($d_s = 3.35$ mm), there was no "initialization" of drug delivery under the nail plate.

Similar dependences were obtained during the "initialization" of drug delivery by focused radiation of a Yb,Er:Glass laser (Fig. 4). The number of pulses required for initialization in this case also first decreases with increasing *h* and then increases (Fig. 4(a)). The fastest initialization was obtained with $h = 0.2 \div 0.8$ mm and $E = 30$ mJ, the number of pulses required for "initialization" in this case was $N = 1$.

As for diverging radiation, dependencies of the mass (*PM*) of the drug penetrated through a single microhole in the nail plate at "initialization" on *h* at different energies of Yb,Er:Glass laser pulses and $N = 50$ (Fig. 4 (b) had maxima but, in this case, these maxima were observed at $h = 0.8$ mm for all pulse energies.



a

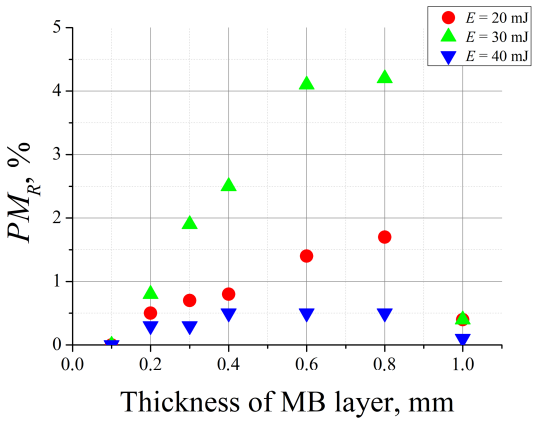


b

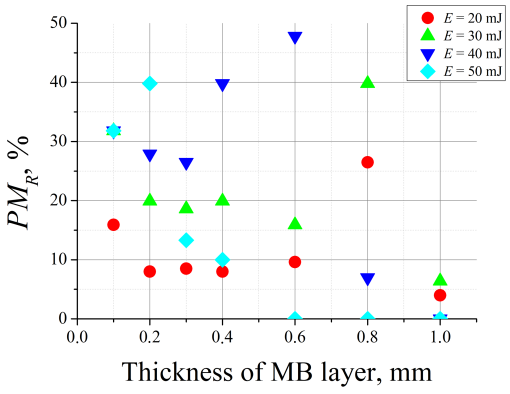
Fig. 4 Dependence of the number of pulses necessary for active laser drug delivery from the energy of laser pulse (a) and the mass of the drug penetrated (*PM*) under the nail plate from the thickness of MB layer *h* (b) when using focused Yb,Er:Glass laser radiation ($F = 11$ mm, $d_s = 250 \pm 20$ μm, focus on the nail plate surface, $N = 50$).

In Figs. 3(a) and 4(a), the decrease of pulse number *N* with the increase in laser pulse energy *E* occurs because with increasing *E* decreases the number of pulses required to achieve a pressure at the entrance to the microhole sufficient for MB to enter it. The pressure changes as a result of laser-induced heating of MB and the resulting hydrodynamic effects. The magnitude of this pressure is determined by the parameters of laser radiation, the properties of MB, properties of the nail and the size of the microhole. In Figs. 3(b) and 4(b), it is possible to note the presence of a maximum *PM*. In Fig. 3(b), the maximum *PM* shifts from $h = 0.8$ mm to $h = 0.2$ mm with increasing *E* from 20 mJ to 50 mJ. In Fig. 4(b), the position of the maximum does not depend on *E* and corresponds to $h = 0.8$ mm. The shift of *PM* maximum can be attributed to the MB spatter observed during this experiment, which is associated with the formation of a steam-gas bubble near the MB surface and its exit to the drug surface. The contribution of spatter to the reduction of *PM* for diverging Yb,Er:Glass laser radiation increases with increasing *E* and does not depend on *E* for focused laser radiation. The last one

can be associated with a significant excess of the power density of the focused laser radiation over the spatter effect threshold. One can also see that *PM* for focused laser radiation is significantly higher than *PM* for diverging laser radiation. This effect can also be related to the difference in power densities for both of these modes. The power density of focused laser radiation is greater than the power density of diverging laser radiation, since for focused radiation, $d_b = 250 \pm 20$ μm, and for the defocused at $H = 0.1$ mm, the spot diameter is about 500 μm. It should also be noted that the *PM* maximum at $h = 0.8$ mm correlates with the depth of water absorption of laser radiation with a wavelength of 1.54 μm.



a



b

Fig. 5 The percentage of *PM* relative to the mass of the applied drug (PM_R) at different thickness of MB, pulse energies E and $N = 50$ when using diverging Yb,Er:Glass laser radiation with $H = 0.1$ mm (a) or when using focused on the nail plate surface Yb,Er:Glass laser radiation with $F = 11$ mm and $d_s = 250 \pm 20$ μm (b).

Fig. 5 shows the percentage of *PM* relative to the mass of the applied drug – PM_R. Fig. 5(a) shows the relationship of the mass of the drug applied to the nail plate surface with the *PM* at different h, pulse energies of the diverging Yb,Er:Glass laser radiation, $H = 0.1$ mm and $N = 50$. Fig, 5(b) shows the relationship (PM_R) of the mass of the drug applied to the nail plate surface with the *PM* at different h and pulse energies of focused Yb,Er:Glass laser radiation and $N = 50$.

It can be seen that the maximum percentage of *PM* relative to the mass of the drug applied to the nail surface reaches 47.8% at $h = 0.6$ mm, $N = 50$ and $E = 40$ mJ, while the dose of the penetrated drug is 85.7 ± 10 mg/cm^2 and exceeds therapeutically sufficient dose. A further increase in h and energy E (at $h > 0.3$ mm) leads to a decrease in this ratio due to splashing of the drug.

It can be seen that in active delivery by focused Yb,Er:Glass laser radiation, the mass ratio of the applied drug to *PM* at best (at $E = 30$ mJ and $h = 0.8$ mm) reaches 4.2%, which is almost an order of magnitude less than in active delivery by diverging radiation. However, the maximum dose of the penetrated drug in active delivery with focused radiation was 225.7 ± 15 mg/cm^2, which is higher than with active delivery by diverging radiation and also exceeds the therapeutically sufficient dose. This effect is because when exposed to focused radiation, the drug solution is sprayed (splashing) and requires additional application after every two-laser pulses. Splashing of the drug during active delivery by focused Yb,Er:Glass laser radiation can be associated with both a change in the geometry of the laser impact and an increase in power density as a result of a decrease in laser spot diameter

4 Conclusion

The features of the active delivery of 0.25% methylene blue aqueous solution through the nail plate microperforated by Er:YLF laser radiation are investigated under various conditions of excitation of hydrodynamic effects in this solution by Yb,Er:Glass laser radiation. It is established that active delivery is most effective when using diverging Yb,Er:Glass laser radiation ($E = 40$ mJ, $h = 0.6$ mm, $H = 0.1$ mm). In this case, the drug is delivered under the nail plate when exposed to a single laser pulse, and within 50 laser pulses 3 mg of solution can be delivered. At the same time 47.8% of the drug mass applied to the nail surface penetrates the nail plate and the drug dose penetrated under the nail plate is 85.7 ± 10 mg/cm^2. The highest dose of the drug penetrated under the nail plate was fixed when exposed to focused radiation of Yb,Er:Glass laser ($E = 30$ mJ and $h = 0.8$ mm) and amounted to 225.7 ± 15 mg/cm^2.

Thus, in active laser delivery a quantity of the drug, well above the therapeutically sufficient dose, penetrates under the nail plate due to the excitation of hydrodynamic effects by the radiation of Yb,Er:Glass laser.

Disclosures

All authors declare that there is no conflict of interests in this paper.

References

1. L. W. F. Souza, S. V. T. Souza, and A. C. D. C. Botelho, "Distal and lateral toenail onychomycosis caused by Trichophyton rubrum: treatment with photodynamic therapy based on methylene blue dye," Anais brasileiros de dermatologia 89(1), 184–186 (2014).
2. S. Vahabi, R. Fekrazad, S. Ayremlou, and N. Zangeneh, "The effect of antimicrobial photodynamic therapy with radachlorin and toluidine blue on streptococcus mutans: an in vitro study," Journal of dentistry (Tehran, Iran) 8(2), 48–54 (2011).
3. M. G. Strakhovskaya, V. G. Zhukhovitskii, A. F. Mironov, A. M. Seregin, E. F. Stranadko, and A. B. Rubin, "Fungicidal activity of khlorin photosensitizers," Doklady Biochemistry and Biophysics 384(1–6), 155–158, (2002).
4. R. Elkeeb, A. AliKhan, L. Elkeeb, X. Hui, and H. I. Maibach, "Transungual drug delivery: current status," International journal of pharmaceutics 384(1), 1–8 (2010).
5. M. V. Saner, A. D. Kulkarni, and C. V. Pardeshi, "Insights into drug delivery across the nail plate barrier," Journal of drug targeting 22(9), 769–789 (2014).
6. R. M. Adams, "Effects of mechanical trauma on nails," American journal of industrial medicine 8(4–5), 273–280 (1985).
7. S. Murdan, "Enhancing the nail permeability of topically applied drugs," Expert opinion on drug delivery 5(11), 1267–1282 (2008).
8. S. N. Murthy, D. E. Wiskirchen, and C. P. Bowers, "Iontophoretic drug delivery across human nail," Journal of pharmaceutical sciences 96(2), 305–311 (2007).
9. A. Torkar, J. Kristl, and S. Murdan, "Low-frequency ultrasound to enhance topical drug delivery to the nail," Presented at AAPS Annual Meeting and Exposition, San Diego, CA, USA (2007).
10. J. Neev, J. S. Nelson, M. Critelli, J. L. McCullough, E. Cheung, W. A. Carrasco, A. M. Rubenchik, L. B. Da Silva, M. D. Perry, and B. C. Stuart, "Ablation of Human Nail by Pulsed Lasers," Lasers in Surgery and Medicine 21(2), 186–192 (1997).
11. M.-T. Tsai, T.-Y. Tsai, S.-C. Shen, C. Ng, Y.-J. Lee, J.-D. Lee, and C.-H. Yang, "Evaluation of Laser-Assisted Trans-Nail Drug Delivery with Optical Coherence Tomography," Sensors (Basel) 16(12), 2111 (2016).
12. O. O. de Morais, I. M. C. Costa, C. M. Gomes, D. H. Shinzato, G. M. C. Ayres, and R. M. Cardoso, "The use of the Er:YAG 2940nm laser associated with amorolfine lacquer in the treatment of onychomycosis," An Bras Dermatol 88(5), 847–849 (2013).
13. E. B. Abd El-Aal, H. M. Abdo, S. M. Ibrahim, and M. T. Eldestawy, "Fractional carbon dioxide laser assisted delivery of topical tazarotene versus topical tioconazole in the treatment of onychomycosis," Journal of Dermatological Treatment 30(3), 1–6 (2019).
14. A. V. Belikov, A. N. Sergeev, S. N. Smirnov, and A. D. Tavalinskaya, "Microperforation of the human nail plate by radiation of erbium lasers," Frontiers of Optoelectronics 10(3) 299–307 (2017).
15. S. Smirnov, A. V. Belikov, A. V. Skrypnik, A. N. Sergeev, and A. D. Tavalinskaya, "Er: YLF-laser microperforation of the nail plate for drug delivery," Proceedings of SPIE 10716, 107160X (2018).
16. P. Gregorčič, M. Jezeršek, and J. Možina, "Optodynamic energy-conversion efficiency during an Er:YAG-laser-pulse delivery into a liquid through different fiber-tip geometries," Journal of Biomedical Optics 17(7), 075006 (2012).
17. M. Frenz, H. Pratisto, F. Konz, E. D. Jansen, A. J. Welch, and H. P. Weber, "Comparison of the effects of absorption coefficient and pulse duration of 2.12-um and 2.79-um radiation on laser ablation of tissue," IEEE Journal of Quantum Electronics 32(12), 2025–2036 (1996).
18. E. D. Jansen, T. Asshauer, M. Frenz, M. Motamedi, G. Delacrétaz, and A. J. Welch, "Effect of pulse duration on bubble formation and laser-induced pressure waves during holmium laser ablation," Lasers in Surgery and Medicine 18(3), 278–293 (1996).
19. A. V. Belikov, S. V. Gagarsky, A. N. Sergeev, and S. N. Smirnov, "Study of hydrodynamic processes in liquids under the influence of powerful microsecond Yb,Er:Glass laser pulses," Journal of Instrument Engineering 60(4), 367–374 (2017) [in Russian].
20. A. V. Belikov, S. V. Gagarsky, A. N. Sergeev, S. N. Smirnov, and A. M. Zagorulko, "Study of acoustic signal during laser hydroacoustic processing of biological tissue by microsecond pulses of ytterbium-erbium glass laser radiation," Scientific and Technical Journal of Information Technologies, Mechanics and Optics 18(6), 939–945 (2018) [in Russian].
21. S. N. Smirnov, S. V. Gagarskiy, Y. Y. Fomicheva, A. V. Belikov, A. N. Sergeev, and A. M. Zagorulko, "Investigation of optical and hydrodynamic processes initiated in biological tissues and liquids under the action of high-power pulses of 1.54 μm laser radiation," Proceedings of SPIE 10716, 107160W (2018).

22. A. V. Belikov, A. M. Zagorulko, and S. N. Smirnov, "Optimum mode for processing cataract lens of the human eye with microsecond pulses of Yb,Er:Glass laser," Journal of Instrument Engineering 61(8), 734–737 (2018) [in Russian].
23. A. V. Belikov, S. N. Smirnov, A. N. Sergeev, and A. D. Tavalinskaya, "Delivery of the photodynamic agent under the nail plate using Er-laser microperforation and laser-induced hydrodynamic processes," 2018 International Conference Laser Optics (ICLO), 491 (2018).
24. A. V. Belikov, A. V. Skrypnik, K. V. Shatilova, and V. V. Tuchin, "Multi-beam laser-induced hydrodynamic shock waves used for delivery of microparticles and liquids in skin," Lasers in surgery and medicine 47(9), 723–736 (2015).
25. C. Peter, D. Hongwan, A. Küpfer, and B. H. Lauterburg, "Pharmacokinetics and organ distribution of intravenous and oral methylene blue," European journal of clinical pharmacology 56(3), 247–250 (2000).